OPTO ACOUSTIC OSCILLATOR USING SILICON RF MEMS BASED OPTICAL MODULATOR

A Dissertation

Presented to the Faculty of the Graduate School

of Cornell University

in Partial Fulfillment of the Requirements for the Degree of

Doctor of Philosophy

by

Suresh Sridaran

May 2012

OPTO ACOUSTIC OSCILLATOR USING SILICON RF MEMS BASED OPTICAL MODULATOR

Suresh Sridaran, Ph.D.

Cornell University 2012

Mechanical resonators have been used for the last few decades as the frequency selection element of high frequency oscillators and radio frequency filters due to their high quality factors. Mechanical resonators scaled to the micro scale, called micromechanical resonators, offer the promise of integration of these high precision frequency selection elements along with microelectronics on the same substrate. Scaling to the micro scale allows micromechanical resonators operate at desired higher frequencies compared to their macroscopic counterparts. This along with the advantage of lower manufacturing cost due to the microelectronic fabrication process used for the their fabrication have made them attractive candidates for use in modern wireless radio devices. Micromechanical resonators excited and sensed using electrostatic air gap capacitive transduction have been shown to have very high quality factors close to the material loss limit. While electrostatic air gap transducers are easy to co-fabricate with microelectronics in a shared process, it suffers from lower sensitivity at higher frequencies making it difficult to use in high frequency applications. Cavity optomechanical systems, where a mechanical resonator is also an optical resonance cavity, has been shown to be one of the most sensitive methods for detecting mechanical motion. Such systems use shifts in the optical resonance frequency of the optomechanical resonator to sense mechanical motion. Presently, these optomechanical systems are used for measuring mechanical thermal noise

displacement or mechanical motion actuated by optical forces. In this dissertation, a monolithic scheme for integration of electrostatic capacitive actuation of mechanical resonators with optical sensing using silicon optomechanical disk resonators and waveguides is presented.

To obtain an optically sensed electrostatically actuated mechanical resonator, a coupled disk geometry is used, where one disk acts as the sensing optomechanical resonator while mechanical vibrations are excited through electrodes around the other disk. The electrostatically actuated optomechanical resonator combines the frequency filtering response of a mechanical resonator with the optical amplitude modulation property of the optomechanical resonator thereby creating an integrated narrowband optical modulator.This narrow band optical modulator called the acousto optic modulator and fabricated on the silicon device layer of a silicon on insulator substrate modulates output light when the electrical input is around the mechanical resonance. For disks of 10μm radius, the radial vibrational modes are observed as optical modulation around 236MHz with an extinction ratio of 12dB for a DC bias of 20V, RF input power of 5dBm and optical quality factor of 53,000. Scaling the radius of the disks to 3.8/*mu*m increases the observed frequency of the fundamental mode resonance to 706MHz along with the second radial vibrational mode to 1.93GHz. An alternate geometry using ring resonators shows multiple mechanical modes up to 3.5GHz making this one of the highest observed mechanical frequencies with air gap electrostatic actuation.

An important application of mechanical resonator is in frequency selection as part of an oscillator loop. Implementing the acousto optic modulator in an oscillator is similar to the opto-electronic oscillator (OEO), which is the current state-of-art oscillator in the few GHz regimes that uses optical feedback in the

oscillation loop. The optical output from the modulator is converted back to the electrical domain using a high speed optical detector and then amplified and fed back into the modulator. Employing this technique, an opto-acoustic oscillator (OAO) has been demonstrated at the mechanical frequency of 236MHz of the disk resonator with an output power of 6.5dBm and a phase noise of -65dBc/Hz at 1kHz offset. Additionally, an OAO operating at 1.12 GHz with an output power of 8.8dBm and -65dBc/Hz at 10kHz offset is demonstrated using the ring resonator based modulator. In summary, this work presents a combined electrical-optical micromechanical system fabricated on a CMOS compatible process thereby opening up the possibility of novel devices for future electo-optic-mechanical multi domain systems.

BIOGRAPHICAL SKETCH

Suresh Sridaran was born in Secunderabad, India to Sridaran Ragothama Rao and Subbulakshmi Sridaran on 8th January 1985. He was schooled in erstwhile Madras and graduated from Padma Seshadri Bala Bhavan high school in 2002. He went on to obtain a Bachelors in Technology in Engineering Physics from the Indian Institute of Technology, Delhi in 2006 before moving to Cornell University to pursue doctoral studies in Electrical Engineering where he joined the OXIDEMems lab to work on studying optomechanical interactions under the guidance of Professor Sunil Bhave. In addition to his research interests, he is an avid railfan and has developed Indian railway based train simulator software.

To my parents

ACKNOWLEDGEMENTS

Firstly, I would like to express my deepest gratitude to my advisor Prof. Sunil Bhave, without whose support this work would never have been possible. His constant encouragement and confidence in my eventual success is what kept me going in the face of failures. His endless stream of ideas and extreme enthusiasm ensured that there was never a dull moment. His informal approach to advising and his concern for students made working in his group extremely enjoyable. I am very grateful to have had the opportunity to work with him and thank him for his very thoughtful guidance.

I would like to thank my committee members, Prof. Farhan Rana and Prof. Michal Lipson for their guidance and support. They have been very helpful in putting things in perspective and for making sure that I ask the right questions and target the right problems. They have always been available to answer my queries and provide inputs to guide me in the right direction. I am very lucky to get to interact with them and learn from their expertise and I am highly indebted to them for the same. I would also like to express my deepest gratitude to all my teachers from school, from IIT Delhi and at Cornell University for sharing their immense knowledge with me. Their teaching of staying thirsty for figuring out the unknown was what motivated me to pursue my doctoral work.

I would also like express my most sincere thanks to all the past and present members of the OxideMEMS group who made the lab feel like home - Dana Weinstein, Hengky Chandrahalim, Eugene Hwang, Chen Chen, Tiffany Cheng, Susmita Bhandari, Laura Fegely, David Hutchison, Siddharth Tallur, Tanay Gosavi, Ryan Wang and Ben Tang. Thanks specially to Dana and Hengky for their help in getting me used to the fabrication process and David for his immense help in the setup of the optical characterization equipment.

I would like to express my deepest thanks to the many graduate students in the ECE program, the interactions with whom greatly helped in shaping my ideas. I would like to thank my colleagues in SONIC MEMS lab and Cornell Nanophotonics Group who most readily shared their CNF wisdom. I would also like to thank my colleagues in the Semiconductor Optoelectronics group, Apsel lab and the Cornell UNIC Lab. In particular, I would like to thank Sasikanth Manipatruni and Gustavo Wiederhacker for very useful discussions about optics and optomechanics. The assistance of the staff of the Cornell Nanophotonics Facitity was instrumental in the fabrication of the devices presented in this work. I am highly indebted to them for the same. The Duffield hall grad office space was the best environment to think, work and have fun - a very special thank you to all my colleagues in Duffield hall who made this possible. Thanks in particular to the ECE desi group - Mustansir Mukadam, Krishna Jayant, Shantanu Rajwade, Siddharth Tallur and Tanay Gosavi for keeping me up to date with world affairs over lunch and coffee in the Duffield Atrium and thanks to Mattin's cafe for providing the required caffeine.

I was lucky to be in the company of amazing friends whom I could fall back upon for any help. I would like to express my most sincere gratitude towards all of them who made me feel at home away from home. Thanks to Vivek Venkataraman, Rajendran Naryanan, Sasikanth Manipatruni, Anand Vaidya, Amit Singhai, Siddharth Tallur, Stueti Gupta, Pavithra Sundararajan and Krishna Etika for the splendid dinners and the amazing insights into life, the universe and everything. Thanks to my close friends Rahul Yadav, Girish Upadhyay, Pankaj Balani, Gagandeep Mallarpu, Karthik Venkataraman, Sangameshwar Rao, Shrinivas Mohan, Vaideesh Subbaraj and Rajiv Soundararajan for all their encouragement during my school and college days. I also thank the many

many more friends along the way who have made this journey highly enjoyable.

Lastly,but not least I am extremely indebted to my family for their unconditional love and support. Many thanks to my sisters Sudha and Sujatha and brother-in-law Santosh who have been there at every step to provide invaluable guidance and motivation. Thanks also to the newest member of the family, Sanjana for the all the joy she has brought us. A huge thank you will not suffice for my parents, who have so unselfishly always put my interests before theirs. Thanks Dad, for your zest for life which I am still trying to imbibe and the constant push for doing things better. I am only just realizing that the advice was not meant to annoy me but to try to make me a better person. Thanks Mom, for showering me with so much love and affection that I cant describe with words.I am still striving to achieve the perfect recipe you have taught me, 'to give it my best and leave the rest'.

In the end, thanks to nature, universe and everything around me for conspiring for me to do this work. Nothing would have been possible without it.

TABLE OF CONTENTS

LIST OF TABLES

LIST OF FIGURES

CHAPTER 1

INTRODUCTION

1.1 Micromechanical Resonators

The field of Micro-Electro-Mechanical Systems (MEMS) consists of mechanical structures that are on the order of a few microns and are made using micro-fabrication techniques. These systems enable integration of sensors and actuators along with the processing electronics that provide the electrical signals required for actuating and sensing. This scheme allows the electronics to interact with the world and at the same time offers a lower cost due to the parallelism of micro-fabrication. Some examples of such systems are motion sensors such as accelerometers and gyroscopes and the moving mirrors in a digital micromirror device. A particular device of interest in this field is the micromechanical resonator. Resonators are devices that naturally oscillate at some frequencies called resonant frequencies with greater amplitude than at other frequencies. At these resonant frequencies there is constructive interference which leads to energy storage within the resonator and very little energy leakage from within the system. Resonators are found in multiple domains including mechanical and electromagnetic domains.In everyday life, examples of mechanical resonators are musical instruments like the guitar and the drum. These instruments make use of the mechanical resonance phenomena to produce sound waves at particular frequencies.

A resonator responds strongly to an input forcing function at the resonant frequency as it stores energy at these frequencies. When the input is not at the resonant frequency the response of the resonator is much smaller. This response

makes them ideal candidates for use as frequency selection elements. In electronics, almost all high precision frequency synthesis makes use of the mechanical resonance of quartz crystals. As electronic wireless communication moves to higher radio frequencies, there is a need to obtain mechanical resonators with higher resonance frequencies. As the resonance frequency is inversely proportional to the mass, this involves making the mechanical resonators smaller and eventually into the micro scale. Micromechanical resonators offer the promise of integration of high precision frequency selection elements, operating at the required higher frequencies fabricated at very low cost along with microelectronics using a similar fabrication process. In addition to the frequency selection applications, micromechanical resonators have also been demonstrated for use in sensors such as gyroscope [6] and mass sensors [7].

1.1.1 Micromechanical Resonator Transduction

To obtain a mechanical response from a micromechanical resonator it is necessary to be able to apply mechanical force on the resonator and detect the motion of the resonator. The easiest interface to apply a force is using electrical signals. Electrical signals can be easily routed in the macroscopic and microscopic domain and can be processed by microelectronics in order to provide a complete system of transduction and signal processing. Some of the common techniques for excitation of mechanical motion are briefly described below.

Electrostatic Actuation

Electrostatic forces is the force obtained when a charged particle is placed in a electric field. This electric field can be obtained due to another charged particle or due to a set of charged particles. As the electric field of a charged particle decreases as the square of the distance away from the particle, the force can be significant when the distance between the charges are small as is the case at the micro scale. Electrostatic forces are most commonly obtained across the plates of a charged capacitor and this force is inversely proportional to the square of the capacitive gap. Electrostatic force is one of the most popular schemes of actuation of micromechanical structures and was used in one of the earliest demonstration of micromechanical actuation[8]. The advantages of using electrostatic actuation include zero power consumption at DC as the electric potential is applied across a capacitor. On the other hand, electrostatic actuation requires high voltages to obtain large forces and suffers from pull-in instability which limits the amount of travel obtainable.

Piezoelectric Actuation

The piezoelectric effect is observed in certain materials, where application of a electrical potential across the material can lead to a mechanical stress in the material. The piezoelectric force occurs due to asymmetric charge distribution in the crystal leading to a electric dipole. This force is present through the body of the piezoelectric material across which the potential is applied. This property makes this force very efficient in exciting motion in the bulk of the material [9]. However, the need for specialized materials and fabrication for these materials make integration with microelectronics harder.

Thermal Actuation

The process of joule heating using electric current is used to obtain a temperature changes in the structure to be actuated. A lever or a bimorph geometry is used to convert the expansion of the heated structure with respect to the static structure in order to obtain a large displacement. The disadvantage of thermal actuation is the large power dissipation for actuation using joule heating.

Magnetic Actuation

This actuation technique uses the force experienced by a current carrying coil in the presence of a magnetic field. A current is sent through the structure to be actuated while a magnetic field is either applied externally through an electromagnet[10]. This scheme of actuation is very simple to implement on chip as it does not require complicated actuators around the mechanical structure. However, the need for a powerful magnetic field applied externally makes integration into a system harder and has a higher power consumption due to the system drawing a large current. Of all the schemes described above, the one considered for actuation for the rest of this work is electrostatic actuation. There are multiple ways to detect the motion of mechanical resonators, a couple of which are introduced below.

Electrostatic Sensing

In this scheme, the mechanical motion is coupled to the motion of one of the plates of a sense capacitor. This capacitance change is then detected at the output to obtain a motional signal. When static displacement needs to be sensed,

an impedance divider with a reference capacitance is used to obtain the displacement. For the case of motion at the mechanical resonance frequency, the movement of the plate modulates the capacitance at the mechanical resonant frequency. This time varying capacitance can be picked up at the output as an alternating current on application of a DC potential.

Piezoresistive Sensing

In the case of piezoresistive sensing, the mechanical motion is coupled to a change in the dimension and resistivity of a resistive element. This resistive change can be picked up at the output by observing the change in the current for an applied DC potential across the resistive element. There is some DC power consumption with this technique as a current is constantly flowing through the resistor to interrogate the motion.

Optical Sensing

Optical interferometric sensing offers one of the most sensitive schemes for sensing displacements. Previous demonstrations of the optical sensing of micro structures used the micro structures as movable micromirrors of a macroscopic optical cavity [2, 1, 3]. Free space optics are used to form a Fabry-Perot optical resonance cavity with the microstructure. Using this setup, a displacement sensitivity good enough to observe the thermal brownian motion is observed as shown in figure 1.1. These demonstrations were also the first demonstrations of optical force due to radiation pressure damping the thermal brownian noise in micromechanical resonators. While these demonstrations exhibit the sensitivity

of the optical sensing scheme, they require the use of bulky free space optics systems and are not implementable in a micro scale package.

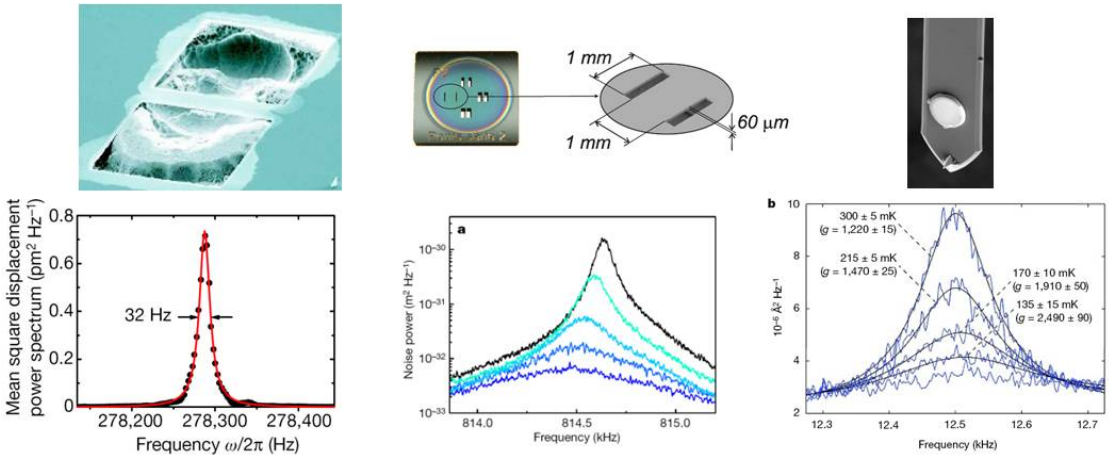

Figure 1.1: (left)Image from [1] (middle) Image from [2] (right) Image from [3]. The images show the vibrating micro structure along with the thermal Brownian noise spectrum measured by optical sensing

1.2 Cavity Optomechanics

In the past few years, the fields of optical microresonators and mechanical resonators have seen a lot of research activity independently for a variety of applications. While electromagnetic radiation pressure force was well understood earlier, the dynamic effect of light exciting a mechanical resonator mode first demonstrated in ultra high quality factor silica micro toroids [11, 12] brought the two fields together to establish the field of cavity optomechanics. The ultra high optical quality factor micro toroid resonators allowed the optical power within the disk to reach very high levels.A large radiation pressure force obtained due

to the high optical power on the walls of the microtoroid and the small mass and stiffness of the microtoroid lead to mechanical displacement of the microtoroid. Self oscillations at the mechanical resonance frequency were setup due to the feedback provided by the mechanical displacement on the optical mode and vice versa. This demonstration led to a slew of research on optomechanical resonators coupling high optical quality factor resonances to small mechanical displacements of the cavity [13, 14, 15]. The optical radiation pressure excited mechanical displacements are also sensed using optically using the same optomechanical resonator. Most of these demonstrations of self oscillations were carried out in resonators fabricated on silicon dioxide or silicon nitride with the optomechanical resonators being interrogated by suspended tapered optical fiber [15]. While this approach had combined the resonator devices at the microscale, it still posed the challenge of integration into a micro scale package due to the need for fine macroscopic adjustment of the spacing between the optomechanical resonators and the tapered fiber.

1.2.1 Silicon Optomechanics

Scaling in the field of microelectronics has pushed the size of silicon transistors to smaller dimension in order to operate faster and at higher frequencies. In addition to scaling, the number of processing cores has been increasing in the past few years. With the advent of multiple processing cores, one of the main roadblocks that has remained is the need for high bandwidth low power interconnects for intrachip communication. Silicon photonics was proposed as the solution to this problem by using optical waveguides and modulators similar to those used macroscopic fiber optic communication . A large body of work

dedicated towards this problem has demonstrated low loss optical waveguiding in silicon [16], micro-optical resonators [17], optical modulators [18] and a multitude of other devices [19] . These demonstrations were carried out in the silicon device layer of silicon-on-insulator (SOI) wafers which offers a platform for integration with silicon CMOS processes. In addition to the conventional photonic devices, optomechanical devices have also been demonstrated in the SOI platform. Mechanically suspended silicon waveguides were used for the first microscale demonstration of optical forces due to an optical field gradient [20].In addition, the SOI platform has also shown to be conducive for the fabrication of mechanical resonators [21, 22]. This makes the silicon-on-insulator an ideal platform for combining electrically actuated mechanical resonators with optomechanical resonators.

In the following chapter, an analytical expression for the mechanical resonances of a disk resonator along with the conventional scheme of actuation and sensing is presented. The drawbacks associated with the conventional scheme of sensing high frequency mechanical resonators is discussed. Chapter 3 moves to the optical domain starting with the fundamentals of an optical resonator and its application in displacement sensing. An initial attempt at combining silicon photonics using thin buried oxide SOI wafers is studied at the end of the chapter. Chapter 4 follows up by presenting a process for combining electrostatically actuated silicon mechanical resonator with a silicon optomechanical resonator on thick buried oxide SOI wafers. The device obtained by combining the two domains is a narrowband optical modulator. Characterization techniques and experimentally measured performance data for the modulator is examined before the device is scaled to higher frequencies. Chapter 5 investigates the application of the device in an oscillator and the results obtained thereof.

CHAPTER 2

MICROMECHANICAL DISK RESONATORS

2.1 Lumped Model for Disk Resonator

The analytic expression for radial displacement and the resonant frequencies are obtained by solving the elastic wave function with appropriate boundary conditions as outlined in [23, 24]. The solution for the radial displacement for the first order radial mode which does not have an azimuthal dependence is given by

$$u_r(r) = A\frac{h}{R}J_1\left(h\frac{r}{R}\right) \tag{2.1}$$

where $u_r(r)$ is the radial displacement at a radial location r, R is the radius of the disk and h is the normalized frequency parameter given by $h = \omega_o R\sqrt{\frac{(1-\nu^2)\rho}{E}}$, where ω_o is the angular resonance frequency of vibration and E, ρ and ν are the Young's modulus, density and Poisson's ratio of silicon respectively.To obtain the mechanical displacement frequency, we use the boundary conditions of radial normal stress and circumferenital shear stress being 0 at the free end [23]. The expression for the resonance frequency is then

$$\frac{hJ_0(h)}{J_1(h)} = 1 - \nu \tag{2.2}$$

To simplify analysis, the distributed disk resonator can be represented by an equivalent mass-spring- damper system assumed to be lumped together at the location of interest. The lumped mass is then assumed to vibrate with the displacement amplitude of the location on the actual resonator for which the equivalent model is evaluated. In the case of the first order radial mode we consider the equivalent mass at the edge of the disk. The effective mass is then

obtained by dividing the total kinetic energy of the disk resonator by the square of velocity at R [5]. When the resonator is vibrating at the resonant frequency, the velocity at a location r is a derivative of the displacement and the velocity amplitude can be expressed as $v(r) = \omega_o u(r)$. The effective mass(m_{eff}) is then

$$\begin{aligned} m_{eff} &= \frac{KE_{tot}}{\frac{1}{2}v(R)^2} = \frac{2\pi\rho t \int_0^R r v(r)^2 \, dr}{v(R)^2} \\ &= \frac{2\pi\rho t}{J_1(hR)^2} \int_0^R r J_1(hr)^2 \, dr \end{aligned} \tag{2.3}$$

The effective spring constant is given by $k_{eff} = \omega_o^2 m_{eff}$ and the effective damping factor by $b_{eff} = \omega_o m_{eff}/Q$. The equation of motion for the radial displacement of the disk edge u_R is then

$$m_{eff}\frac{d^2u_R}{dt^2} + b_{eff}\frac{du_R}{dt} + k_{eff}u_R = F_{es} \tag{2.4}$$

At resonance, the inertial term cancels the restoring force term. The velocity at resonance is then determined by the damping in the system and is represented as

$$\left.\frac{du_R}{dt}\right|_{\omega=\omega_o} = \frac{F_{es}}{b_{eff}} \tag{2.5}$$

The damping coefficient b_{eff} is a measure of the energy dissipated from the system at resonance and can be represented in terms of the qulaity factor. The mechanical quality factor is a ratio of the energy stored to the energy dissipated per cycle. The quality factor can also be obtained by frequency response measurements using $Q = f/\Delta f$

$$b_{eff} = \frac{m\omega_o}{Q} \tag{2.6}$$

2.2 Electrostatic capacitive transduction

2.2.1 Actuation

Electrostatic capacitive actuation is a popular technique for actuating motion of micromechanical devices. The scheme used for electrostatic actuation consists of a closely spaced electrode surrounding the resonator forming an air gap resonator as shown in fig.2.1. When the resonator is electrically grounded and a potential (V) applied to the capacitor plates, a force is obtained on the plates of the capacitor. This is due to an accumulation of opposite charges on the capacitor fields leading to an attractive force (F) between the plates given by

$$F = \left|\frac{\partial U}{\partial d}\right| = \frac{1}{2}\left|\frac{\partial C}{\partial d}\right| V^2 = \frac{1}{2}\frac{\epsilon_o A}{d^2}V^2 \tag{2.7}$$

where U is the potential energy of the capacitor, A is the area of the capacitor and d is the electrode resonator spacing. To obtain a force at a frequency ω, a combination of AC and DC potentials are applied. This combination gives rise to a force at ω due to the nonlinear dependence of force on potential applied.

$$\begin{aligned} F &= \frac{1}{2}\frac{\epsilon_o A}{d^2}(V_{dc} + v_{ac}sin(\omega t))^2 \\ F_\omega &= \frac{\epsilon_o A}{d^2}V_{dc}v_{ac} \\ F_\omega &= V_{dc}\frac{\partial C}{\partial d}v_{ac} = \eta v_{ac} \end{aligned} \tag{2.8}$$

where we have introduced the electromechanical coupling coefficient $\eta = V_{dc}\partial C/\partial d$. To increase this force, we need to reduce the electrode-resonator spacing, increase the area of the capacitor and the potential applied to the capacitor plates. At higher frequencies, the impedance of the capacitor reduces leading to

a smaller potential drop across the plates. This leads to a smaller force at higher frequencies. To obtain the response of the resonator when this force is at the mechanical resonant frequency, using (2.5),(2.8) we obtain the velocity amplitude to be

$$\frac{du_R}{dt} = \frac{\eta v_{ac}}{b_{eff}} \tag{2.9}$$

Representing the velocity amplitude as $\omega_o u_R$, the displacement amplitude u_R is obtained to be $u_R = QF_\omega/k_{eff}$ where Q is the quality factor and k_{eff} is the effective stiffness of the mechanical resonator. This expression shows that the displacement amplitude at resonance is enhanced by the quality factor compared to the displacement amplitude to a static force.

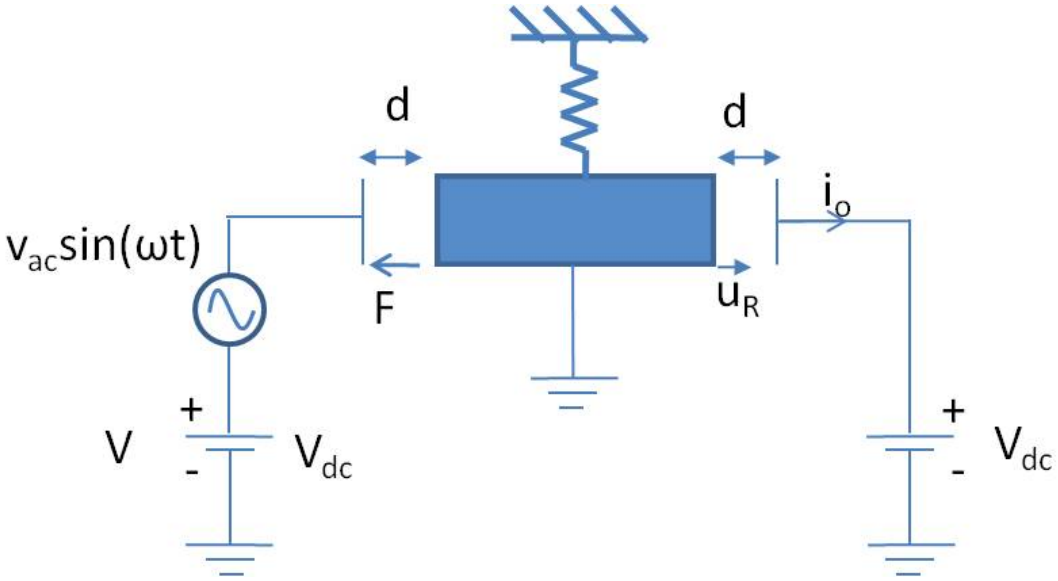

Figure 2.1: Schematic of electrostatic capacitive actuation (left electrode) and capacitive sensing (right electrode)

2.2.2 Capacitive displacement sensing

A scheme similar to actuation is used for sensing. The basis for sensing is a time varying capacitance that can be read out as a displacement current. This can be done by either looking at the current on the actuation capacitor or by using a separate electrode for sensing as shown in fig. 2.1. On application of a DC potential to the right capacitor electrode of fig. 2.1, a current i_o at the output is obtained. This current is related to the amplitude of displacement by

$$\begin{aligned} i_o &= \frac{d(CV)}{dt} = V_{dc}\frac{dC}{dt} = V_{dc}\frac{dC}{du_R}\frac{du_R}{dt} \\ i_o &\approx V_{dc}\frac{\partial C}{\partial d}\frac{du_R}{dt} = \eta\frac{du_R}{dt} \end{aligned} \tag{2.10}$$

Using (2.10) and (2.9), a relation between the current at the output to the voltage at the input at resonance frequency is obtained as

$$i_o = \frac{\eta^2 v_{ac}}{b_{eff}} \tag{2.11}$$

2.3 Electrical Equivalent

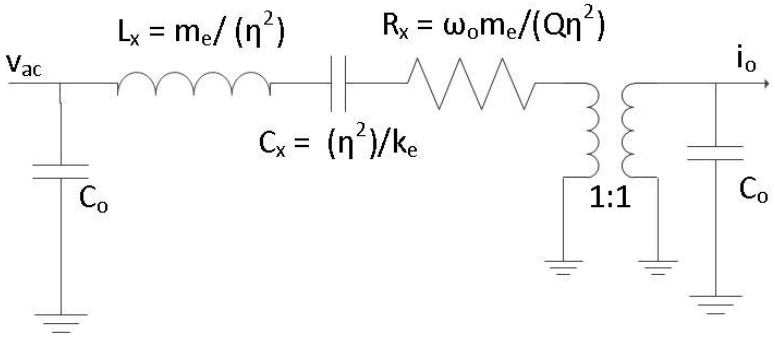

Figure 2.2: Electrical equivalent of the electrostatically transduced mechanical resonator

The differential equation for the mechanical model developed in the earlier section is very similar to the governing equations of a LCR resonator. To study the electrical transmission property of the mechanical resonator, it is convenient to define a electrical equivalent circuit that has the same response as the resonator [5, 25, 26]. Figure 2.2 shows the mechanical equivalent of the mechanical resonator. The equivalent inductor is proportional to the mass of the resonator while the capacitor is inversely proportional to equivalent stiffness of the resonator. At resonance, the current at the output is determined only by the resistor and this is obtained from (2.11). The actuation and the sense capacitors appear in parallel to the motional arm and offer a competing lower impedance path to ground at high frequencies. In order to obtain the maximum response to an input voltage at resonance, it is necessary to reduce the motional impedance. Using (2.11), the motional resistance is

$$R_x = \frac{\omega_o m_{eff}}{Q} \frac{d^4}{\epsilon_o^2 A^2 V_{dc}^2} \tag{2.12}$$

To reduce the motional impedance, the electrode to resonator spacing d is designed as small as possible while increasing the area of the actuation capacitor and the quality factor. At higher frequencies, the motional impedance gets larger due to the direct dependence on frequency. In addition, as the resonators are smaller at higher frequencies ,the area of actuation is smaller which in turn adds to the increase in motional impedance.

2.4 Previous Demonstrations

Figure 2.3 shows images and results of previous demonstrations of electrostatically actuated micromechanical disk resonators. The disk resonator in these

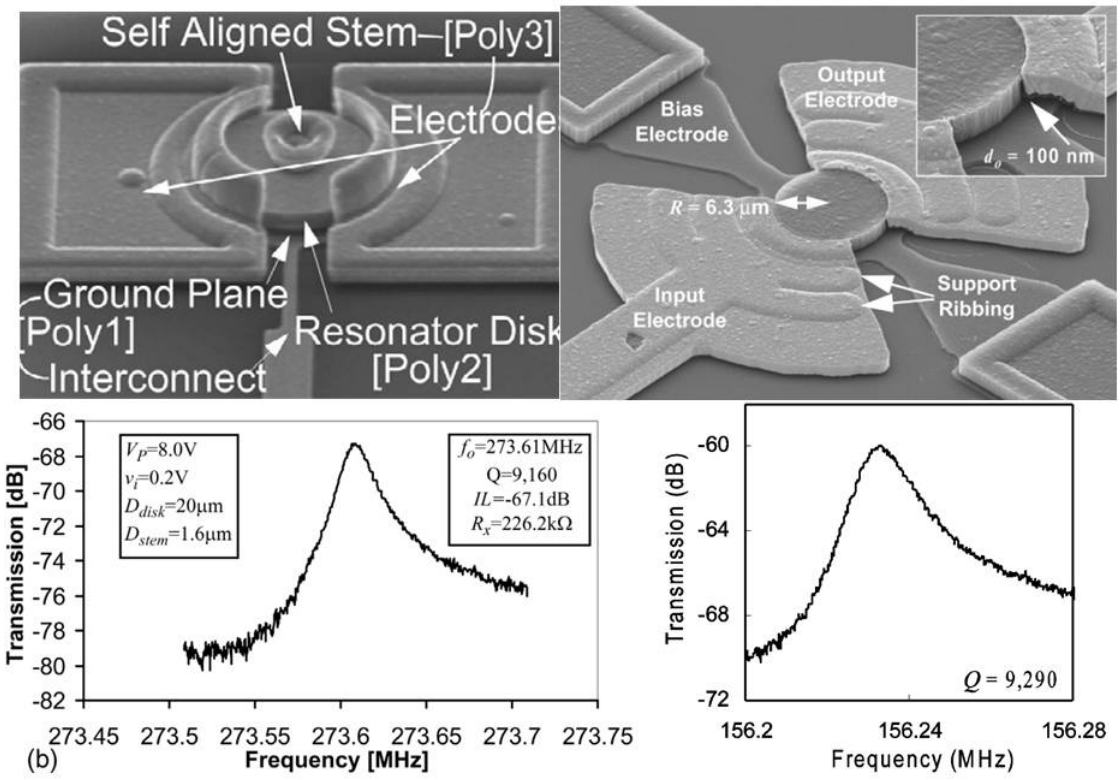

Figure 2.3: (left top) Image reproduced from [4] showing a polysilicon disk resonator of radius 10μm and thickness 2.1μm actuated by electrodes separated by a 68nm air gap.(left bottom) The two port response shows a resonance at 274MHz with a quality factor of 9100. (right top) Image reproduced from [5] shows a polysilicon disk of radius 6μm separated by a 100nm air gap and (right bottom) two port resonance of a similar device shows a mechanical resonance at 156MHz.

demonstrations were patterned in a deposited polysilicon layer which is around 2.1μm thick. The electrodes surrounding the disk used for actuation are fabricated on a second layer of polysilicon. The electrode polysilicon is separated from the resonator polysilicon by a thin sacrificial layer film which is removed during the release process. The use of a thin film for the air gap definition allows very precise and small gaps down to few tens of nanometers. The radius of

the disk resonator shown in figure 2.3 is 10μm which gives a fundamental resonance frequency of 274MHz. A two port measurement scheme is used to study the response of the devices. A RF signal is applied to the input electrode on one side of the resonator along with a DC bias. When the RF input is at the mechanical resonance of the disk resonator, the radial vibrations that are excited are picked up as a current at the output. A network analyzer is used to observe the power received from the output electrode as the RF input is swept. The ratio of the power received at the network analyzer to the power applied to the device is obtained as the transmission S21. As explained in the earlier section, the RF power obtained is maximum for motional impedance of 50ohms matching the network analyzer impedance. However, since the actual motional impedances of the electrostatically excited mechanical resonators are much larger around a few kilo-ohms, the insertion loss observed in the transmission spectrum at resonance is very high.The insertion losses obtained for the resonators at resonance between 100MHz and 300MHz is between 60dB and 70dB. The problems is made worse as we go to higher frequencies as the motional impedance (2.12) increases with frequency. In addition to the increasing motional impedance, an additional problem is the feed through capacitance. The feed through capacitance is a parasitic capacitance formed between the input and output electrodes bypassing the mechanical resonator. At higher frequencies, the feedthrough capacitance offers an alternate low impedance path from the input to the output. This can be understood in the transmission response as a drowning out of the mechanical response by the parasitic feedthrough as shown in figure 2.4. In order to overcome these limitations and to observe the response of the resonators at higher frequencies, a mixing measurement scheme has been used in previous demonstrations [5, 4]. In order to avoid feedthrough, the input frequency

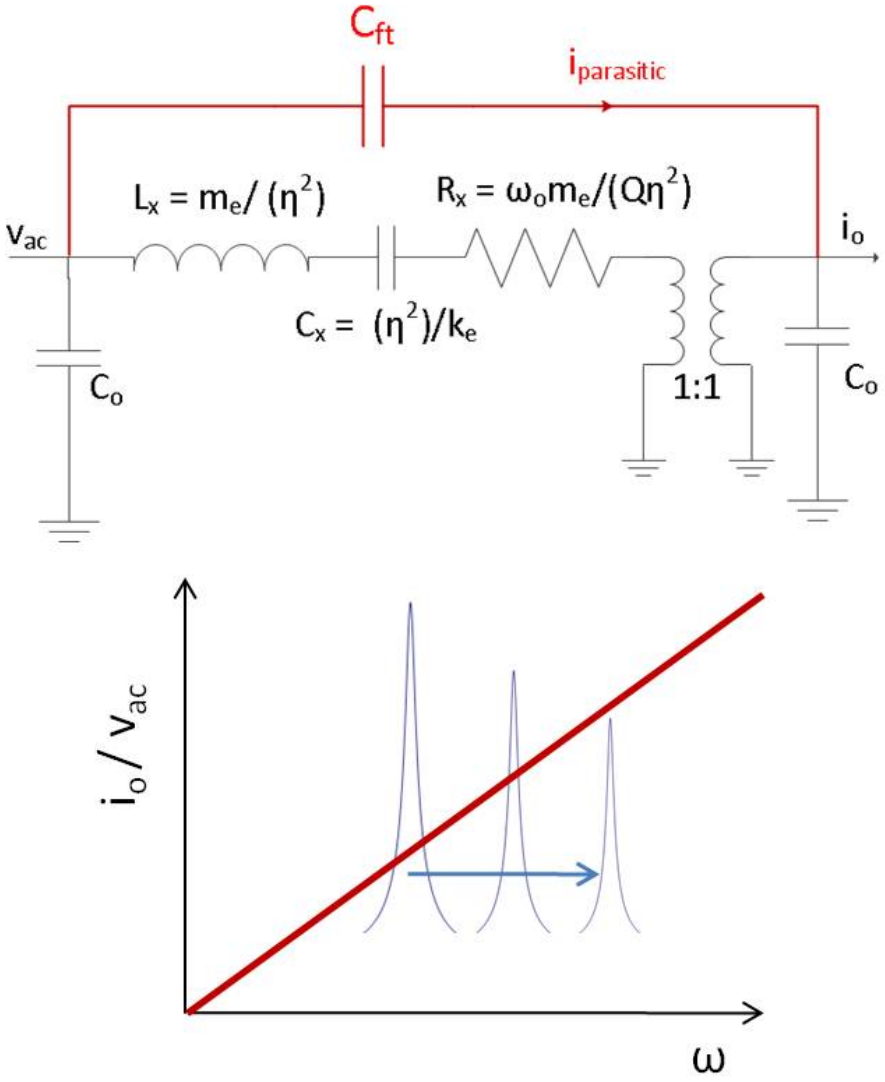

Figure 2.4: (top) Electrical equivalent circuit of the mechanical resonator along with the parasitic feedthrough capacitance.(bottom) The alternate path of lower impedance provided by the feedthrough capacitor is seen by the red line which can be higher than the resonator response at high frequencies

is made different from the output frequency. To obtain a force at the output frequency, a low frequency 'local oscillator' source is used instead of the DC bias. The frequency of the local oscillator is such that $\omega_{IN} - \omega_{LO} = \omega_{OUT}$ which ensures that the force obtained on mixing the two signals on the actuation capacitor results in a force at the output frequency. Using this mixing setup, higher order radial modes of the disk resonator have been measured up to 1.15GHz [4].

In this chapter, the basic equations governing the mechanical resonance frequency of disk resonators have been presented. A scheme for actuation of the micromechanical resonators at the micro scale was analyzed. Previous demonstrations of electrostatically transduced disk resonators on the micro scale have shown two port measurement of mechanical resonances up to 274MHz. The response of the resonator at higher frequencies is hard to obtain with normal two port measurement and need the use of specialized interrogation techniques. This highlights the need for alternate sensing techniques which can overcome the difficulties associated with electrostatic sensing. One such alternate technique, is the use of optomechanical resonators. In the next chapter, the basics of optical resonators are presented and their application as optomechanical resonators for displacement sensing is studied.

CHAPTER 3

OPTICAL RESONATORS

Optical fibers have formed the backbone of communication in the past few decades. Optical fibers act as optical waveguides and carry information at more than a few GB/s. Similar optical waveguides fabricated on the nanoscale on silicon offer to overcome a bottleneck in the field of electronics. As microprocessors have scaled down in size and to higher frequency, most of the energy in the processor is spent in driving the electrical lines of communication inter processor and intra processor. The field of silicon nanophotonics aims to avoid this problem by integrating optical components along with the electrical devices on microprocessors, thereby bringing the advantage that optical communication offers down to the chip scale [27, 28]. The low intrinsic material losses of silicon allows the use of the telecommunication wavelength around 1550nm for these devices. The usual scheme of making optical waveguides consists of defining silicon channels on the device layer of a silicon on insulator (SOI) substrate. The high refractive index of silicon (3.45,) acting as the waveguide core, compared to the index of the buried oxide(1.45) and surrounding air allows for waveguiding in these channel waveguides. Among the fundamental devices that allow for control of light passing through these silicon nanophotonics waveguides is the optical microresonator. Optical resonators are structures that store optical energy at certain wavelengths. A simple optical resonator geometry is the Fabry Perot cavity consisting of two parallel mirrors facing each other. At certain wavelengths there is constructive interference between light reflecting off the two faces and there is a build up of energy inside the resonator. The light in the case of a Fabry Perot cavity forms a standing wave between the two mirror faces and is called a standing wave resonator. Another type of resonator is

a waveguide looped around to form a ring. At certain wavelengths when the path length of light inside the ring corresponds to an integral multiple of the wavelength, there is constructive interference and build up of energy of that wavelength within the ring. Such an optical resonator is a traveling wave resonator as the light is constantly traveling around the ring. The next section will briefly describe the governing equations of optical transmission through an optical resonator following the more detailed analysis presented in [29, 30].

3.1 Dynamics of optical resonator

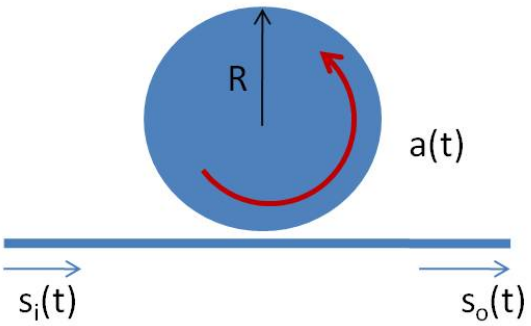

Figure 3.1: Schematic of optical disk resonator evanescently coupled to a waveguide. $|a(t)|^2$ is the total energy inside the resonator while $|s_i(t)|^2$ and $|s_o(t)|^2$ are the total power at the input and output of waveguide.

In this section, the analysis deals with the coupling of light from a waveguide passing next to the optical resonator as shown in figure 3.1. Light is input in the optical waveguide with an amplitude $s_i(t)$ such that $|s_i(t)|^2$ corresponds to the total power input. A part of the mode traveling in the waveguide is outside the waveguide in the cladding. As the waveguide passes by the optical resonator, a part of this mode couples evanescently into the disk resonator mode. The

actual frequencies of resonance for the disk resonator are obtained by solving the Maxwell's equations with appropriate boundary conditions [29]. The mode can then be considered to travel with an effective index n_{eff}. The condition for resonance which specifies the path length to be an integral multiple of the wavelength then becomes

$$m\lambda_o = 2\pi R n_{eff} \tag{3.1}$$

where m is an integer, λ_o is the free space wavelength corresponding to optical resonance and R is the radius of the disk. The right side of the equation corresponds to the optical path length of the optical mode in the disk resonator. The disk supports a traveling wave with amplitude $A(t)$ such that $|A(t)|^2$ is the power flowing through any cross section of the disk at time t. For the analysis, the disk resonator can be considered to be a single mode lumped resonator with energy amplitude $a(t)$ such that $|a(t)|^2$ is the total energy in the disk. The total stored energy and power flow are related by [30]

$$|a(t)|^2 = |A(t)|^2 \frac{2\pi R}{v_g} \tag{3.2}$$

where v_g is the group velocity. The equation for rate of change of the cavity energy with time is obtained by looking at the power coupling into and out of the disk. The decay rate is the power leaving the ring and consists of two components. The power coupled to the waveguide to the transmitted wave is given by the rate $1/\tau_e$. The other decay is due to intrinsic loss such as material absorption and surface scattering and is given by decay rate $1/\tau_i$. The total decay rate $1/\tau$ is the sum of the energy decay rates due to the the two phenomenon and is given by $1/\tau = 1/\tau_e + 1/\tau_i$. The time rate of change of disk energy is then

$$\frac{da}{dt} = \left(j\omega_o - \frac{1}{\tau}\right) a - j\mu s_i \tag{3.3}$$

where μ is the coupling between the waveguide and the disk resonator. The second term on the right hand side shows power coupling into the resonator

from the input waveguide along with a phase factor of -j. The first term corresponds to the phase of the circulating energy along with the decay rate term. The equation for the power at the transmitted port is then

$$s_o = s_i - j\mu a \tag{3.4}$$

The expression for μ can be evaluated by using the decay of the cavity energy in the presence of only the waveguide without any intrinsic losses to be $\mu = \sqrt{2/\tau_e}$. To evaluate the response, let us consider an input at a frequency ω given by $s_i e^{j\omega t}$. The response of the cavity energy is also at the same frequency as represented by $ae^{j\omega t}$ and equation (3.3) can be rewritten as

$$\begin{aligned} \frac{da}{dt} &= \left(-j(\omega - \omega_o) - \frac{1}{\tau_e} - \frac{1}{\tau_i}\right)a - j\sqrt{\frac{2}{\tau_e}}s_i \\ &= \left(-j\Delta\omega - \frac{1}{\tau_e} - \frac{1}{\tau_i}\right)a - j\sqrt{\frac{2}{\tau_e}}s_i \end{aligned} \tag{3.5}$$

where $\Delta\omega = \omega - \omega_o$ is the frequency detuning of the input light with respect to the cavity resonance frequency.

3.2 Transmission at steady state

At steady state, we set the time rate of change of cavity energy to 0 and use equations (3.5) and (3.4) to obtain the power at the waveguide output. The amplitude of energy inside the cavity is then

$$a = \frac{-j\sqrt{\frac{2}{\tau_e}}}{j(\omega - \omega_o) + \frac{1}{\tau}}s_i \tag{3.6}$$

and the amplitude of power at the output

$$s_o = \frac{j(\omega - \omega_o) + \frac{1}{\tau_i} - \frac{1}{\tau_e}}{j(\omega - \omega_o) + \frac{1}{\tau}}s_i \tag{3.7}$$

Additionally, quality factors can be defined which correspond to ratio of the energy stored in the resonator to the rate of energy dissipation from the resonators due to the particular loss mechanism. The quality factor Q is related to the rate of energy loss due to loss effects $1/\tau$ by [29]

$$\begin{aligned} Q_i &= \frac{\omega_o \tau_i}{2} \qquad Q_e = \frac{\omega_o \tau_e}{2} \\ Q_{tot} &= \frac{1}{\left(\frac{1}{Q_i} + \frac{1}{Q_e}\right)} \\ Q_{tot} &= \frac{\omega_o}{2} \frac{1}{\left(\frac{1}{\tau_i} + \frac{1}{\tau_e}\right)} = \frac{\omega_o \tau}{2} \end{aligned} \tag{3.8}$$

The transmission at the output of the waveguide defined as the ratio of the

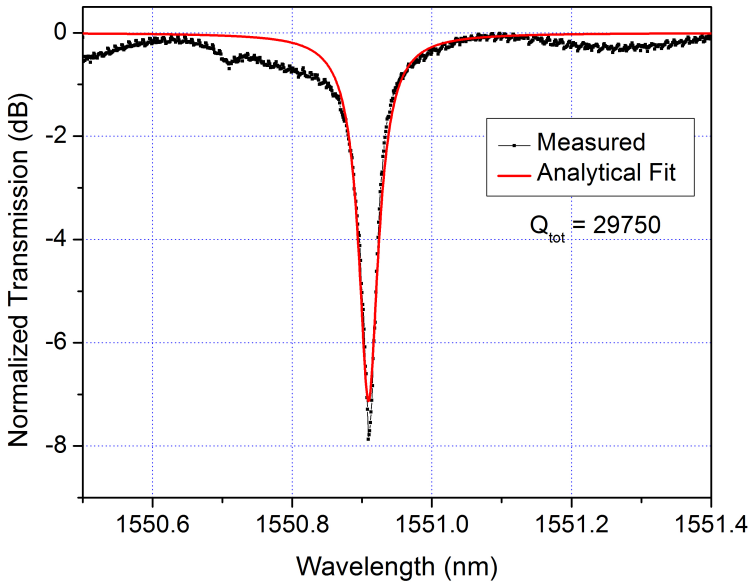

Figure 3.2: Normalized optical transmission at the output past a typical optical resonator (black) along with the analytical fit from (3.9) (red) for a loaded quality factor of 29,750

output to the input power obtained using (3.7) and (3.10) is

$$T = \left|\frac{s_o}{s_i}\right|^2 = \frac{4(\omega - \omega_o)^2 + \omega_o^2 \left(\frac{1}{Q_i} - \frac{1}{Q_e}\right)^2}{4(\omega - \omega_o)^2 + \omega_o^2 \left(\frac{1}{Q_i} + \frac{1}{Q_e}\right)^2} \tag{3.9}$$

Figure 3.2 shows a typical transmission spectrum measured by using a tunable laser to sweep across the wavelengths and observing the output on a photodiode. There is a drop in transmission when the input laser wavelength corresponds to the disk resonance wavelength. The depth of the dip is determined by Q_i and Q_e and the transmission at resonance goes to 0 when $Q_i = Q_e$. This condition is called the condition for critical coupling. While Q_i is determined by the intrinsic losses in the disk, Q_e in this system can be adjusted in the design process by controlling the spacing between the coupling waveguide and the disk. The other feature of the resonance that is of particular interest is the full width at half maximum (FWHM). The quality factor is inversely proportional to the FWHM $\Delta\lambda$ and can be evaluated using the expression

$$Q_{tot} = \frac{\Delta\lambda}{\lambda_o} \tag{3.10}$$

A high quality factor resonance would be characterized by a very sharp resonance and small FWHM.

3.3 Optomechanical Resonators

3.3.1 Optomechanical Coupling Constant

The disk optical resonator can be converted into an optomechanical resonator by releasing the disk from the substrate and allowing a mechanical resonance mode to co-exist with the optical resonance mode. Figure 3.3 shows a schematic of a disk resonator that is coupled to a waveguide and sustaining the first radial vibrational mode corresponding to a time varying radial displacement. On a change in the radius of the disk, the optical path length seen by the light travel-

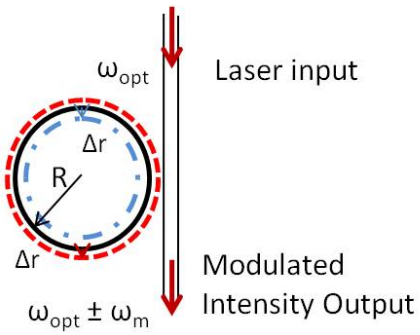

Figure 3.3: Schematic of radial changes of an optomehanical resoantor coupled to a waveguide

ing around the disk changes. This in turn changes the condition for resonance specified by equation (3.1) into

$$m\left(\lambda_o + \Delta\lambda_o\right) = 2\pi\left(R + \Delta r\right) n_{eff} \tag{3.11}$$

where $\Delta\lambda_o$ is the change in the optical resonance wavelength. Rearranging the terms, we obtain

$$\frac{\Delta\lambda_o}{\lambda_o} = \frac{\Delta r}{R} \tag{3.12}$$

Expressing equation (3.12) in terms of frequency and taking limit $\Delta r \to 0$

$$\frac{d\omega}{dr} = -\frac{\omega_o}{R} \tag{3.13}$$

This relation is a measure of the change of the optical resonance frequency to a small change in the radius of the resonator and is also called the optomechanical coupling constant g_{om} [13]. A larger g_{om} would give a larger change in the optical resonance frequency for a given displacement, thus making the optical system more sensitive to displacement. The optical resonator can be considered to be converting the phase change caused by the radial displacement into an amplitude response at the output. To estimate the amplitude change, we go back to the equation for rate of change of energy in the cavity given by (3.5).

As the optical resonance frequency is a function of the radial displacement, the optomechanical coupling appears in the form of a time varying detuning in this equation. If the input laser is biased such that the initial detuning is $\Delta\omega_{intial}$, then on a small radial change r, using equation (3.13)

$$\begin{aligned}\Delta\omega &= \omega - \left[\omega_o + \left(\frac{d\omega_o}{dr}\right)r\right] \\ &= \Delta\omega_{initial} - \left(\frac{d\omega_o}{dr}\right)r \\ \Delta\omega &= \Delta\omega_{initial} + \frac{\omega_o}{R}r\end{aligned} \tag{3.14}$$

The radial displacement r can correspond to the radial vibrational mode in which case it can be obtained by using a simple mass spring damper resonator system.

The optomechanical resonator can thereby be described by the following three set of equations

Mechanical Resonator

$$\frac{d^2r}{dt^2} + \frac{\omega_m}{Q_m}\frac{dr}{dt} + \omega_m^2 r = \frac{F}{m_{eff}} \tag{3.15}$$

Optomechanical Coupling

$$\Delta\omega = \Delta\omega_{initial} + \frac{\omega_o}{R}r \tag{3.16}$$

Optical Resonator

$$\frac{da}{dt} = \left(-j\Delta\omega - \frac{1}{\tau_e} - \frac{1}{\tau_i}\right)a - j\sqrt{\frac{2}{\tau_e}}s_i \tag{3.17}$$

3.3.2 Displacement Sensitivity

Figure 3.4 represents the changing transmission due to changing optical resonance caused by radial vibrations. The quality factor of the optical resonance

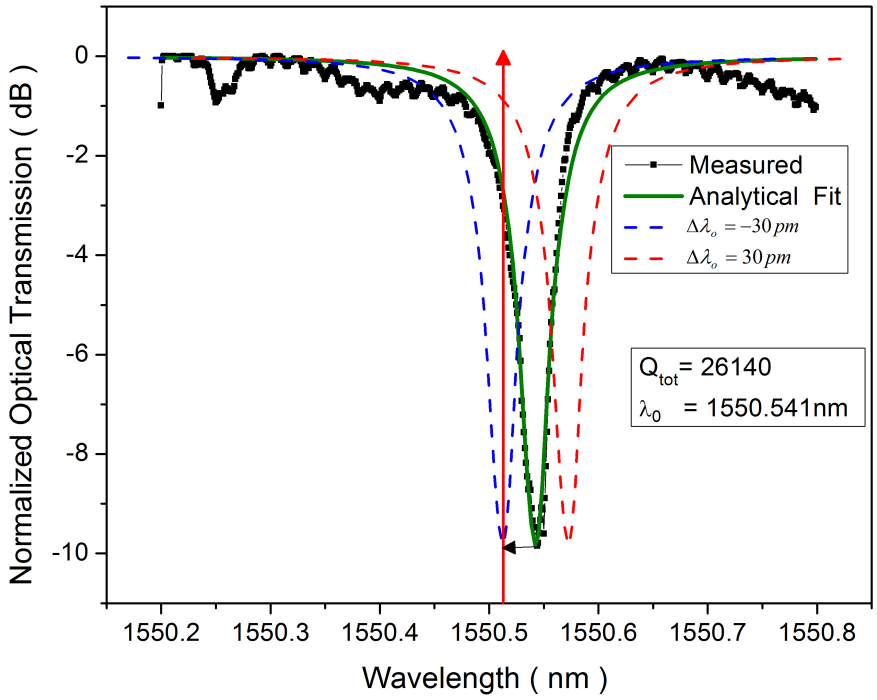

Figure 3.4: Normalized optical transmission (black) at the output past a typical optomechanical resonator along with the analytical fit(green). On increasing radius by 0.2nm, the optical resonance increases by 30pm(red) and on decreasing radius by 0.2nm optical resonance decreases by 30pm(blue).

shown in the figure is that of a typical optomechanical silicon disk resonator. The input laser wavelength is biased at the half maximum point of optical resonance. The modulation of transmission is property of not only the optomechanical coupling constant but is also dependent on the optical quality factor of the resonance. At high quality factors, the slope of the transmission curve with respect to wavelength is steep, and small changes in resonance wavelength appear as large changes in the transmission at the output. For the transmission spectrum shown in figure 3.4, the quality factor is 26,140 which gives a λ_{FWHM} =59pm. Using equation (3.12), a optical resonance wavelength shift $\Delta\lambda_o$

of 30pm is obtained for a radial displacement amplitude of 0.2nm. When the radius reduces by 0.2nm, the resonance wavelength would blue shift by 30pm thereby turning off the transmission at the output. On an increase in the radius by 0.2nm, the resonance wavelength would increase by 30pm and the transmission would turn completely on. We define the extinction ratio to characterize the amount of modulation and define it as the ratio of the maximum to the minimum transmission. The maximum extinction ratio possible for the current system is determined by the strength of coupling of the optical resonator to the waveguide. In the case of the resonator whose transmission spectrum is shown in figure 3.4, the maximum extinction ratio that can be achieved is equal to 10dB which is the depth of extinction at optical resonance. Critical coupling between the resonator and waveguide is preferred to achieve maximum modulation. Figure 3.5 shows the expected extinction ratio as a function of radial displacement amplitude for the optical resonator with quality factor of 26,140 and an extinction at optical resonance of 10dB. This figure is obtained by simulations using the equations in the earlier section. The actual displacement sensitivity of the system is determined not just by the extinction for a given radial displacement, but also by the power at the output. For a radial displacement of 90pm of the 10μm radius disk an extinction of 3dB is obtained. For this extinction, an average power of 1mW at the output would correspond to an output power modulation of 500μW. However, if we only had 10μW at the output, then the output power modulation is only 5μW making the displacement much harder to detect. For an optical detector with a responsivity of 1A/W and terminated by 50Ω, we obtain radio frequency electrical power at the output of 12.5μW when the optical power modulation is 500μW. The limit of motion detection sensitivity is thus determined by the minimum power that can be detected

considering the noise at the detector. Typical detector sensitivities of the 1647 Avalanche photo diode allows for detection of 1.6 pW per root hertz of optical power over the sensing bandwidth. This optical power sensitivity can allow for mechanical displacement sensitivities of a few fm per root hertz.

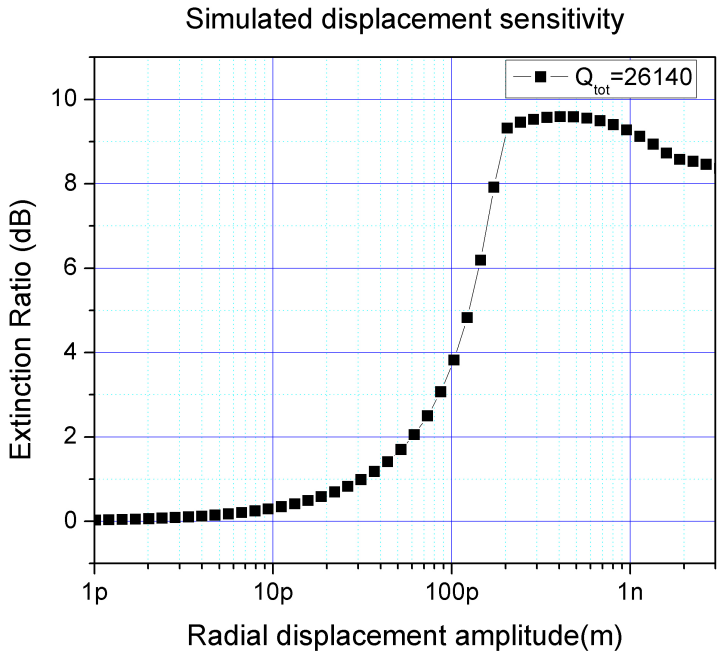

Figure 3.5: Simulated extinction ratio as a function of radial vibration displacement amplitude for an optomechanical resonator with loaded quality factor of 26,140 as shown in figure 3.4

3.3.3 Sensing bandwidth

In the analysis presented above, light is considered to respond instantaneously to any radial displacement changes. To verify this assumption, the optical cavity lifetime needs to be calculated. The cavity lifetime is a measure of the time

taken for the optical system to respond to a changing stimulus. The optical cavity lifetime is specified by $\tau_{opt} = 2Q_{opt}/\omega_{opt}$. For typical silicon optomechanical systems, the quality factor of the resonance is 30,000 around 1550nm which gives us a lifetime of 49ps. This lifetime is much smaller than the time period of mechanical radial vibrations. The vibrations which are typically between 10MHz upto a GHz have time periods ranging from 100ns to 1ns which is much larger than the cavity lifetime of 49ps. As the time period of mechanical oscillations gets closer to the optical cavity lifetime, the optical cavity is unable to respond to the changes fast enough and we observe a decrease in the sensitivity. For a cavity with a lifetime of 49ps, this occurs when the mechanical oscillation time period is around 100ps which corresponds to a frequency of 10GHz.

3.4 Electrostatic Actuation of optomechanical resonators

Ideally, it would be best to have a single disk optomechanical resonator which supports an optical mode and whose mechanical motion can also be electrostatically actuated. However, the closely spaced electrodes required for actuation of the mechanical motion would prevent the optical mode from existing in the disk. The evanescent field existing outside the disk resonator would couple light into the electrodes. To prevent this, a coupled disk geomtry is chosen for fabrication of the acousto-optic modulator as shown in figure 3.6. The device consists of a optomechanical and mechanical disk resonator fabricated in the device layer and buried oxide of the SOI substrate. The two resonators are mechanically coupled to each other through a coupling beam in the buried oxide to transfer the vibrations excited in the mechanical resonator to the optomechanical resonator.

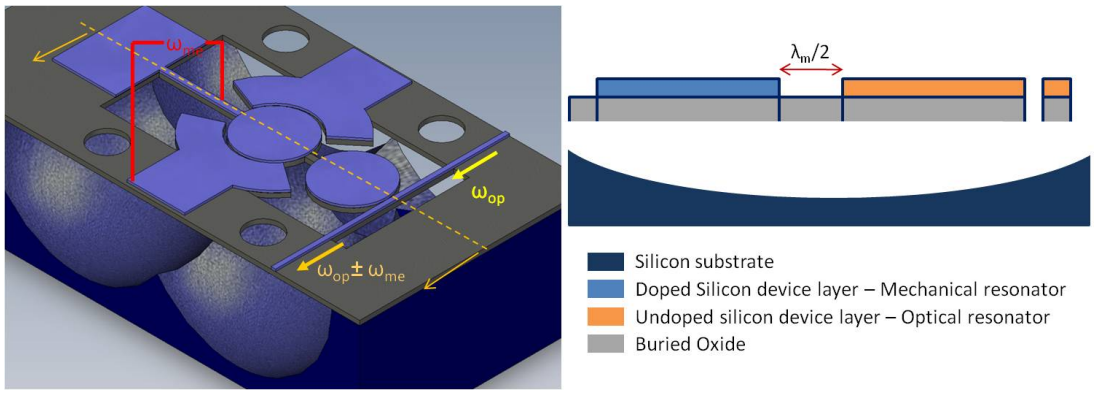

Figure 3.6: Schematic for device for electrostatic actuation of optomechanical resonators. The disk on the left has electrodes for actuating mechanical motion and it mechanically coupled to the optomechanical resonator on the right by a coupling beam in the buried oxide.

A thin buried oxide SOI wafer is chosen to fabricate these devices. This choice is due to the fact that the silicon and buried oxide stack needs to be etched all the way down to the substrate silicon in order to mechanically release the structures. A thick buried oxide would make the aspect ratios between the electrode-resonator spacing (150nm) and the silicon-buried oxide stack very large and prevent etching all the way down till the substrate silicon. As a first step to fabrication of the modulator, a process was developed to demonstrate optical structures on thin buried oxide SOI substrates.

3.5 Nanophotonic devices on thin buried oxide SOI

3.5.1 Motivation

Traditionally, silicon nanophotonic strip waveguides are made on SOI with a thickness less than 260 nm and buried oxide thickness greater than or equal to 1 μm [31, 32, 33]. The waveguide width is defined lithographically and etched into silicon with a width less than 500 nm to ensure single-mode operation. The propagation loss reported for such waveguides is between 1-5 dB/cm [31, 32] with values smaller than 1 dB/cm reported for waveguides made using oxidation smoothing [33]. The buried oxide on which the waveguide rests acts as a barrier preventing light leakage into the substrate and needs to be greater than 1m to keep the substrate leakage loss to a value lower than 1 dB/cm [34, 35]. Commercial silicon-on-insulator (SOI) complementary metal oxide semiconductor (CMOS) electronics on the other hand relies on thin buried oxide to reduce short channel effects [36] and avert thermal problems [37] . For integration of waveguides on the same layer as SOI based CMOS, the thickness of buried oxide under the waveguides needs to match that used for electronics. The buried oxide for electronics is thinner and ranges from 100nm [38] to 400nm [39].It has been shown previously through simulations [35] that these buried oxide thicknesses would give losses > 100dB/cm for the strip waveguides.

3.5.2 Fabrication

Optical waveguiding on thin buried oxide SOI wafers is achieved using a technique of localized substrate removal. A buried oxide thickness of 400nm is

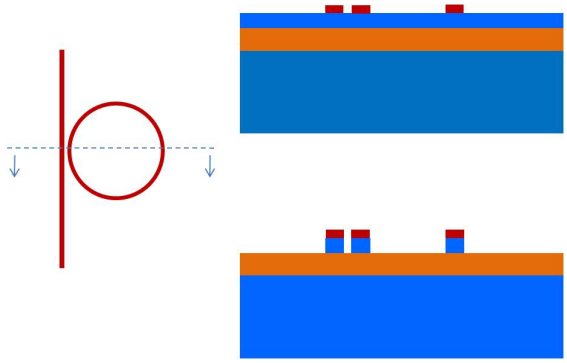

(a) Patterning of e-beam resist and transfer of pattern to silicon device layer

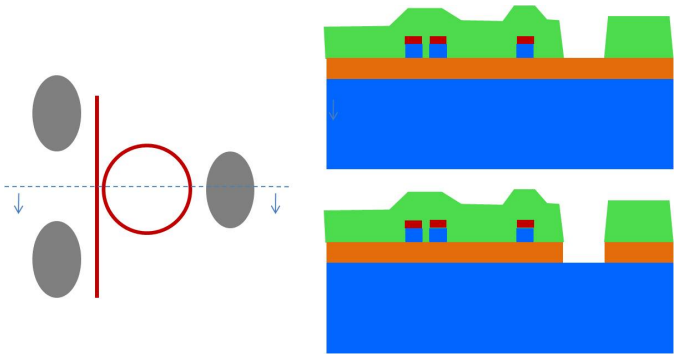

(b) Photoresist patterned to protect silicon device layer and to open windows for localized substrate removal follwed by buried oxide etch using CHF_3/O_2 RIE to access substrate silicon

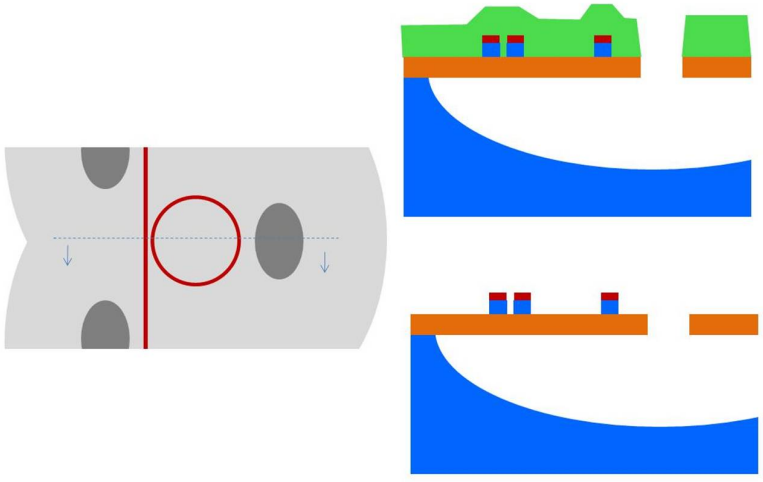

(c) Substrate removal through XeF_2 etch and final device cross-section after photoresist strip

Figure 3.7: Process flow for optical waevguides and resonators on thin buried oxide SOI

chosen due to ready availability. After patterning of the device layer to obtain waveguides, the substrate silicon is removed with an isotropic dry etch using xenon difluoride (XeF2) gas[40].The approach followed is similar to that used to fabricate polysilicon waveguides above the trench isolation layer of a CMOS process [41].

The waveguides and ring resonators are fabricated on the 250 nm thick device layer of a SOITEC SOI substrate with a buried oxide thickness of 400 nm as shown in Fig. 3.7. HSQ based negative e-beam resist (XR-1541) of thickness 130 nm is spin coated on top of the device layer. Waveguide are patterned on the resist using a JEOL 9300 e-beam lithography system and developed in AZ 300 MIF developer. The patterns are transferred to the silicon device layer using a Cl_2 based Inductively Coupled Plasma(ICP) based Reactive Ion Etch (RIE). Photoresist is then spin coated to a thickness of $3\mu m$ and substrate removal etch windows are patterned using a 5x i-line stepper. The etch windows are elliptical and are spaced 3 m away from the waveguides. These windows are etched into the oxide using an RIE with CHF_3/O_2 gases.The wafer is then diced before the substrate removal etch to allow for coupling through the ends of the waveguide. The substrate removal is performed in a XACTIX etcher by a pulsed xenon difluoride (XeF_2) etch recipe to obtain a lateral undercut of $15\mu m$. The openings in the oxide act as windows for XeF_2 gas to reach the substrate. The undercut of silicon is decided depending on the desired air gap below the waveguide, the spacing between each of the etch windows and the spacing between etch windows and the waveguide. The photoresist protecting the device layer is removed after the XeF_2 etch by the use of oxygen plasma. Fig. 3.8 shows the SEM of a waveguide obtained with this process.The SEM shows an undesired undulation of buried oxide below the waveguides. The ripples on the buried oxide can be reduced

by making the etch holes closer to the optical structure and removing a smaller region of substrate silicon thereby making the suspended region smaller.

Etch hole placement

The xenon di fluoride etch is an isotropic etch. The etch holes need to be spaced such that the depth of silicon removed below the optical devices is large enough to reduce the optical losses. For shorter etches of a few microns, the etch holes need to be placed closer to the center of the device. For the waveguides fabricated, the holes were placed 3um to the device in order to accommodate for lithographic misalignment between the silicon device layer mask and the etch hole mask. The size of the opening is limited by the process parameters of depth of etch and etch rate required. The requirement for etch holes can limit the density of integration. However, compared to competing methods, having a single substrate substantially reduces the total footprint and the need for flip chip bonding, area for bond pads etc.

3.6 Experimental Setup

The transmission of light through the waveguides is measured for both quasi-TE and TM to characterize the waveguides and resonators. Light from a tunable laser is coupled into the waveguides via a polarization controller with the help of a tapered lensed fiber. The waveguides have a nanotaper[42] at the ends to convert the optical fiber mode into the waveguide mode. A SEM of a nanotaper is shown in figure 3.9. The light coming out of the waveguide is collected through a 40 microscope objective and focused on a detector via a polarizer. A

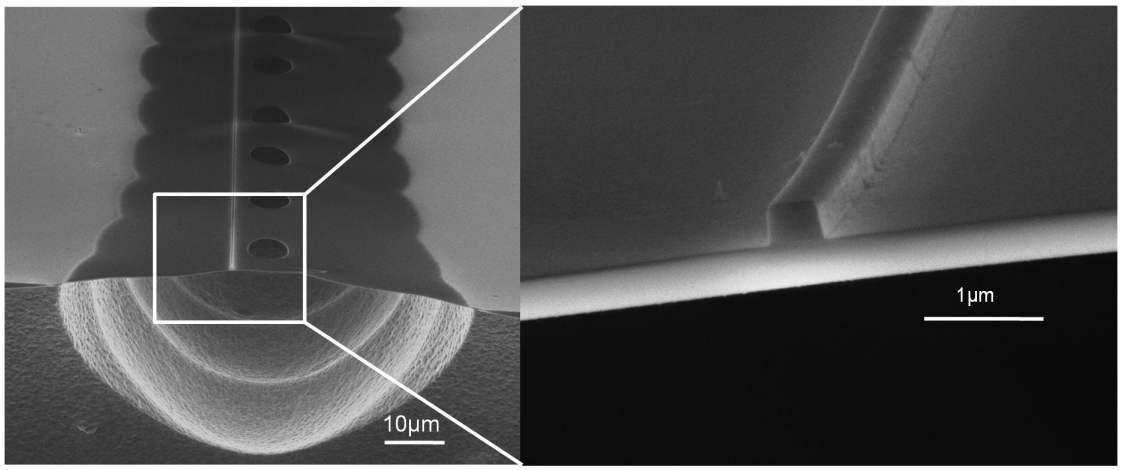

Figure 3.8: (left) SEM of waveguide showing etch windows in buried oxide and pits in substrate silicon created by XeF_2 etch, (right) Close-up of 250 nm silicon waveguide (with XR on top) resting on a 400 nm membrane of buried oxide.

loss of 18 dB is obtained from laser input to the detector for waveguides of 9 mm in length.

3.6.1 Results

Characterization of waveguide loss

We obtain propagation losses using a cutback method [32] by fabricating meandering waveguides of different lengths. The number of bends for each of the waveguides is kept constant and the length of the straight section is increased in order to obtain waveguides of different length .The cutback method is limited by the variations in coupling loss to different waveguides. Fig.3.10(a) and Fig.3.10(b) shows the data obtained from 2 different chips from the same wafer for waveguide loss measurement. The loss obtained from the slope of the lin-

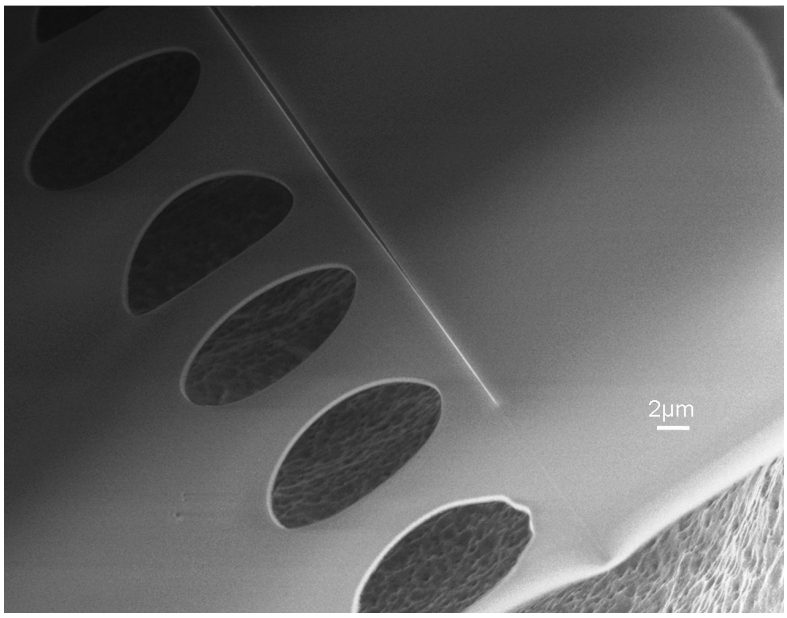

Figure 3.9: SEM of nanotaper for coupling from lensed fiber into waveguide.

ear fit is 3.88 dB/cm for the quasi-TE and 5.06 dB/cm for the quasi-TM mode. This loss is comparable to silicon waveguides fabricated on buried oxide with thickness ¿ 3μm [32] showing that the loss due to substrate leakage has been eliminated in our process. The effective index obtained using COMSOL FEM software for the quasi-TE mode is 2.405 and the quasi-TM mode is 1.862 at λ_o=1550nm

Coupling loss at the nanotaper

The fiber mode is coupled into the waveguide mode by an inverted nanotaper as shown in fig. 3.9. The waveguide is tapered in a parabolic fashion from a size of 90nm at the tip to the waveguide width of 450nm over a distance of 40m [42] . The loss for two of the nanotapers corresponds to the intercept of fig.3.10(a) and fig.3.10(b). The intercept for the TE mode is -14.77 dB corresponding to a loss

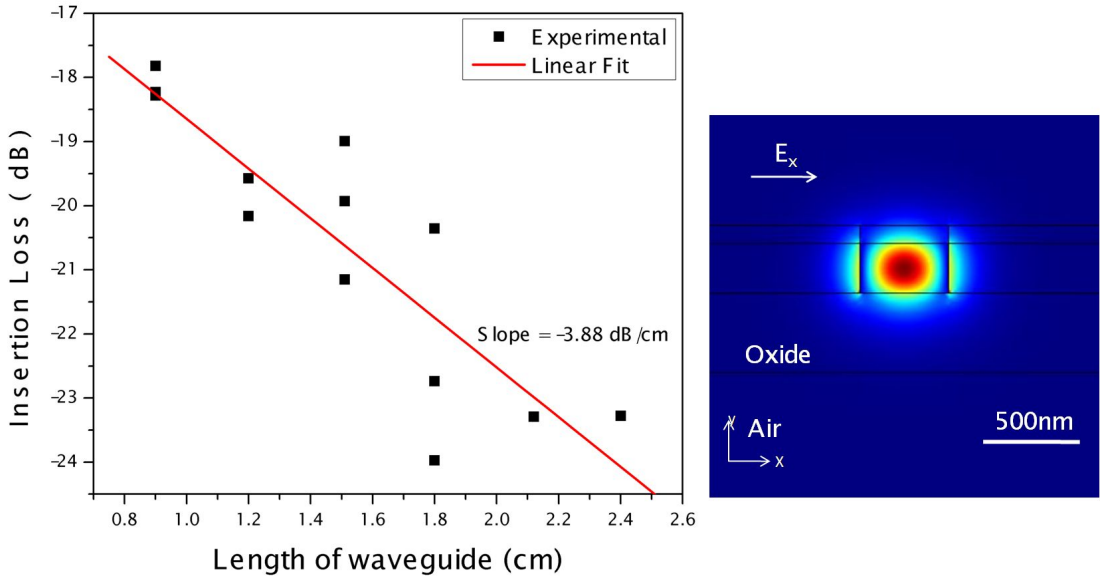

(a) (left) Insertion loss for different waveguide lengths for quasi-TE mode. (right) Optical mode profile for the quasi-TE mode with effective index neff = 2.405 calculated using COMSOL FEM software.

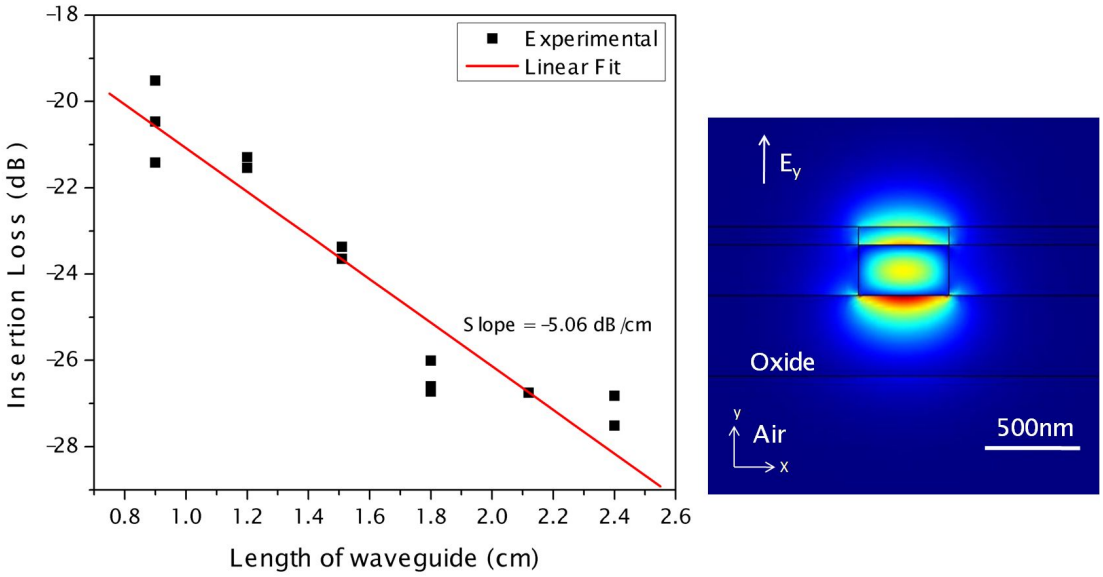

(b) (left) Insertion loss for different waveguide lengths for quasi-TM mode. (right) Optical mode profile for the quasi-TM mode with effective index neff = 1.862 calculated using COMSOL FEM software

Figure 3.10: Cutback method for characterization of waveguide loss

of 7.385 dB per taper and for TM mode is -16.02 dB which gives a loss of 8.01 dB per taper. As seen from the SEM in Fig. 3.9, the nanotaper is etched 15μm from the chip edge by the XeF2 etch. This is because of insufficient photoresist coverage at the edge exposing the tip of the taper to the etching gases. The input light is focused using a tapered lensed fiber held flush with the edge of the chip and having a focusing distance of 14μm. The width of the taper at the focus is not optimal for coupling into the waveguide mode and leads to high losses. This loss can be reduced in the future by slightly recessing the nanotaper from the edge of the chip thereby ensuring better protection by the photoresist.

Ring resonators

Resonance for quasi TM mode

The transmission spectrum of ring resonators was obtained by sweeping the tunable laser and recording the output of the waveguides from the detector onto a computer. The transmission spectrum for the quasi-TM mode for a ring resonator of radius 7.5μm with a width of 450 nm and spaced 400 nm away from the waveguide is shown in Fig. 3.11. The free spectral range (FSR), which corresponds to the wavelength spacing between different orders of the optical resonance, is used to calculate group index n_g using $n_g = \lambda_o^2/(FSR.L)$ [43], where λ_o is the free space wavelength and L is the length of the resonator . The measured free spectral range is 10.44 nm from which the group index is calculated to be 4.92 around 1557.6 nm.

The loaded optical quality factor Q_opt of 46,500 is obtained for the resonance shown in Fig. 3.12 by fitting a Lorentzian. At critical coupling the intrinsic qual-

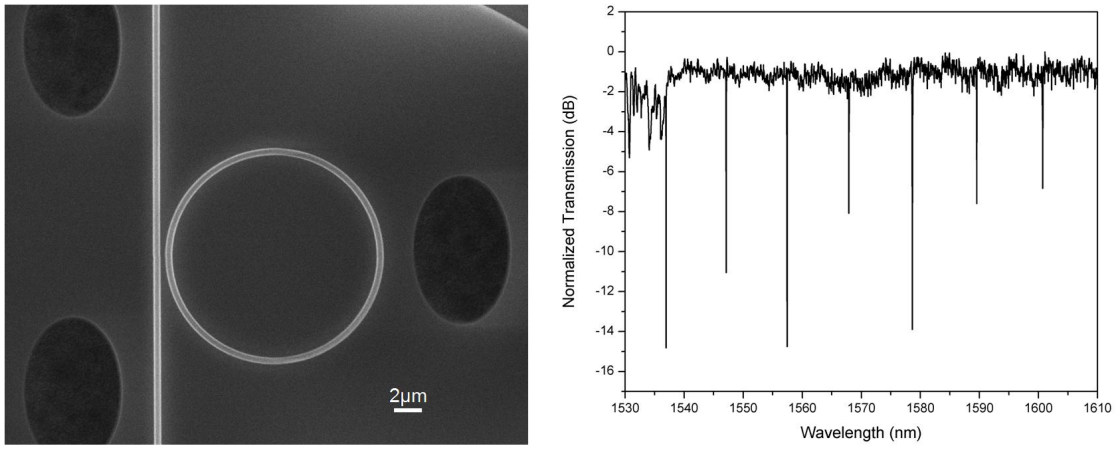

Figure 3.11: (left) SEM of ring resonator of 7.5μm radius spaced 400 nm away from the waveguide (right) Normalized transmission spectrum of the ring resonator for the quasi-TM mode.

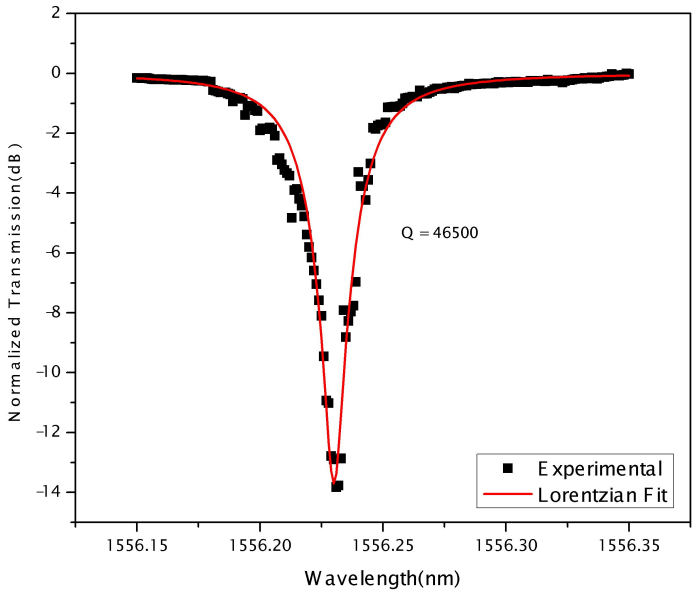

Figure 3.12: Normalized transmission for the quasi-TM resonance mode with a loaded quality factor of 46,500 and an extinction of 14 dB.

ity factor is double the loaded quality factor giving an intrinsic quality factor of 93,000. Under critical coupling condition, the losses in the ring are calculated from the intrinsic quality factor using [30, 43]

$$Q_{loaded} = \frac{Q_{intrinsic}}{2} = \frac{\pi n_g}{\lambda_o \alpha} \tag{3.18}$$

where α is the total propagation loss per unit length in the ring, and n_g is the group index. The loss per unit length for the ring for a loaded Q of 46,500 is 9.28 dB/cm. This loss for the quasi-TM waveguides is slightly higher to the losses that extracted from the cuback method as these include the radiation loss in the curved resonator.

Resonance splitting for Quasi-TE mode

The transmission spectrum for a quasi TE resonance of a 7.5 m radius ring with a width of 450 nm and 150 nm spacing from the waveguide is shown in Fig. 3.14. A split resonance is obtained with a center wavelength of 1544.8 nm, a separation of 0.085 nm and an extinction ratio of 12 dB for each of the dips. Split resonances have been observed in ring resonators due to mode coupling between the clockwise and anticlockwise travelling modes [44]. The mode coupling is caused by surface roughness which is introduced due to imperfections on the resist and etching process. The mode coupling is caused by surface roughness which is introduced due to imperfections on the resist and etching process. The transfer function for the transmitted power to the input power is given by [44, 45]

$$T(\omega) = \left| 1 - \frac{1}{2Q_e} \left(\frac{1}{j\left(\delta + \frac{1}{2Q_u}\right) + \frac{1}{2Q_i} + \frac{1}{2Q_e}} + \frac{1}{j\left(\delta - \frac{1}{2Q_u}\right) + \frac{1}{2Q_i} + \frac{1}{2Q_e}} \right) \right|^2 \tag{3.19}$$

where $\delta = (\omega - \omega_o)/\omega_o$, Q_i is intrinsic quality factor determined by loss per unit length in the ring, Q_e is coupling quality factor determined by the rate of coupling of the mode to the waveguide and Q_u is the mutual coupling quality factor which is controlled by the coupling between clockwise and anticlockwise propagating modes within the ring resonator. Eqn. 3.19 assumes that the two coupled resonances modes have the same resonance frequency and quality factor.

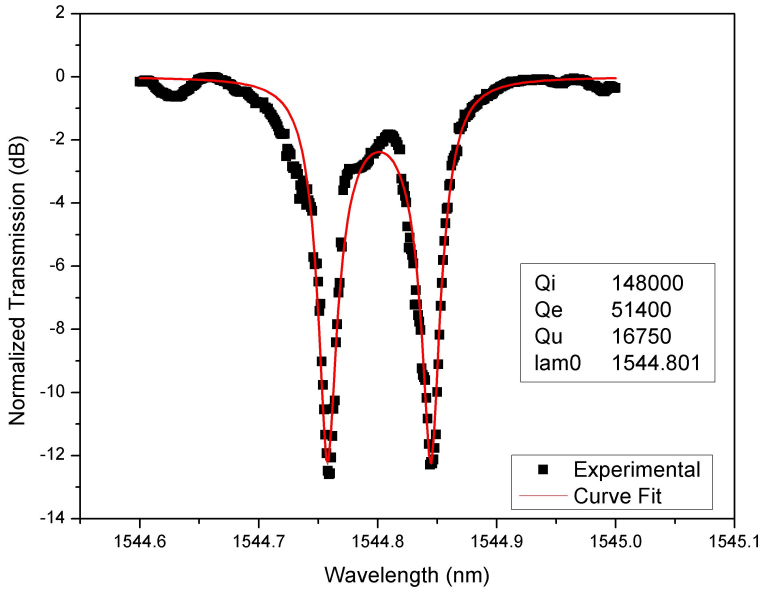

Figure 3.13: Normalized transmission for a quasi-TE resonance mode with the label describing the parameters obtained from fitting the measured data to Eqn.(3.19)

The free spectral range observed for the resonances is 11.15 nm and gives a group index of 4.54. The intrinsic quality factor obtained by fitting the measured transmission spectrum to Eq.(3.19) is 148,000. The propagation loss per unit length obtained from the intrinsic quality factor using Eq.(3.18) is 5.43 dB/cm.

Thermal nonlinearities are also observed in the resonators at input powers

of a hundred microwatts. This is because of the high optical quality factors and the only path of heat removal being along the buried oxide to the point where the oxide membrane is anchored to the substrate. By making the etch depth smaller and the etch holes closer, the path for heat leakage to the substrate can be shortened and the effect of nonlinearities can be reduced.

3.7 Mechanical resonators on thin buried oxide SOI: Challenges

In order to obtain the mechanical resonators shown in figure 3.6, the patterns on the device layer need to be etched right through the buried oxide after etching the top silicon layer. In addition, the top silicon layer needs to be protected during the buried oxide etch. Etching of the silicon in the Cornell nanofabrication facility requires an oxide hard mask. Additionally,in order to protect the silicon during the buried oxide etch after device layer definition, the thickness of the top oxide hard mask needs to be at least as thick as the buried oxide. As we need to etch 150nm gaps between the resonator and electrode down into the buried oxide, the aspect ratio in the gaps becomes too large for the oxide etchers to work effectively as shown in figure **??**. This prevents the release of the silicon - buried oxide sandwich structures for mechanical vibration.

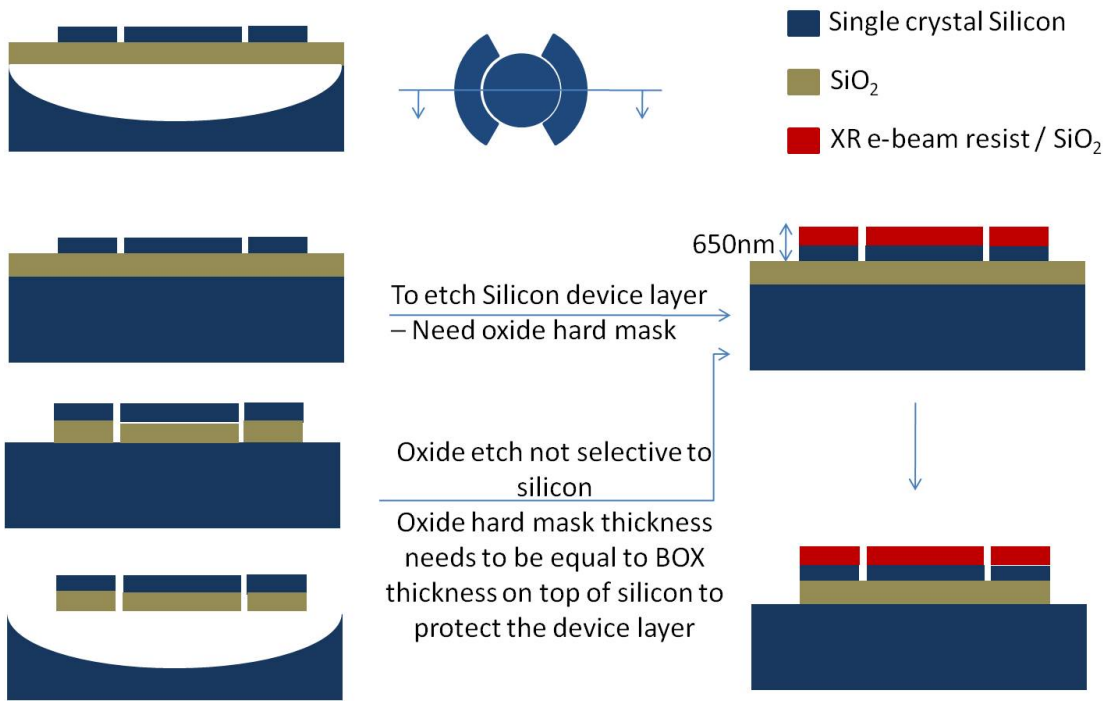

Figure 3.14: Fabrication challenges in etching through the buried oxide of the mechanical structures while protecting the silicon device layer. The topmost structure shows the devices achieved using the technique developed for nanophotonic structures on thin box SOI. The steps on the left need to be performed in order to get to the structure on the lower left. However due to fabrication challenges we end up with a structure as shown in lower right where the buried oxide is not etched in the gaps.

CHAPTER 4

ACOUSTO OPTIC MODULATOR

In the previous chapters, the scheme of electrostatic transduction of mechanical motion has been presented. The problems with sensitivity of the electrostatic transduction especially at higher frequencies has prevented its application in applications such as oscillators and filters. An optical scheme of sensing motion using optomechanical resonators was then presented. The optomechanical resonators offer increased sensitivity and higher frequency operation compared to electrostatic sensing. A fabrication process was then proposed for making these structures on the device layer of thin buried oxide silicon on insulator substrates. As a first step, optical waveguides and resonators with high quality factors were demonstrated on this substrate. However, fabrication challenges prevented extension of the process to fabricate optomechaical structures on the thin buried oxide substrates. In this chapter, a modified device schematic is presented followed by a fabrication process for the same and results obtained for this device.

In the optical sensing scheme, we are observing the optical modulation caused by mechanical vibrations driven by the electrical input. The mechanical vibrations are excited only when the electrical input is at the mechanical resonance frequency. Therefore the optical modulation is expected to be observed only for a narrowband electrical input around the mechanical resonance frequency. In this chapter, we refer to this narrow band optical modulator as an acousto-optic modulator.

4.1 Schematic and Structure

Fig.4.1 shows the schematic of the proposed electrically actuated optomechanical resonator consisting of two suspended microdisk resonator similar to the scheme presented earlier.The microdisk resonator on the left has electrodes around it to provide the electrostatic actuation force for driving mechanical motion. The difference in the schematic here, is that the optical and mechanical structures are fabricated only on the device layer of thick buried oxide SOI (3μm). The structures are released by removing the buried oxide below the disks leaving behind a pedestal of oxide holding the disk at the center.

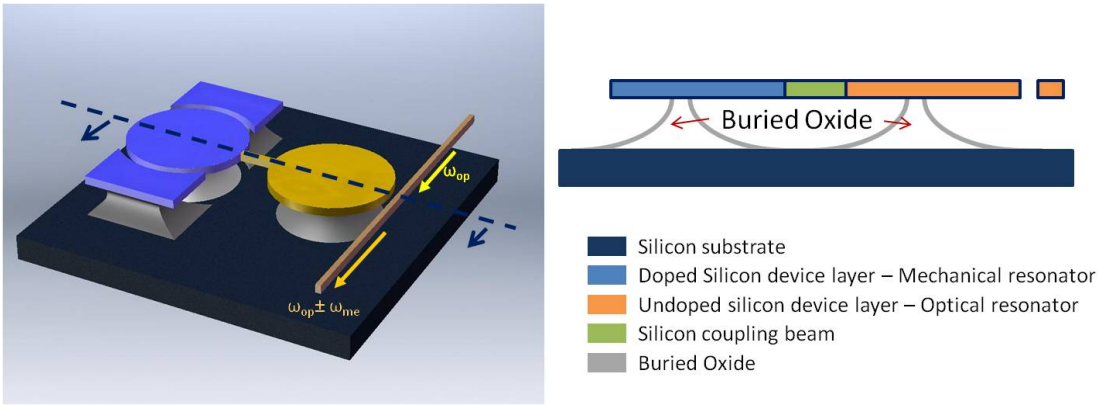

Figure 4.1: Schematic of the Acousto optic modulator on thick buried oxide

4.1.1 Optomechanical resonators on thick buried oxide SOI

The advantages of switching to thicker buried oxide SOI optomechanical system include easier fabrication of the optical waveguides and mechanical resonators. The thicker buried oxide of 3μm offers excellent optical isolation for light in the

silicon device layer from the silicon substrate. Switching to the thick buried oxide SOI eliminates the need to remove the substrate silicon from below the optical structures. For the mechanical structures, which involve a closely spaced electrode, the device etch only needs to go upto the top of the buried oxide. This is simpler to achieve and has lower aspect ratios compared to the initial fabrication process on thin buried oxide SOI which involved etching the device structures right upto the base of the buried oxide. The one disadvantage of switching, however, is the coupling beam which can no longer be in the buried oxide and needs to be in the silicon device layer. The silicon coupling beam can be a scattering point for the optomechanical resonator and reduce the optical quality factor of some modes.

4.1.2 Principle of Operation

This section recaps the content of the earlier chapters for the particular case of the acousto optic modulator. Figure 4.2 shows another schematic of the actual acousto optic modulator layout. The electrodes on the disk on the left provide the driving force for mechanical motion. This force is obtained from equation (2.8). The presence of the mechanical coupling beam splits the fundamental radial vibrational mode into two modes of the coupled disk system. The first mode is when the radial displacement in the two disks are out of phase with each other and the second mode is when the two are in phase with each other. The combination of the two mechanical modes and the coupling beam result in a filter response to the electrical input with the bandwidth being tunable by the characteristics of the coupling beam. The separation in the frequency of the two modes is determined by the stiffness of the coupling beam. When the force is

at either of these mechanical frequencies, we obtain radial displacement in both the disks. This radial displacement leads to a change in the optical resonance wavelength by $\Delta\lambda_o = (\Delta r/R)\lambda_o$. When the wavelength of the tunable laser input to the waveguide is set around the optical resonance wavelength, we obtain optical modulation at the output.

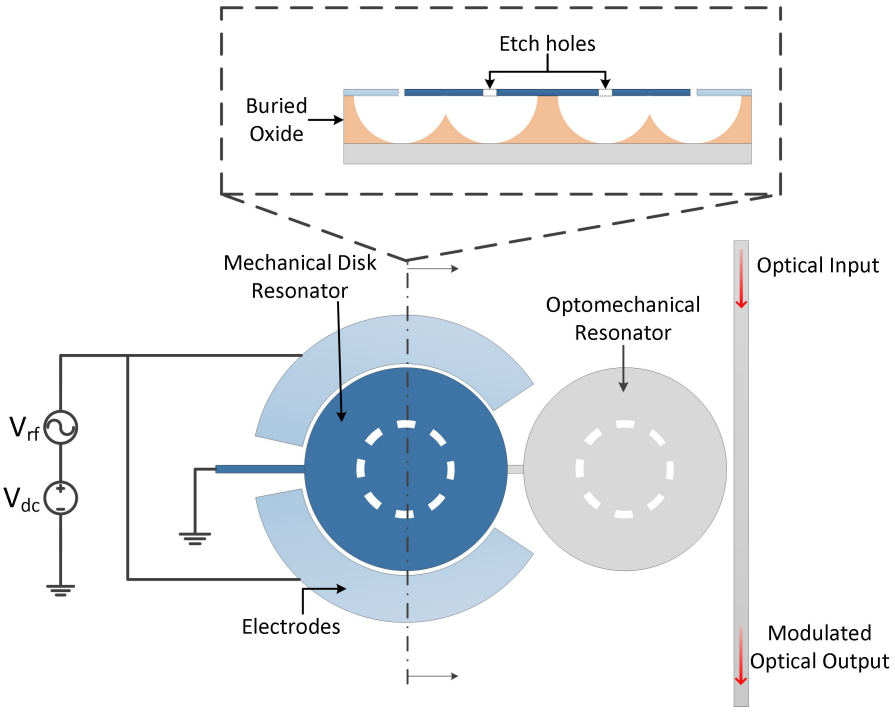

Figure 4.2: Schematic of the electrically actuated disk mechanical resonator in blue (on left) coupled to an optomechanical resonator in gray(on right). A combination of DC and RF potential applied to electrodes around the mechanical resonator excite vibrations which get coupled to the optomechanical disk resonator .These radial vibrations affect the optical resonance thereby modulating the intensity of light exiting the waveguide

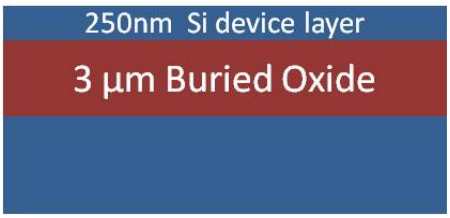

(a) Starting silicon on insulator substrate with 3μm buried oxide and 250nm silicon device layer

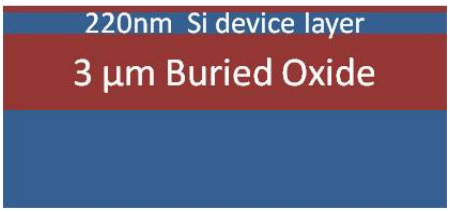

(b) Thermal oxidation to obtain 60nm oxide hard mask for silicon etch

(c) Electron beam lithography to transfer pattern into elecron beam resist

(d) Transfer pattern into oxide hard mask using CHF_3/O_2 etch

(e) Transfer pattern to silicon using Cl_2 ICP RIE

Figure 4.3: Process flow for silicon acousto optic modulator (contd.)

(g) Remove oxide hard mask using CHF_3/O_2 RIE etch

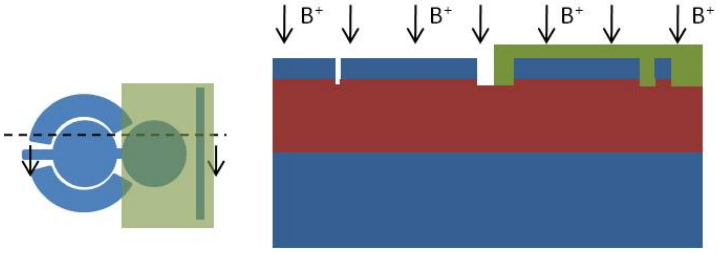

(h) Pattern photoresist and perform boron ion implantation to reduce resistivity of electrical routing beams and mechanical resonator

(i) Pattern release windows around the devices and protect the waveguides and grating couplers

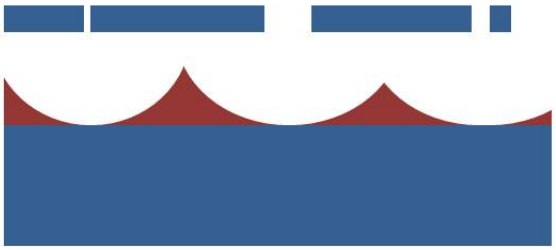

(j) Release using timed etch in buffered oxide etchant, remove photoresist in acetone and dry using critical point dryer to prevent stiction

Figure 4.3: Process flow for silicon acousto optic modulator

4.2 Fabrication

The modulator is fabricated using a three mask process on a custom SOI wafer (undoped 250 nm device layer for low optical loss and 3m thick buried oxide). The top silicon is thermally oxidized to obtain a thin oxide hard mask layer and a silicon device layer thickness of 220nm. Ma-N 2403 electron beam resist is spun on top of the oxide and patterned using electron beam lithography. The patterns are transferred into the oxide using a CHF_3/O_2 based reactive ion etcher . The electron beam resist is then removed by ashing in an oxygen plasma. The oxide hard mask pattern is then transferred into the silicon device layer using a chlorine based reactive ion etch to define the modulator, waveguides and bond-pads. A second layer of photoresist is spun and windows are patterned above the mechanical resonator and electrical routing beams. A boron ion implantation is carried out to reduce the resistivity of these structures. After photo resist removal, the samples are annealed at 900°C to activate the boron ions and remove ion implantation damage. The samples are then primed in HMDS vapor prime to make the surface hydrophobic and allow for good photoresist adhesion during the wet release etch. Photoresist is then spun again and a third mask is then used to pattern release windows near the modulator. This is followed by a timed release etch in buffered oxide etchant to undercut the devices. The photoresist is removed by an acetone dip and the samples are dried after the wet release etch using a critical point dryer to prevent stiction. Figure 4.4 shows a scanning electron microscope image of the acousto optic modulator. The radii of the disks are 10μm which gives a mechanical resonance frequency of 242MHz. The gap spacing between the actuation electrodes and the mechanical resonator is 150nm. The suspended waveguide which are 350nm wide are

anchored to the substrate using tethers. The coupling beam width is kept to a minimum in order to prevent large scattering losses of the optical mode from the coupling beam. In the device shown here the width of the beam is kept to 0.5μm and the length of the beam is 1.5μm. S-bend structures are used to reduce the optical loss at these anchor points [46]. The timed release etch is kept to the minimum time possible in order to prevent photoresist delamination which increases with the etch time. The disk resonators have etch holes in them to allow the oxide etchant to undercut the disks and to keep the undercut depth to 3μm. The etch holes are so designed to leave behind a 1μm oxide pedestal at the center supporting the disk. Grating couplers are designed to couple light into and out of the waveguides.

4.3 Characterization

4.3.1 Optical Characterization

The first step after fabrication is to characterize the optical resonator. Light from a tunable laser (Santec TSL 510) is coupled into a polarization maintaining (PM) fiber. This is then incident on a glass fiber holder in which the PM fiber is held in a glass plate using V-grooves. The glass plate is polished such that it forms a 8° angle at the face. This glass plate is then held at an angle of 8° over the substrate containing the waveguides. The 8° polish ensures that the face of the glass plate containing the polish fiber end is now flush in line with the substrate. The PM fibers are aligned such that the light coming out is polarized parallel to the substrate. The grating coupler picks this light up and couples it into the

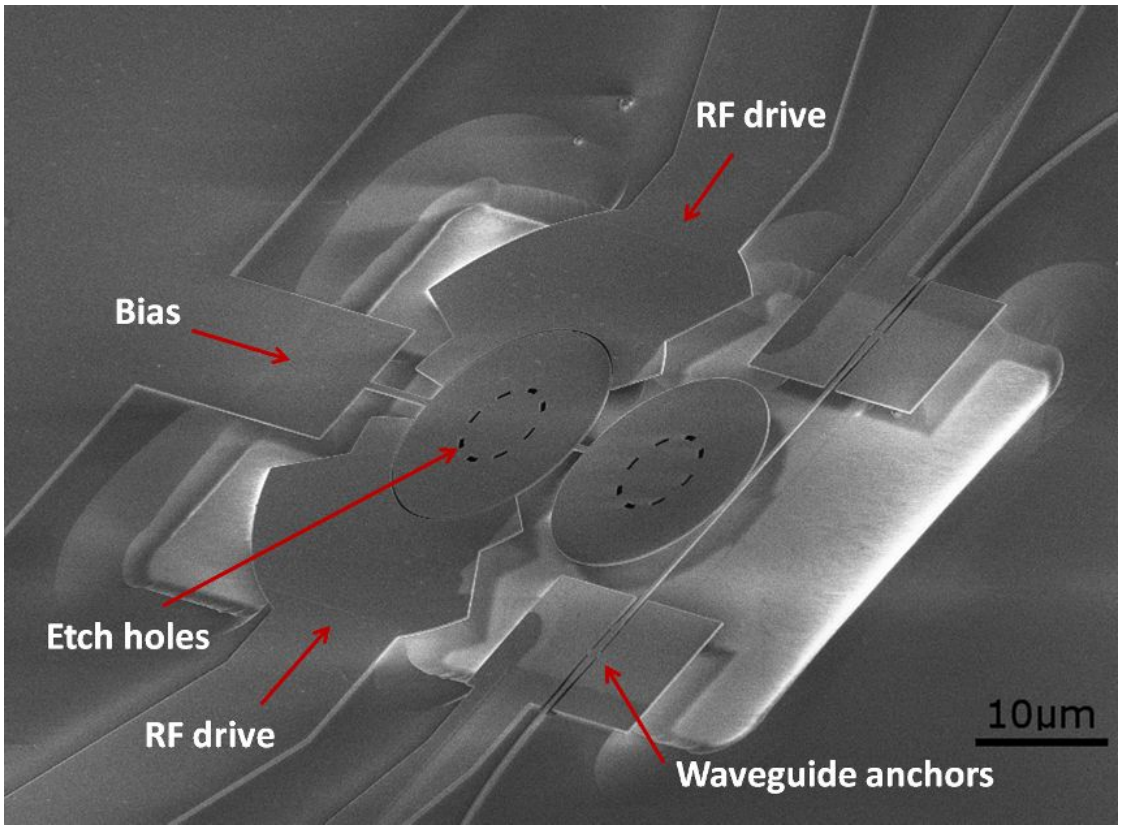

Figure 4.4: Scanning electron microscope image of fabricated device showing the coupled disk resonator geometry. The darker silicon shade show the silicon regions where boron has been ion implanted while the lighter silicon regions are undoped silicon.

silicon waveguides. At the output, the light from the grating is picked up using another fiber in the glass plate. This output is then sent to a photo detector which is connected to an power detector. The output from the power detector is obtained in the form of an analog voltage which is sent to a controlling computer using an National Instruments (NI) digital acquisition card. The tunable laser is controlled using NI Labview software to sweep the laser, while the power meter output is collected at the computer to obtain the optical transmission spectrum. The optical transmission spectrum shows multiple dips corresponding to the

whispering gallery modes of the disk resonator. A typical optical transmission spectrum is shown in figure 4.5(a). The typical quality factors obtained for the released disk of 10μm radius with the coupling beam and etch holes is around 25,0000. Figure 4.5(b) shows an optical mode seen for these disks with a high optical quality factor of 53,000.

To analyze the mode family that is coupling to the waveguide, a simulation was performed to solve the Maxwell's equations with appropriate boundary conditions[47].In addition to the condition for critical coupling, optimum coupling is expected when there phase matching between the waveguide mode and the resonator mode [29]. Figure 4.10(a) shows the waveguide mode for 350nm wide and 220nm thick silicon waveguides with air cladding obtained from COMSOL finite element software with an effective index of 1.818. Additionally, the mode family to which coupling is observed has a free spectral range of ≈12nm. Using these two parameters, the optical disk resonator mode that is expected to couple to the waveguide is shown in figure 4.10(b) . The optical mode is a higher order radial and azimuthal mode with a effective index of 1.791 which is close to the effective index of the waveguide. The mode also has a smaller field at the edge of the disk which may reduce the scattering seen from the coupling beams and explain the high quality factors seen for these modes. Figure 4.7 shows the optical resonance measured for three different disk resonators on a unreleased substrate. For the optical mode observed around 1548nm, the optical quality factor is approximately the same for the disk resonator, disk resonator with etch holes and disk resonator with etch holes and anchors. This suggests that the optical mode interacts only weakly with the changes made to the disk resonator.

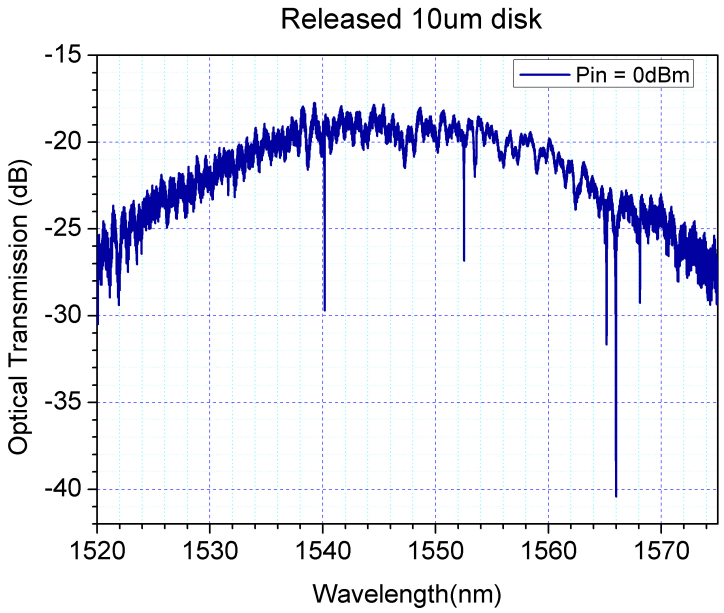

(a) Optical transmission spectrum showing multiple resonances. The grating response is seen as the envelope with an insertion loss of 21dB from input to output.

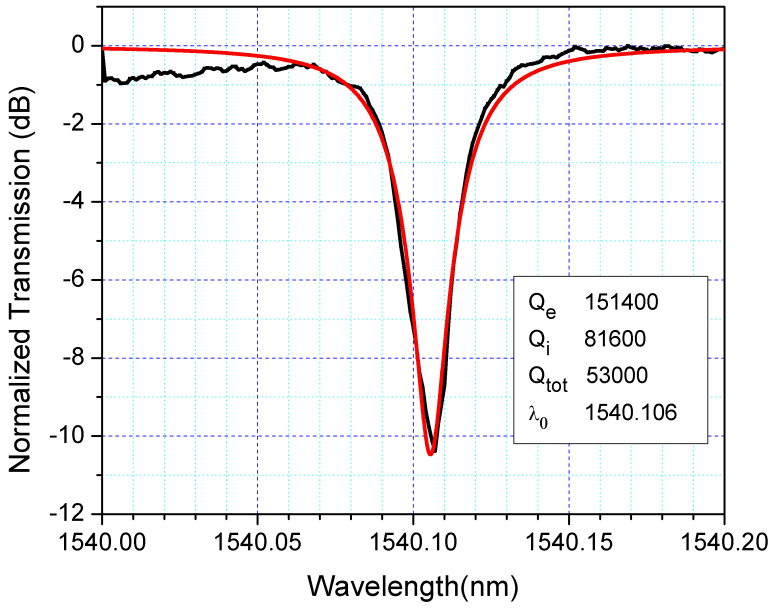

(b) Close up of the resonance at 1540.1nm showing an optical quality factor of 53,000

Figure 4.5: Optical transmission characteristics of released optomechanical resonators

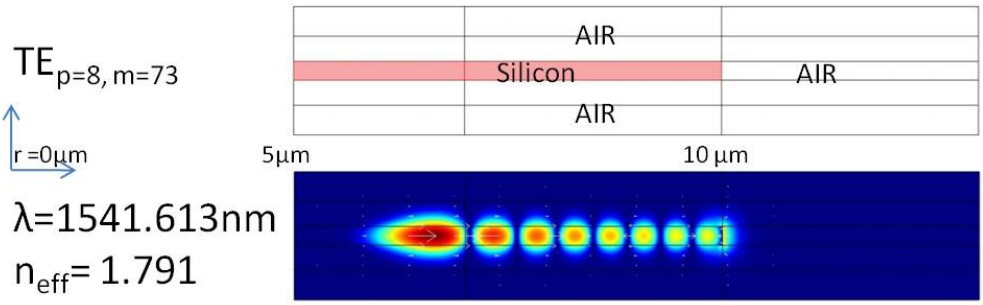

(a) Optical mode shape of the disk showing log of radial electric field intensity for mode with radial number 8 and azimuthal number 73 with an effective index of 1.791

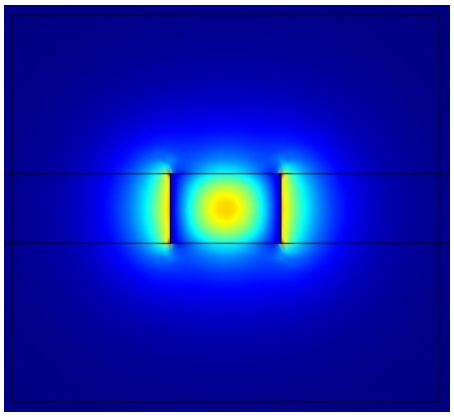

(b) Electric Field intensity profile for the horizontal component for a air clad 350nm wide suspended silicon waveguide with n_{eff} = 1.818

Figure 4.6: Optical mode shape of disk resonator and waveguide

4.3.2 Electro Optic Characterization

After the optical transmission spectrum is measured, the laser wavelength is fixed at the half maximum point of a particular optical resonance. A setup as shown in figure 4.8 is used to measure the electro optic response. The electrodes and the resonator structures are connected to large silicon pads (80μm x 80μm) on which GSGSG probes can be landed. SMA cables are used to carry the RF signals from port 1 of an Agilent N5230A network analyzer to the probes. A DC bias is applied along with the RF signal in order to obtain a force at the

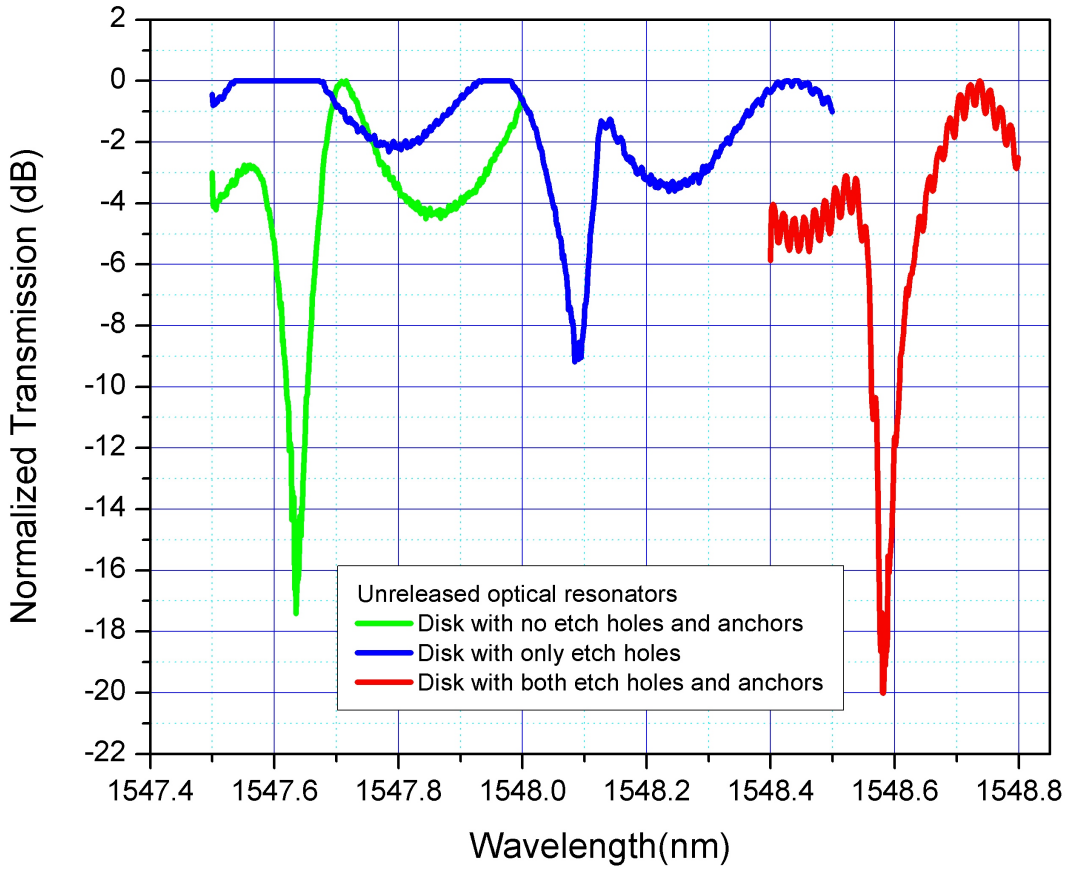

Figure 4.7: Optical resonance around 1548nm for three different disk structures (green)disk with no holes and anchors (blue)disk with only etch holes (red)disk with etch holes and anchors

frequency of the RF input as explained earlier. The output from the grating is sent to a high speed 1647 New Focus avalanche photo diode which has a gain of 4500V/W. The RF output from the photo diode is sent to port 2 of the network analyzer. The network analyzer applies a RF signal to port 1 at a particular frequency and records the power measured at port 2 with a preset bandwidth around the excitation frequency. The response of the device is measured as the transmission S21 which is the ratio of power received at port 2 to the power output from port 1. The typical transmission for the Acousto Optic modulator

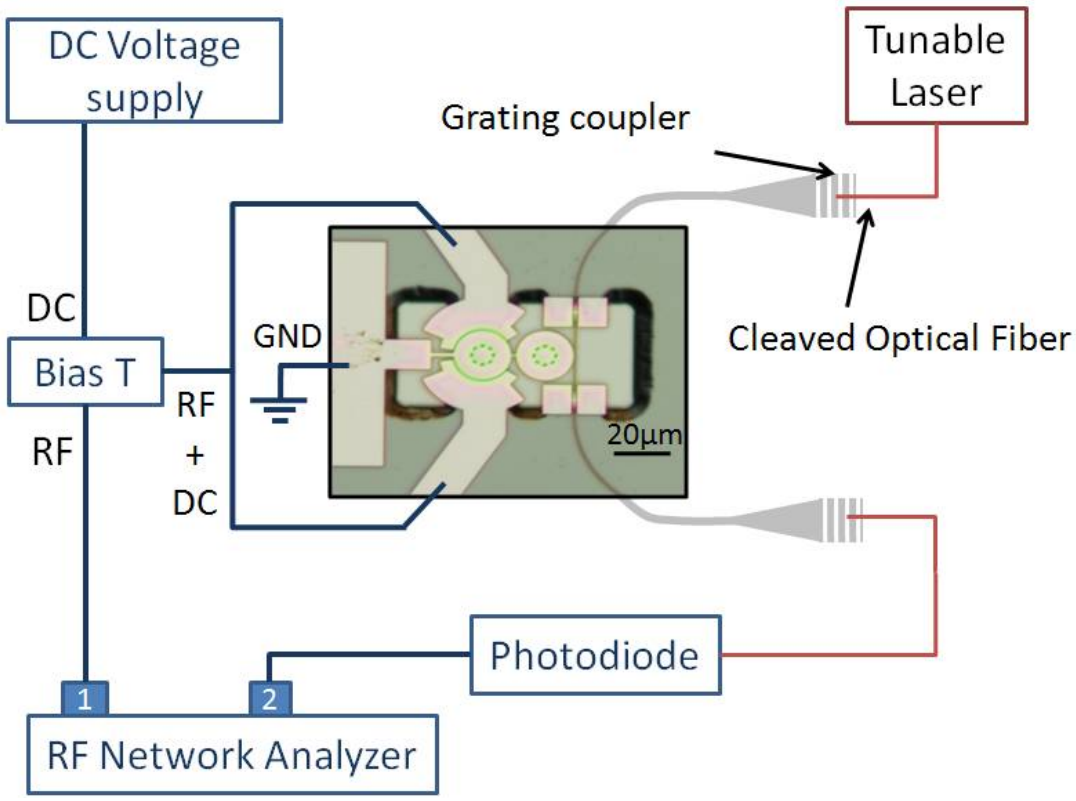

Figure 4.8: Setup for measuring the electro optic response of the Acousto Optic modulator.RF signal from port 1 is applied to device along with DC bias using GSGSG probes. The optical response at the excitation frequency is observed at port 2 of the network analyzer.

is shown in figure 4.9 .When the electrical input is at a mechanical resonant frequency of 235.1MHz, there is a peak in the transmission which corresponds to an optical modulation. To confirm that the optical modulation is indeed due to the electrostatic actuation, the DC bias applied to the device is varied. The DC bias determines the amount of force at the RF frequency as given by equation (2.8). On increasing the DC bias, the force is larger which leads to larger motion of the disk resonators. This larger motion is able to achieve deeper modulation of the optical power which shows up as an increased transmission at the

mechanical resonant frequency. The radial vibrational mode of the disk splits into two modes which are seen as two peaks in the transmission response at 235.1MHz and 242MHz.The predicted mechanical frequencies from finite element simulation and the corresponding measured values are in good agreement with each other. Figure 4.10 shows the simulated COMSOL mode shapes of the two radial modes. The mode at 235.1MHz has a mechanical quality factor of 1,300 in air. The power received at the detector has been used to back calcu-

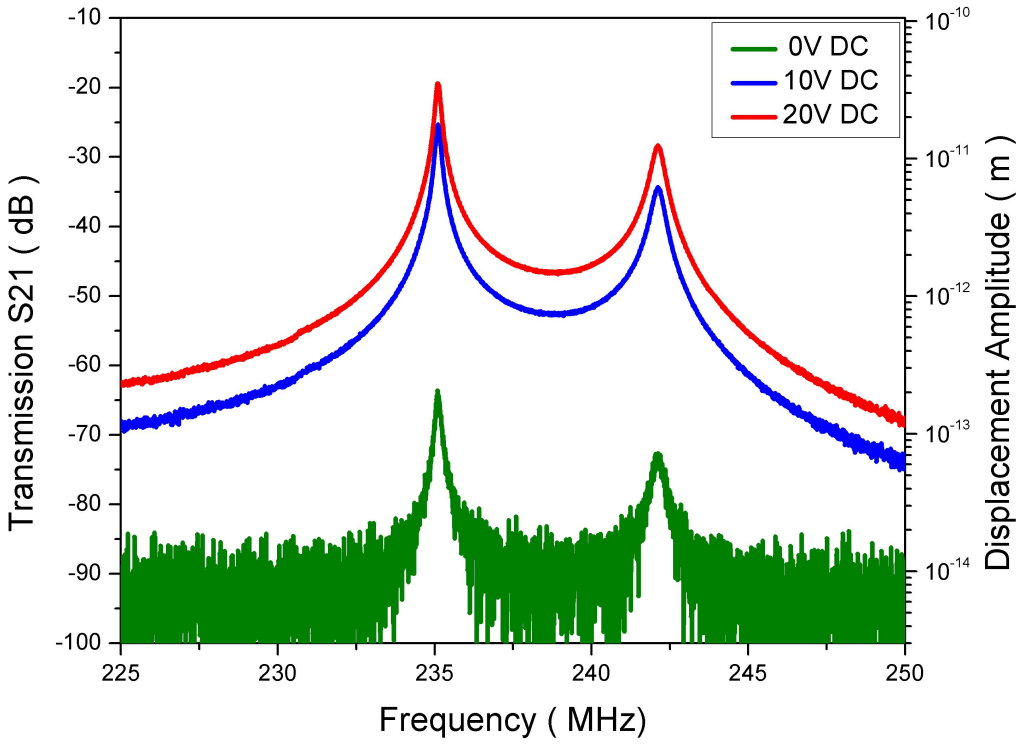

Figure 4.9: Electrical transmission spectrum observed using the network analyzer showing modulation peaks at 235.1 MHz and 242.1MHz when input RF power is at -10dBm and optical input power is at 6dBm

late the modulation on the average power at the detector. The displacement

required to obtain the modulation is calculated using the modeling scheme for optomechanical resonators presented earlier. This information of the expected displacement is plotted on the right side y axis of figure 4.9 to give an idea of the displacement of the mechanical resonator.

Table 4.1: Optical and Mechanical Parameters corresponding to the Acousto Optic Modulator measurement in figure 4.9

(a) Optical Resonator Parameters

Resonance Wavelength	1550.541nm
Quality Factor	26,140
Insertion Loss (from input to output)	21dB
Laser Input Power	6dBm

(b) Mechanical Resonator Parameters

Resonance Frequency	235.1MHz/ 242.6MHz
Quality Factor (in air at 235.1MHz)	1300
RF input power	-10dBm
RF Insertion loss(at resonance and 20V DC)	-19dBm

4.3.3 Modulator : Figure of merit

While the transmission characteristics measured on the network analyzer is a good measure of the modulated RF power at the output, it is also strongly influenced by the optical power at the detector. The insertion loss in the RF transmission measurement is not just a function of the optomechanical performance of the device but also the optical losses in the coupling and waveguiding structures on the optical structures. This is seen in figure 4.11 which shows two transmission measurements for the same input RF power applied to the device but with

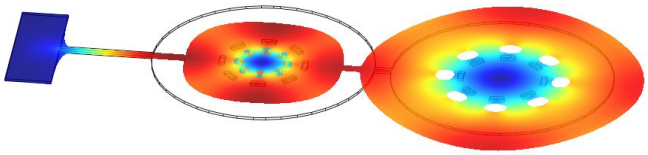

(a) Mode Shape for the out of phase mode with a simulated resonance frequency of 241.6MHz and measured frequency of 235.1MHz

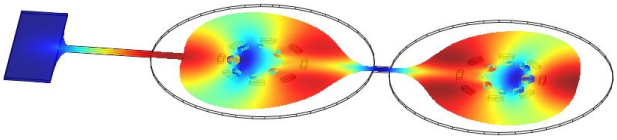

(b) Mode Shape for the in phase mode with a simulated resonance frequency of 248.3MHz and measured frequency of 242.1MHz

Figure 4.10: Displacement mode shapes of the radial vibrational modes of the coupled disk acousto optic modulator obtained using COMSOL finite element simulation

different optical powers input to the modulator device which corresponds to different average optical power at the detector. To characterize the modulator independent of the optical power incident at the detector, a parameter called the modulation index is introduced. As the detector modulates the optical intensity at the frequency of input, the optical power at the detector is then

$$i_{det} = \Re \alpha P_{in}(1 + m\cos(\omega t)) \tag{4.1}$$

where $\Re$ is the responsivity of the detector in A/W, P_{in} is the average optical power input to the modulator, α is the optical loss from input to output. The average optical power is modulated by the second term which is a cosine multiplied by a modulation index m. The value of m can range from 0 which corresponds to no modulation to 1 which corresponds to complete modulation. The power at the output of the detector terminated by a resistor R_o at the frequency

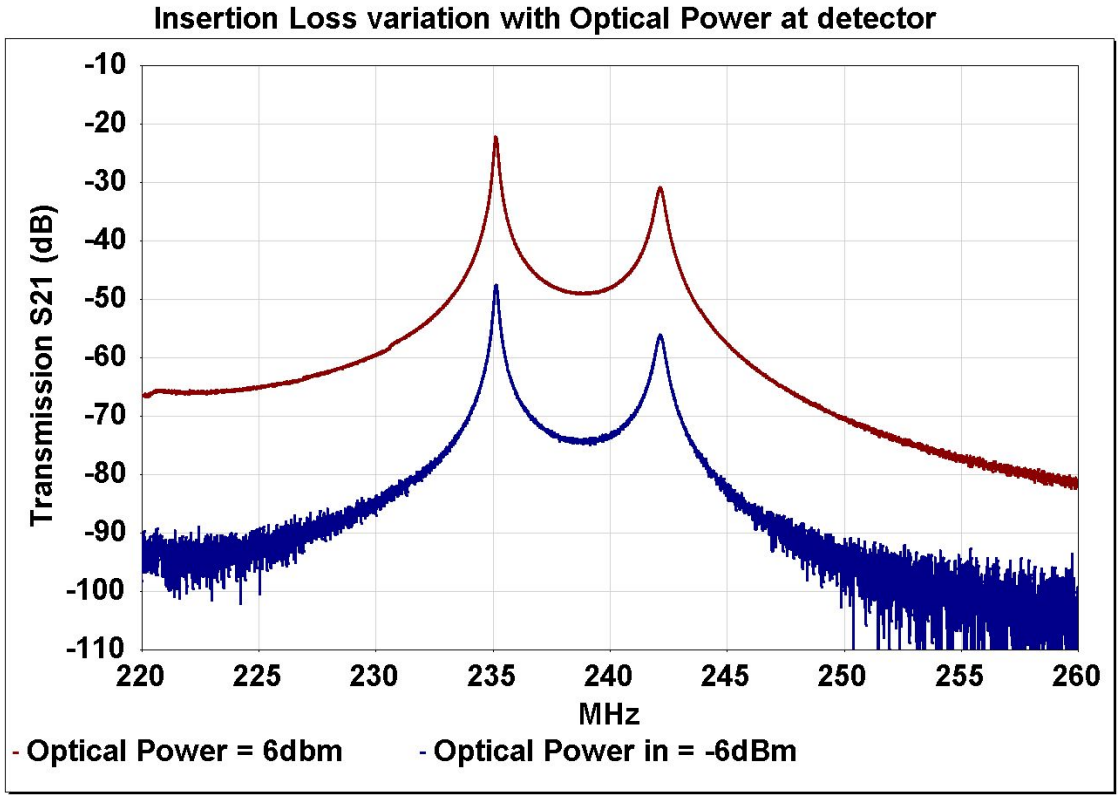

Figure 4.11: Transmission spectrum measured for the acousto optic modulator at input RF power of 0dBm and DC bias of 15V for two different optical input powers of 6dBm(red) and -6dBm(blue)

ω of the input is then

$$P_{det} = \frac{1}{2} m^2 R_o \Re^2 P_{avg}^2 \tag{4.2}$$

where the average power at the detector is $P_{avg} = \alpha P_{in}$. From this equation it is observed that the power incident at the network analyzer for the same modulation level can be different depending on the input power level and optical losses in the system. Henceforth, the characterization of the modulator presented here will make use of the extinction ratio and modulation index as defined above.

The extinction ratio and the modulation depth can be obtained by observing the modulated waveform. This is done by taking the power out from a DC

coupled photodetector to an oscilloscope. The voltage measured on the oscilloscope is then given by $V_{osc} = R_o \Re P_{avg}(1 + m\cos(\omega t))$. Figure 4.12 shows the measured waveform for an input RF power of 10dBm at the mechanical resonant frequency of the modulator of 236.8MHz. The extinction ratio is defined as the ratio of the maximum modulated power to the minimum optical power which is equivalently defined as

$$ER = 10log\left(\frac{V_{max}}{V_{min}}\right) \tag{4.3}$$

The modulation index which is given by the ratio of the maximum optical power to the mean optical power can be obtained by

$$m = \frac{ER - 1}{ER + 1} \tag{4.4}$$

As seen from the waveforms in figure 4.12, an increasing DC bias leads to a larger modulation. This is because the electrostatic force depends on the DC bias applied and a larger DC bias corresponds to a larger displacement and thereby greater modulation.

4.3.4 Modulator performance on varying input parameters

The performance of the modulator is characterized by observing the modulation index and the extinction ratio to the electrical input parameters which are the DC potential bias and the RF signal power . Figure **??** shows the variation of modulation index with respect to the DC bias applied to the device for two different RF powers from both simulations and measurements. The RF signal is applied at the mechanical resonant frequency in order to obtain the maximum

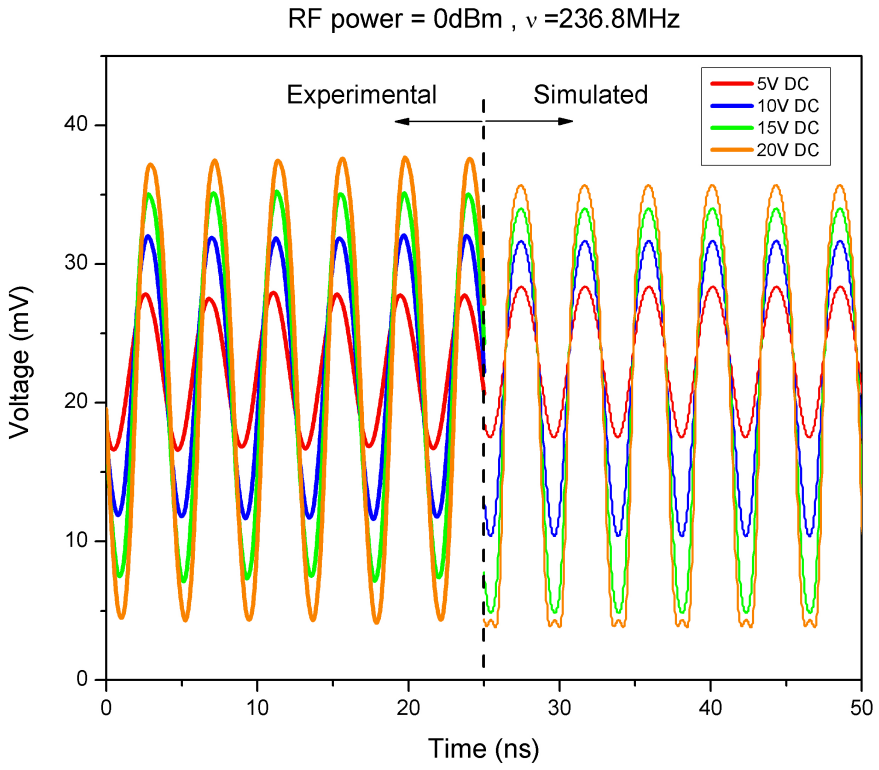

Figure 4.12: Measured modulation waveform for RF power of 0dBm at the reosnance frequency of 236.8MHz for different DC bias values. On the right side is the expected modulation waveform from simulations

modulation. The force on the mechanical resonator and thereby the displacement increases linearly with the DC bias. This is seen as a increase in the modulation index and extinction ratio with increasing DC bias. At higher displacements, when the shift in resonance is more than the resonance wavelength we see the modulation index saturating. The optical resonance used for this modulator has an optical resonance with a quality factor of 53000 and an extinction of 10db as seen in figure 4.5(b). The simulations predict the modulation index to saturate around 0.8 and is observed at 0.88 in experiments. A similar effect

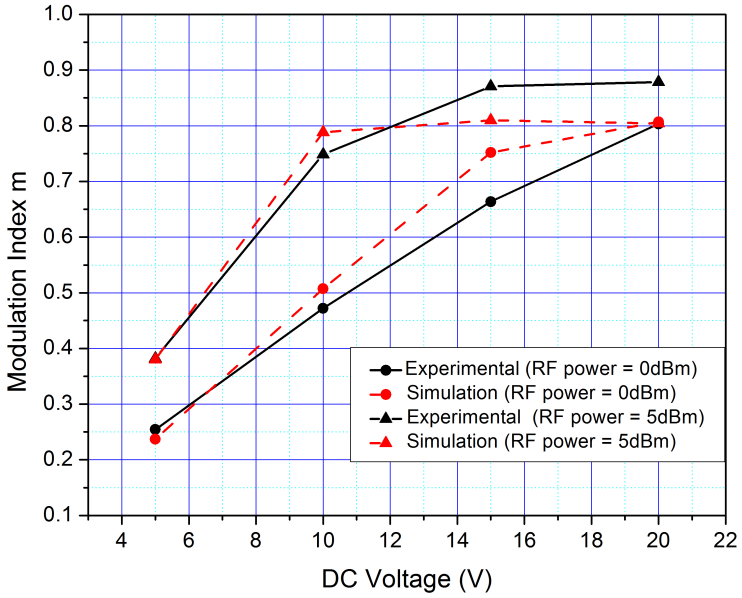

Figure 4.13: Measured (black) and simulated (red) modulation index with varying DC bias voltage for RF powers of 0dBm and 5dBm

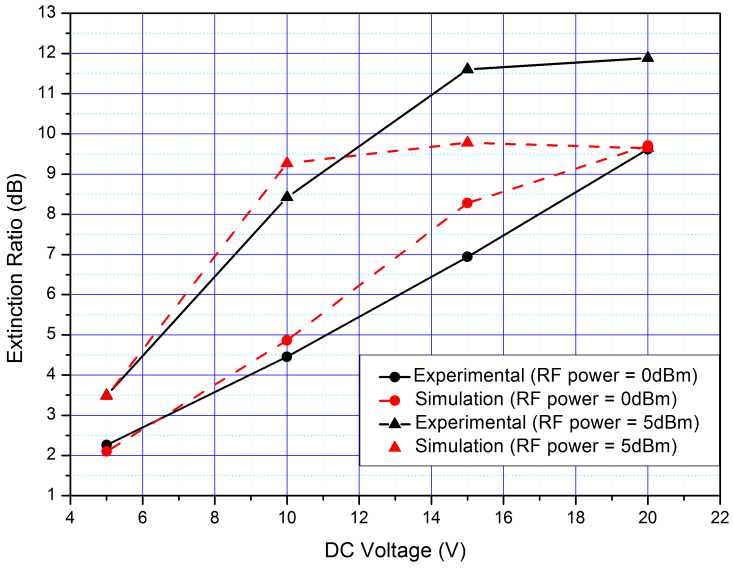

Figure 4.14: Measured (black) and simulated (red) extinction with varying DC bias voltage for RF powers of 0dBm and 5dBm

is seen in the extinction ratio with increasing DC bias voltages in figure 4.14 . The extinction ratio in the simulations is expected to saturate at 10dB which is the extinction obtained from the optical resonance. The experiments show saturation of the extinction ratio at a slightly higher value of 12dB.

A similar experiment is carried out to study the variation of the parameters with input RF power while holding constant DC bias potential and the results are shown in figure 4.15. A non linear dependence of the modulation index and extinction ratio is observed with RF power. This is due to the fact that the ac potential on the actuation capacitor is not linear with the input RF power as explained in more detail in appendix A.

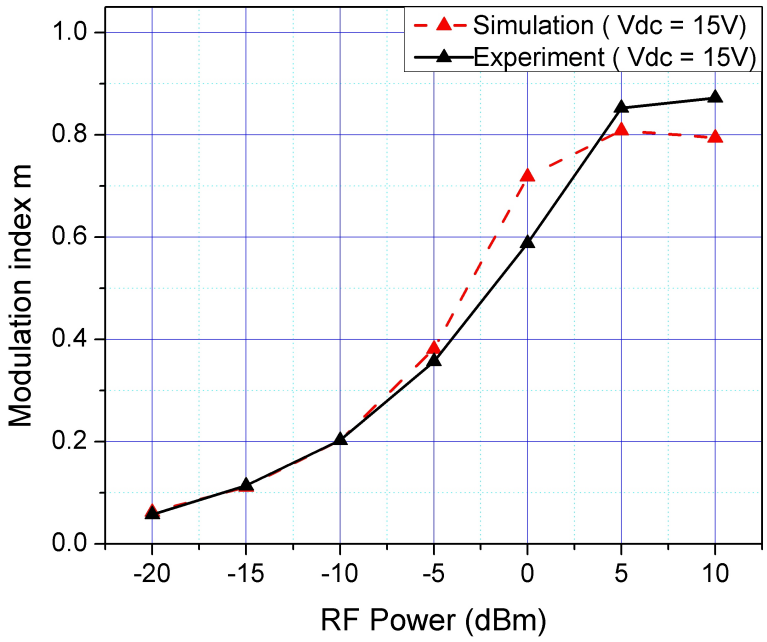

Figure 4.15: Measured (black) and simulated (red) extinction with varying RF power for a DC bias of 15V

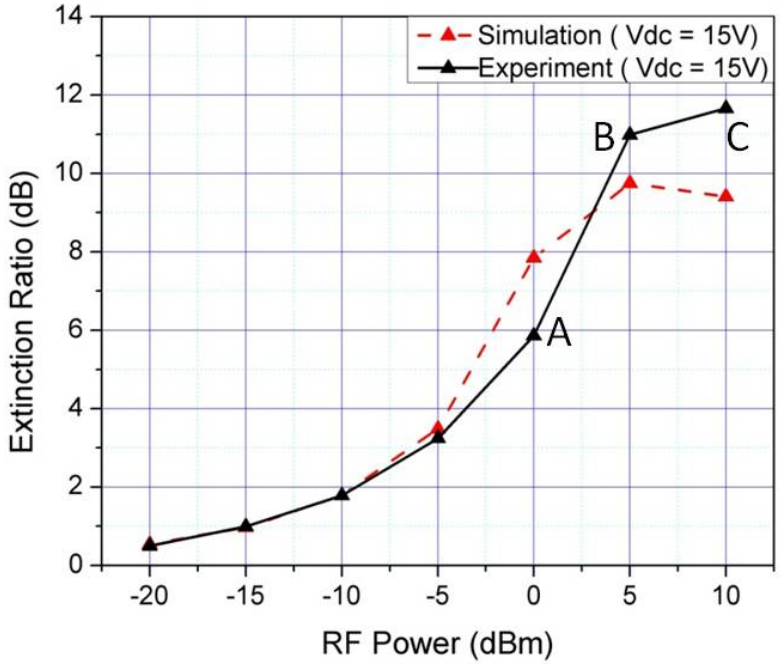

Figure 4.16: Measured (black) and simulated (red) extinction with varying RF power for a DC bias of 15V

4.3.5 Saturation of modulator response

As explained in the previous subsection, there is a saturation of the modulator performance parameters at high RF powers. This occurs when the RF signal frequency is at the mechanical resonant resonator frequency. Figure 4.17 shows how the saturation effect is observed in the transmission measurements where the frequency of the RF signal is swept. In the normal mode of modulator operation, a higher RF input would corresponds to a higher modulation and thereby higher power at the output. The ratio stays a constant and the transmission spectrum remains constant for varying RF powers below saturation. However, when saturation occurs, a response as seen in figure 4.17 is observed. As the RF power approaches the mechanical resonant frequency, the modulated power cannot increase any more. The saturation of the output power is seen as an in-

crease in insertion loss at the resonant frequency and also as a decrease in the quality factor. In figure 4.17 the quality factor is seen to fall from 1116 at 0dBm RF input to 650 at 10dBm RF input.

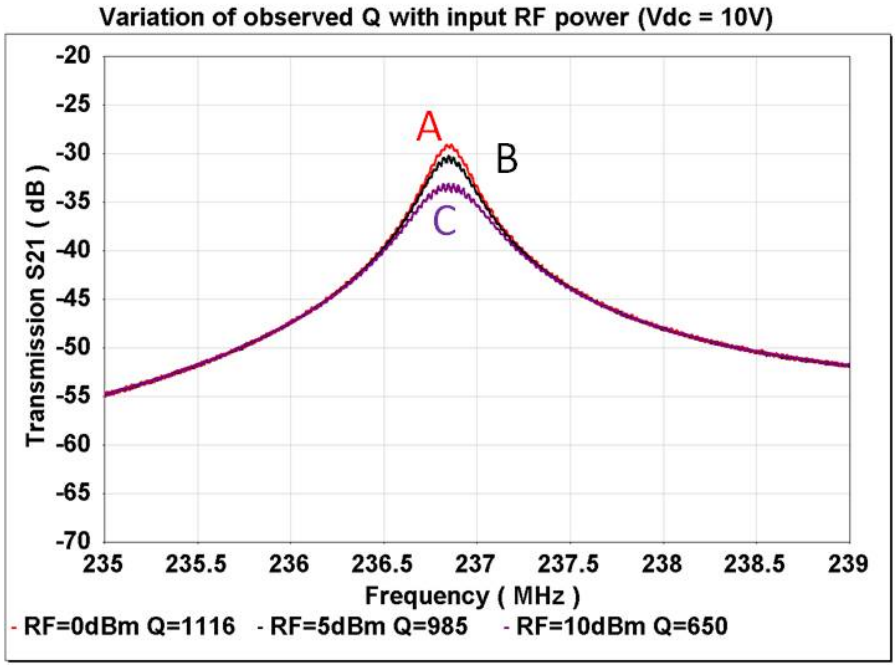

Figure 4.17: Transmission spectrum observed on the network analyzer for varying RF powers from 0dBm to 10dBm at a DC bias voltage of 10V. The labels A, B and C refer to the received power saturating corresponding to the labels in figure 4.16

It is interesting to observe the modulation waveform when the modulation is saturated. Figure 4.18 shows the experimentally measured waveform and simulated waveform at saturation. At these displacement amplitudes, the resonance wavelength shifts beyond the input wavelength and the output goes back up on to the other side of the resonance. This is seen as a small bump at the bottom of the sinusoid. Saturation also transfers power from the fundamental excitation frequency into higher harmonics in the modulated output. If the input were biased at the optical resonance frequency and the resonator is electrically excited

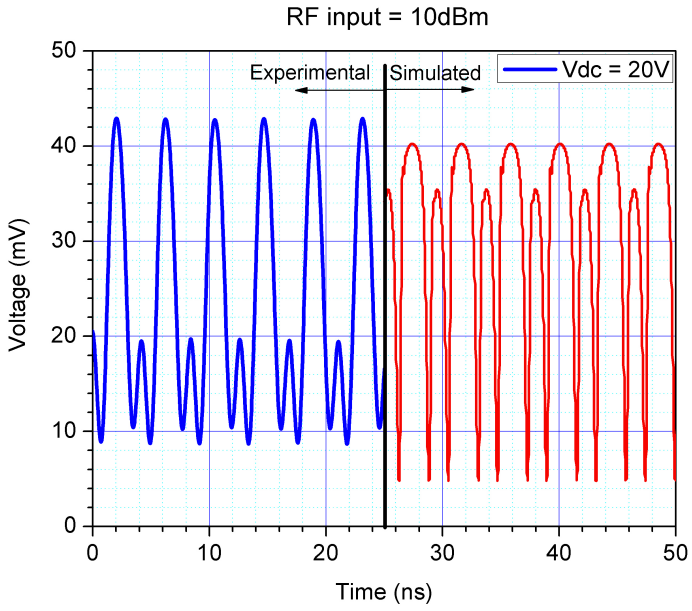

Figure 4.18: Measured (blue) and Simulated (red) waveform when the modulator output is saturated

at the mechanical resonance frequency, it is possible to obtain optical modulation which is at twice the frequency of the input excitation. This is due to the fact that any movement of the disk would cause the resonance to shift in such a way to cause an increase in the transmission. As this happens for both increasing and decreasing radial displacement, this leads to frequency doubling at twice the output of the mechanical frequency. To study the nonlinearity in the frequency domain of the modulator an additional experiment was performed. The output power from the photodiode is observed on a RF spectrum analyzer while the input is driven by a single frequency RF source set at the mechanical resonance frequency of 236.8MHz. The response for varying RF powers is represented by the different colors in the spectrum in figure 4.19. As the RF power is increased, a larger increase is observed in the output power at the third and

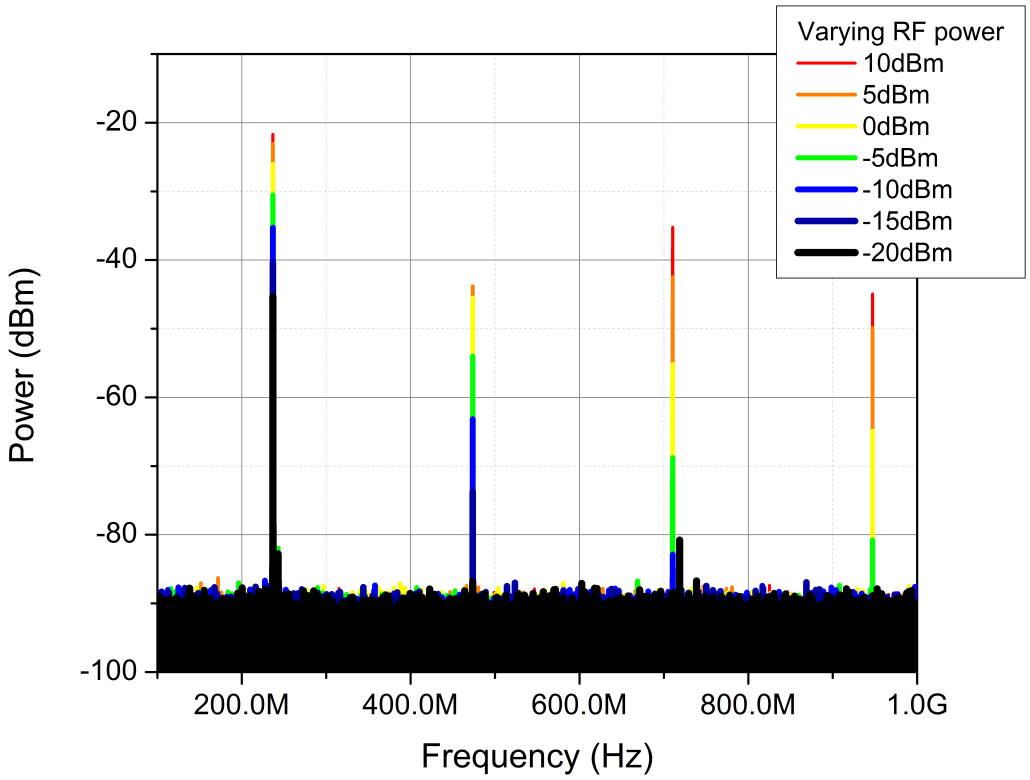

Figure 4.19: Output from the photodiode observed on a spectrum analyzer with input to the modulator driven by a single frequency RF source. The RF source is set to the mechanical resonance frequency of 236.8MHz with a DC bias of 15V and optical input of 5dBm while the RF power is varied

higher harmonics as the modulator gets saturated.

4.3.6 Mechanical Mode Spectrum

The analysis presented so far involved exciting the radial mode of the modulator. The transmission spectrum of the modulator however shows that there

any many other modes that can be sensed in addition to the radial modes. Figure 4.20 shows the transmission spectrum of the acousto optic modulator over a wider frequency range. The mode shapes and frequencies that are expected fort the mechanical modes are obtained through a finite element model in COMSOL. These frequencies agree well with the measured values as shown in figure 4.20. The insertion loss obtained in the transmission spectrum for a particular mode is a function of both the strength with which it is excited and the strength with which it is sensed optically. The displacement amplitude of a mode is dependent of the geometry of the excitation electrode and its overlap with the mechanical mode to be excited. The optical sensing on the other hand depends on optomechanical coupling constant for that particular mode. The radial displacement is seen to have the highest response in the modulator. This is due to the fact that electrodes around the disk excite the radial modes most efficiently. The optomechanical coupling which is dependent on the optical path length change is also largest for the radial mode. In addition to the radial mode, we see the presence of the first order wineglass modes around 190MHz, torsional modes around 200MHz and the second order wineglass modes around 270MHz.

4.3.7 Mechanical Quality Factor limitation

The quality factors of mechanical resonators fabricated on single crystal silicon is limited by the acoustic losses in the material. The f-Q product of silicon at the frequency of operation of the acousto-optic modulator is around $2x10^{13}$ [48] , which gives a quality factor limit of around 85,000 due to material losses. Demonstrations of actual resonators on silicon have shown quality factors of 18,000 for resonances at 3.72GHz [49] which is very close to the material limit of

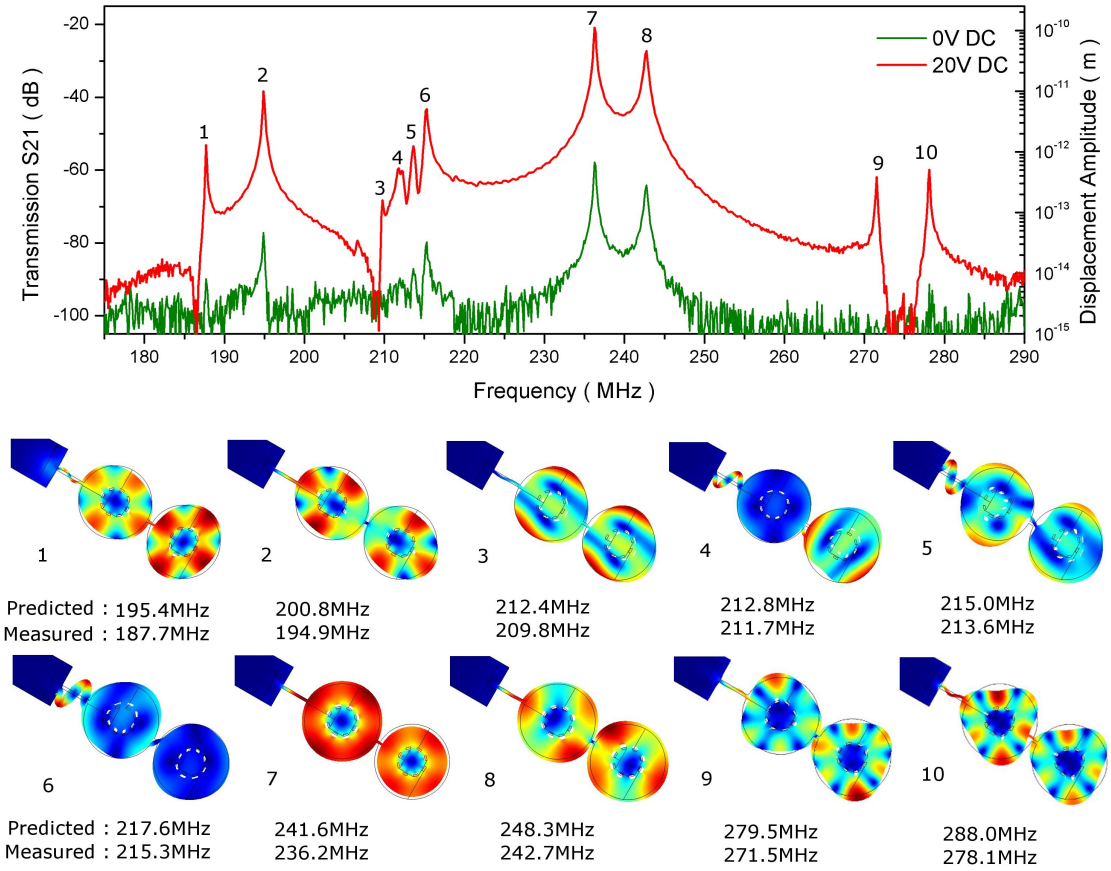

Figure 4.20: Transmission spectrum showing modulation at multiple in-plane mechanical resonances for an optical input of 6dBm and a RF input of 0dBm. Insets 1 to 10 show the mechanical mode shape obtained using finite element method and their predicted and measured frequency for modes in the transmission spectrum.

silicon. However, the resonators on the acousto optic modulator demonstrate quality factors of 1500 at 236MHz, which gives an f-Q product of only $3.5x10^{11}$. To investigate the losses limiting the quality factor of the mechanical resonator, a finite element simulation was setup to investigate the anchor losses in the acoustic optic modulator as outlined in [50]. The energy transfered into the sub-

strate through the anchors is simulated as being lost using a matched layer. The anchor loss limited quality factor obtained from this simulation as shown in figure 4.21 is 800 for the out of phase radial mode and 600 for the in phase radial mode which are very close to the quality factor of 1000 that is measured for these modes. The reason for the low quality factor is the presence of an anchor beam at the maximum displacement point of the disk to electrically ground the body of the resonator. The quality factor can be improved by moving the anchor over to the coupling beam and using the coupling beam to electrically ground the devices [51]. The coupling beam is now made a half wavelength such that there is a nodal point for the in-phase mode at the center of the beam where the electrical anchor can be created. Figure 4.21 shows the new proposed scheme for anchoring along with the anchor limited quality factor numbers for the two modes in the new scheme. From simulations, it is seen that the in-phase mode should not be limited by the anchor losses.

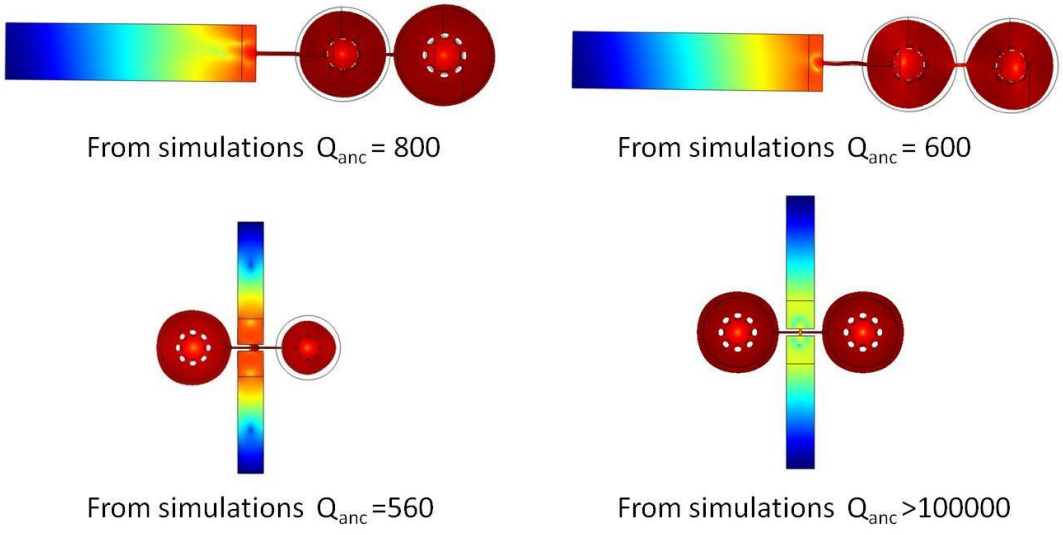

Figure 4.21: Simulations using matched layer to obtain the anchor loss limited quality factors of different configurations of the acousto optic modulator

4.4 Scaling to higher frequencies

4.4.1 Disk Resonators

In the previous sections, an acousto optic modulator working at a frequency of 236MHz was presented. A couple of approaches are available in order to scale the mechanical resonance to higher frequencies. The first approach is to scale down the radius which increases the fundamental resonance frequency of the disk. In order to obtain resonance above a GHz in silicon, the radius of the disk needs to be scaled down to below 3.5μm. Figure 4.22 shows an SEM image of a 3.8μm radius disk resonator based modulator which failed during fabrication. The anchoring scheme used here is a half wavelength coupling beam with anchor at the nodal point of the coupling beam. One of the important factor that needs to be considered is the optical quality factor of the optomechanical resonator which can be adversely affected by a decrease in the radius. A decrease in the radius makes the optical path length around the resonator comparable to the wavelength and increases the radiative bending losses. Figure 4.23 shows the optical resonance obtained for one of these devices. The optical resonance has a quality factor of 5,500 and an extinction ratio of 11.5dB. The optical input is then biased at the half maximum point of the resonance and the electro optic response is measured on the network analyzer. Figure 4.24 shows a wide spectrum from a few MHz all the way up to 2GHz. The transmission spectrum shows a resonance peak at 706.6MHz which corresponds to the fundamental radial mode of 3.8μm disk whose mode shape from finite element simulation is shown in figure 4.25(a). Another small peak is also observed at 1.928GHz which corresponds to the second order radial mode as shown by the mode shape in

figure 4.25(b). The mechanical quality factor of the fundamental mode is 2,600 as observed in the electro optic response shown in figure 4.26. While the fundamental resonance can be observed, the insertion loss in the electro optic response at the fundamental resonance is about 60dB which is very large. This can be attributed to a couple of factors. The first is the low optical quality factor of 5,500 of the smaller radius optomechanical disk resonators which makes the displacement sensing less efficient and the second is the reduced area of the actuation capacitor due to the decreased radius. The reduced area of actuation leads to a smaller electrostatic force and smaller displacements.

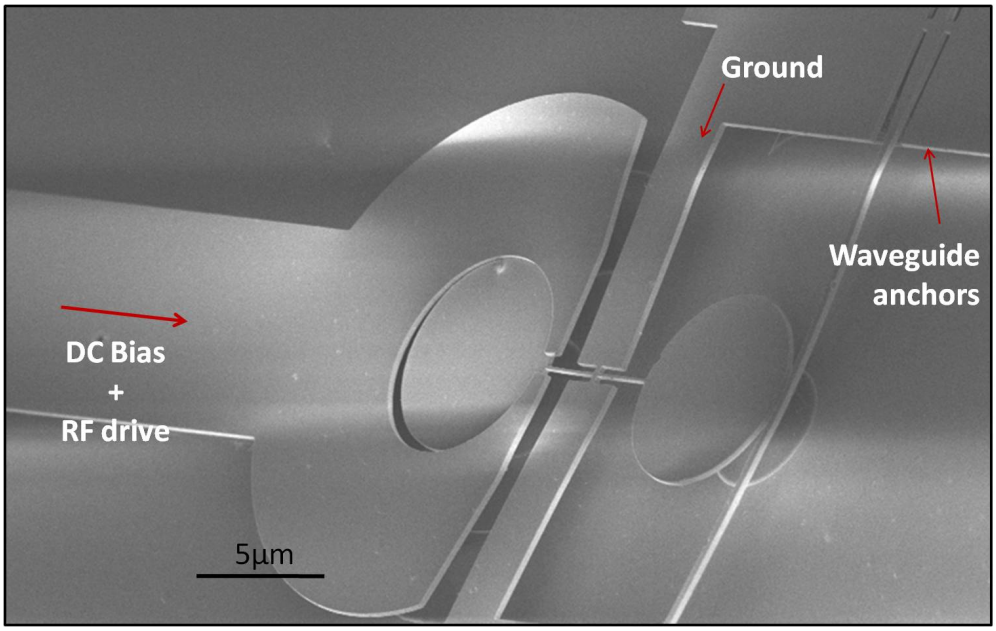

Figure 4.22: Scanning Electron Microscope Image of a 3.8μm radius disk based acousto optic modulator.

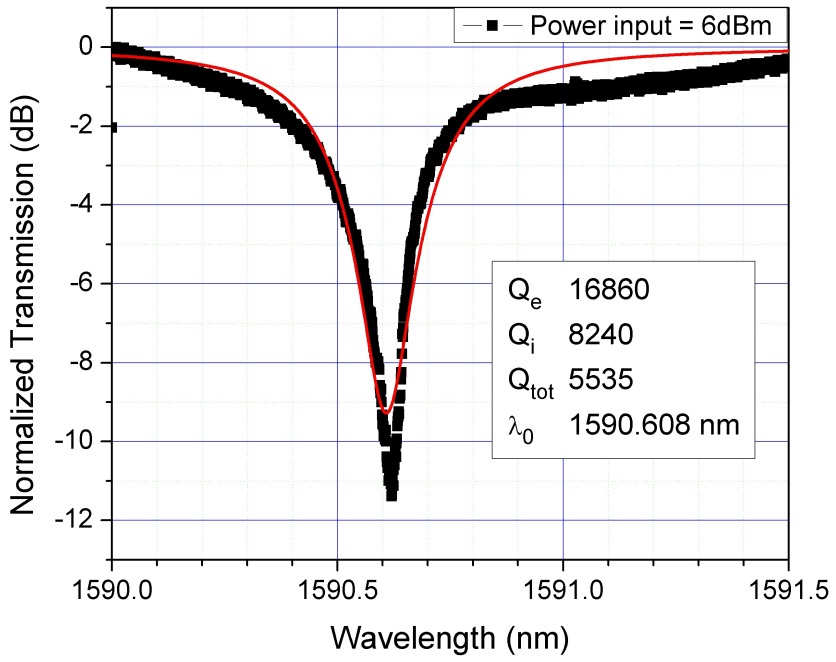

Figure 4.23: Optical resonance for the 3.8μm radius optomechanical disk

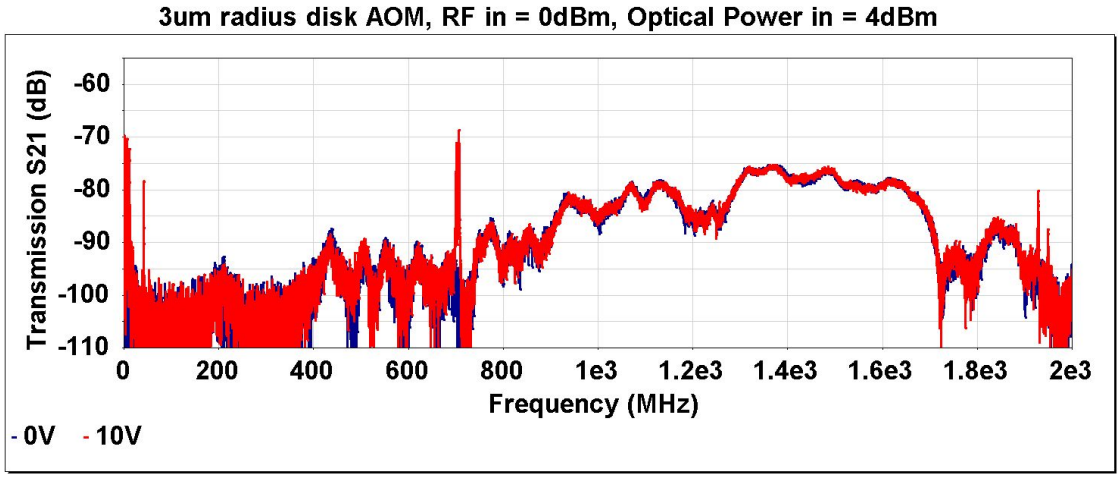

Figure 4.24: Electro optic response of 3.8μm radius disk based acousto optic modulator

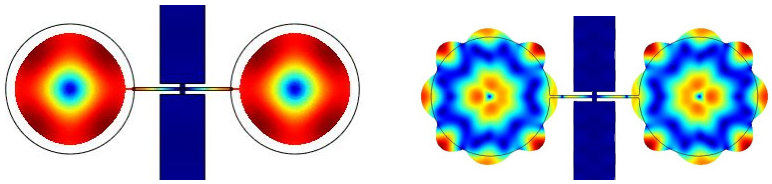

(a) Fundamental radial mode with simulated frequency at 705.6 MHz (b) Second order radial mode at 1950MHz

Figure 4.25: Simulated mode shapes in COMSOL for 3.8μm radius disk based acousto optic modulator

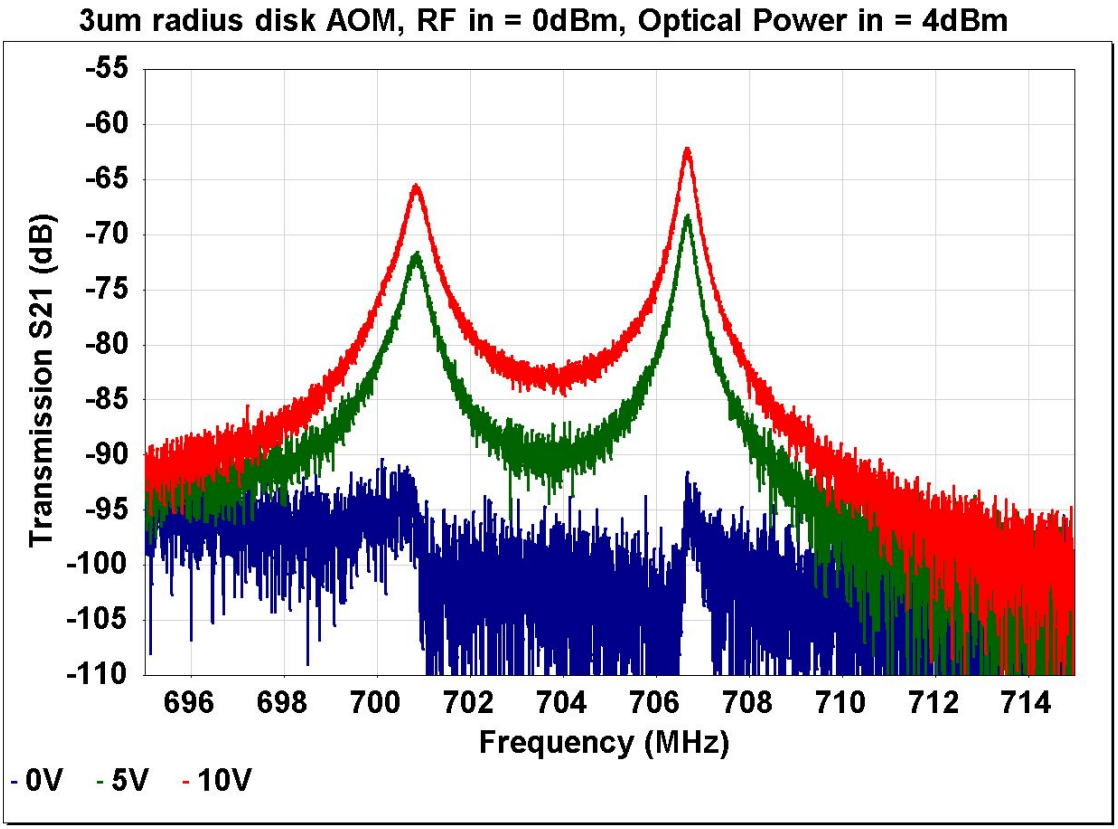

Figure 4.26: Electro optic response around the fundamental mode showing the fundamental mode at 706.6MHZ with a mechanical quality factor of 2,600

4.4.2 Ring Resonators

The other approach that overcomes the drawbacks of using a scaled disk resonator is the ring resonator. The ring geometry allows the decoupling of the radius of the ring and the mechanical resonance frequency. The second order radial mode of the ring is nearly independent of the radius of the ring and is only dependent on the width of the ring. This enables us to design a resonator with higher mechanical resonance without reducing the radius and thus preventing a reduction in the optical quality factor and the actuation capacitor area. Figure 4.27 shows a SEM image of an ring resonator based acousto optic modulator. The rings have an inner radius of 5.7μm and a width of 3.8μm. The inner radius of 5.7μm is chosen as it corresponds to the quarter wavelength at the resonance frequency of 1GHz. The quarter wavelength anchor beam reduces the displacement at the anchor point to 0 at the resonant frequency and thereby prevents coupling of mechanical energy into the anchor. The coupling beam is 11.4μm and the electrical anchor is placed at the nodal point which is 5.7μm away from the edge of the rings. The remaining features are similar to the lower frequency acousto optic modulator. The anchors are designed to provide the same electrical potential to the waveguides as the rings to prevent any unwanted motion of the waveguide towards the ring. Any potential difference would cause an electrostatic force on the waveguide which would move it inwards and change the optical coupling to the resonator.

The first step after fabrication is optical characterization. Figure 4.28 shows the optical transmission of an optical resonance observed for the ring optomechanical resonator. The response exhibits a split optical resonance which seems to suggest coupling from the counter clockwise traveling wave mode to the

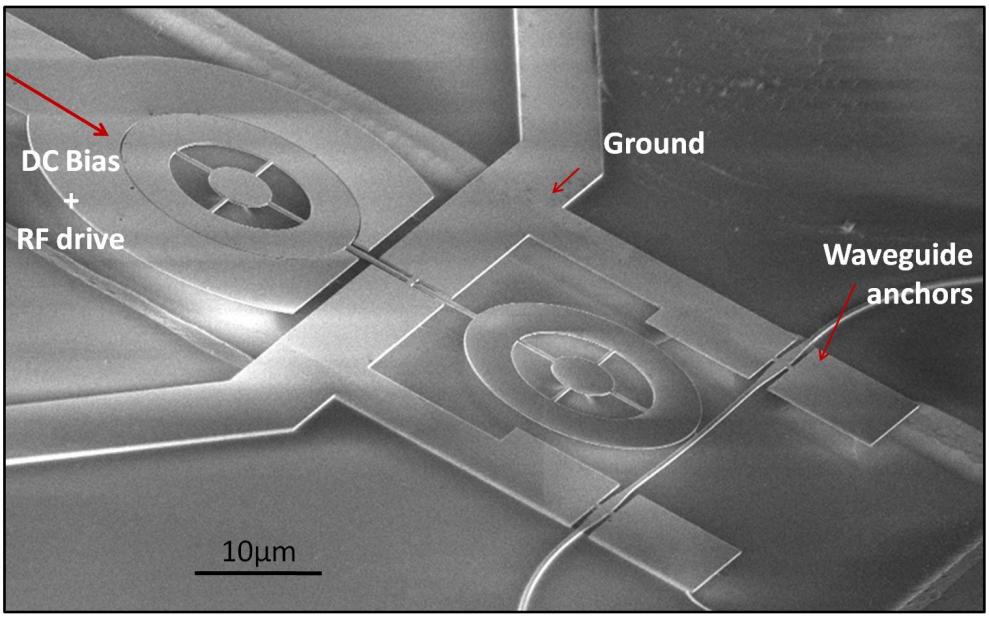

Figure 4.27: SEM image of a ring resonator based acousto optic modulator. The rings have a inner radius of 5.7μm and a width of 3.8μm

clockwise traveling wave mode. This coupling may be due to scattering from the coupling beam which transfers a part of the forward traveling mode into the backward traveling mode. The intrinsic quality factor observed for the optical mode is 45,500. The laser input is then biased at the half maximum of this resonance and the electro optic response is measured using the setup shown in 4.8. Figure 4.29 shows the electro optic response for an optical laser input of 25mW and RF input of 0dBm for two different bias voltages of 0V and 15V. When the bias voltage is 15V, a bunch of modes starting from a few MHz all the way upto 3.5GHz are observed. The fundamental mechanical resonance of the ring resonator where both the edges of the ring move in phase is at 176MHz and this response along with the mode shape is shown in figure 4.30. The second order mode where the two edges move out of phase as shown in figure 4.31 is observed at 1.122GHz. The insertion loss for an optical input of 11dBm, RF input of -10dBm and DC bias of 15V is around -30dB. The mechanical quality factor

of the resonance at 176MHz is 1,000 while that of the resonance at 1.122GHz is 2,500. These results demonstrates that the second mode of the ring can be used to obtain high frequency modulation.

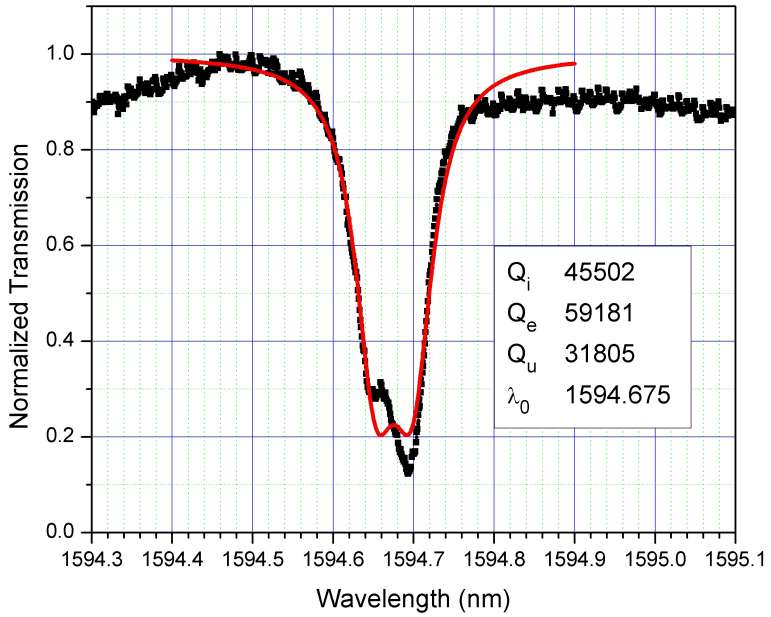

Figure 4.28: Optical transmission spectrum of ring optomechanical spectrum showing a split resonance with an intrinsic quality factor of 45,000

4.5 Chapter Summary

A process for the co-fabrication of silicon optomechanical with electrostatically excited mechanical resonators has been presented. A device which senses motion of the mechanical resonator using optical sensing has been fabricated. As the optical sensing is obtained as a modulation at the output, the device also acts as a narrowband optical modulator when the electrical input to the device is at the mechanical resonance frequency. The dependence of the various char-

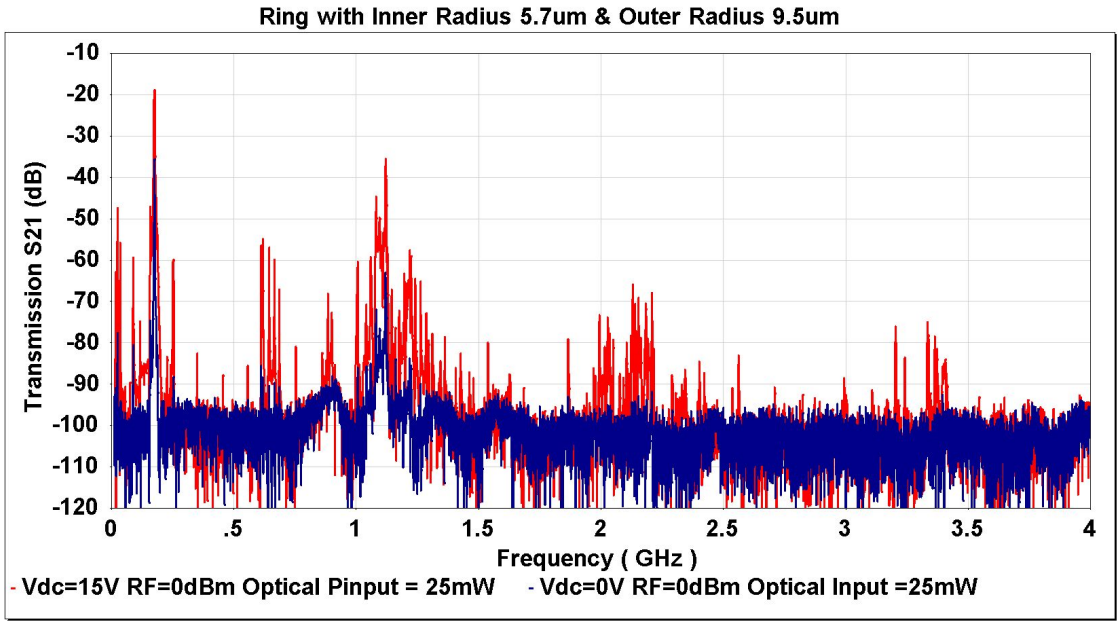

Figure 4.29: Electro optic response of the ring resonator based acousto optic modulator for 0V(blue) and 15V(red) dc bias

acteristics of the acousto optic modulator such as the insertion loss, extinction ratio and modulation index have been studied as a function of the input optical power, RF power and DC bias applied to the device. The mechanical quality factor limitations were attributed to anchor losses as established through finite element simulations in COMSOL. Simulations of an alternate scheme of anchoring through the coupling beam suggests higher quality factors to be achievable. Finally, a couple of geometries have been studied and fabricated to scale the modulator to higher frequencies. In the next chapter, an application of the acousto optic modulator as an oscillator is presented.

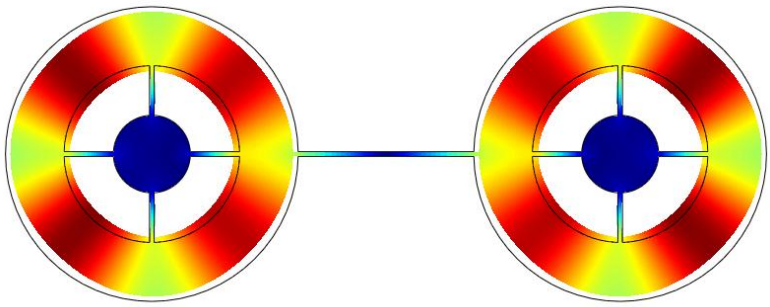

(a) Fundamental radial mode with simulated frequency at 174.43MHz

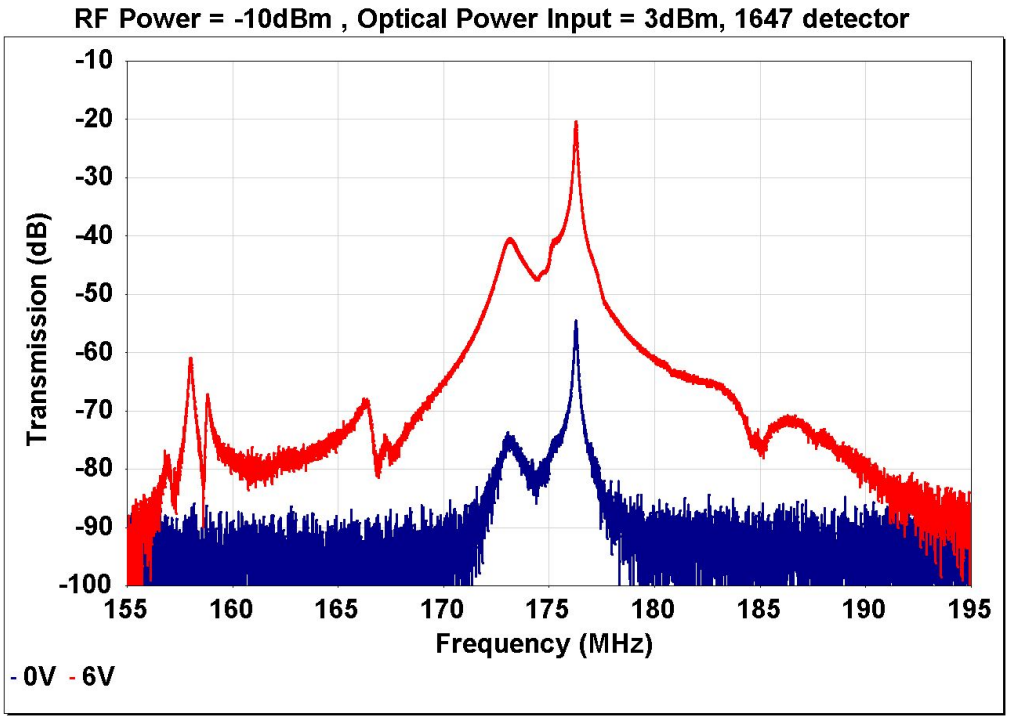

(b) Electro optic transmission spectrum of the ring resonator based modulator around the fundamental radial vibration resonance for DC bias of 0V(blue) and 6V (red)

Figure 4.30: Simulated mode shape in COMSOL and electro optic response for the fundamental vibrational mode of the ring resonator based AOM

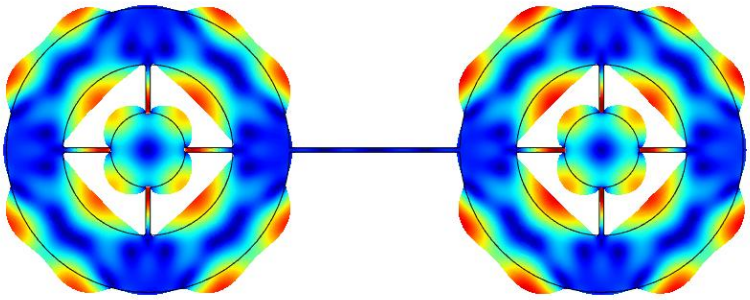

(a) Second oreder radial mode with simulated frequency at 1.1027GHz

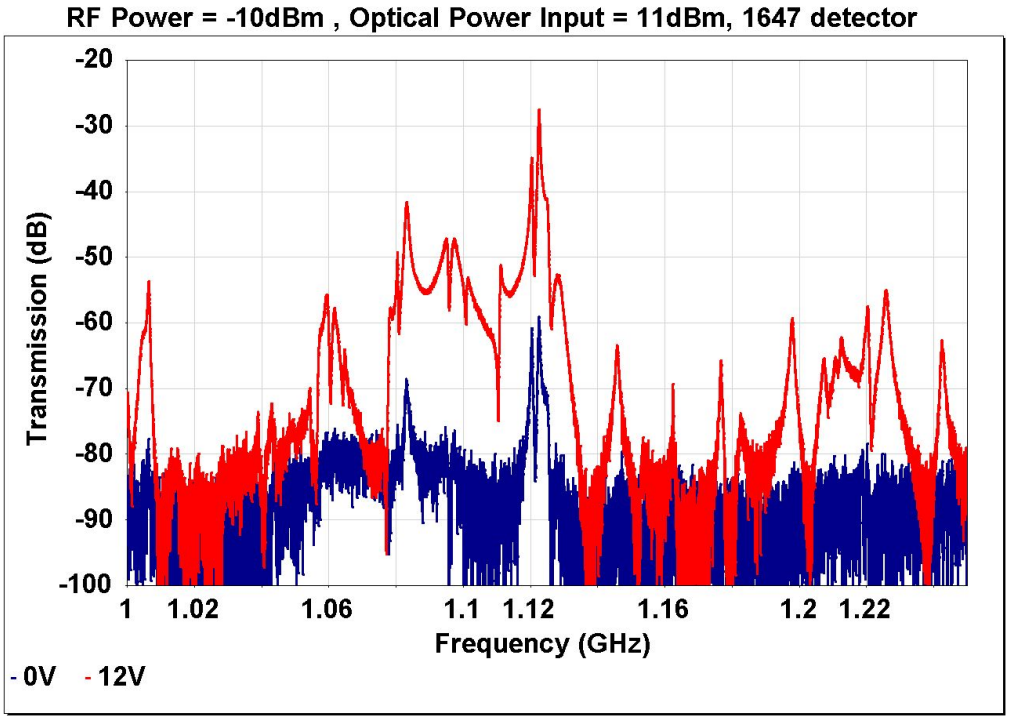

(b) Electro optic transmission spectrum of the ring resonator based modulator around the second order radial vibration resonance for DC bias of 0V(blue) and 12V (red)

Figure 4.31: Simulated mode shape and electro optic transmission response for the second order vibrational mode of the ring resonator based AOM

CHAPTER 5

THE OPTO ACOUSTIC OSCILLATOR

One important application for mechanical resonators has been their application in oscillators as the frequency selection elements. Piezoelectric quartz crystal resonators have been the typical choice of mechanical resonators for traditional oscillators. The thickness of the crystal and type of cut determine the frequency of oscillation. However, since these crystals are cut using a macroscopic process individually, the frequencies achievable are lower than that which can be obtained with micromechanical resonators.In addition, they are more expensive to manufacture as they are discrete components and have larger footprint than their micromechanical counterparts. Micromechanical resonators unlike quartz crystals also offer the potential for integration with feedback electronics on the same substrate.

In order to obtain an oscillator it is necessary to use a feedback loop around the resonator. The condition required for oscillation is set by the Barkhausen criterion. This criterion for oscillation requires that the overall loop gain be unity and the phase around the loop an integral multiple of 2π at the frequency of oscillation. The resonator in the oscillator acts to select one of the frequencies for which this condition is to be satisfied. To achieve the Barkhausen gain condition with the lossy resonator in the loop, an amplifier is required that compensates for the losses in the resonator and provides unity gain for the open loop. The other condition is ensured by either choosing an appropriate feedback circuit or using a phase shifting circuit to provide the correct phase at feedback. A typical electronic circuit to obtain oscillators using mechanical resonators is the Pierce oscillator circuit which consists of a transistor to provide the gain and a

combination of capacitors in feedback for the phase.

5.1 Oscillator using Acousto Optic Modulator

The mechanical resonator motion in the Acousto optic modulator is measured optically while the input is electrical. In order to obtain an oscillator from this resonator system, the output of the photodiode measuring the optical signal is amplified using an transimpedance amplifier. The voltage output obtained from the transimpedance amplifier is applied as the driving signal to the input of the resonator [52]. Figure 5.1 shows the setup used to convert the acousto optic modulator into an oscillator.

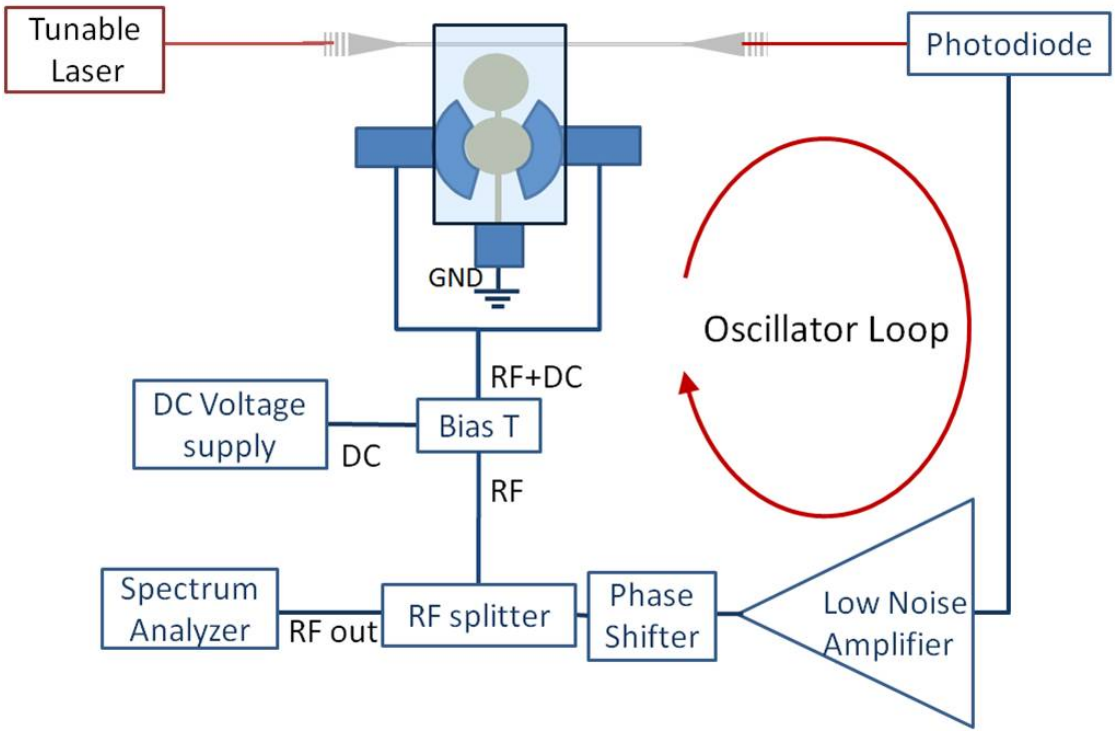

Figure 5.1: Setup to obtain an oscillator using the Acousto Optic Modulator

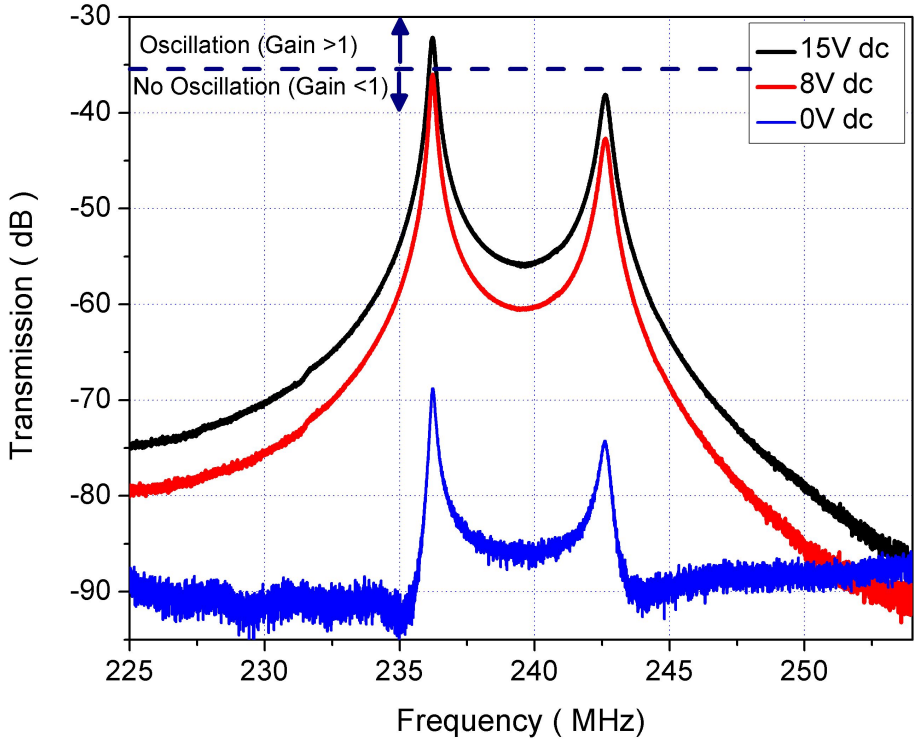

Figure 5.2: Transmission response of an Acousto Optic Modulator at DC bias of 0V(blue), 8V(red) and 15V(black). The insertion loss at which the overall loop gain is unity due to the amplifier gain of 36dB is shown by the line at -36dB

The gain provided by the amplifier used in the setup can be chosen depending on the losses in the resonator. For initial demonstration at 236MHz, the amplifier used is a MITEQ AM1412 with a power gain of 36dB. As explained earlier in the chapter on Acousto Optic modulator, the insertion loss in the electro optic transmission spectrum is controlled by the DC bias applied to the resonators. This is used to control the start and stop of oscillations in the loop.Figure 5.2 shows the transmission response for different DC bias along with the line depicting the insertion loss values at which the open loop gain becomes unity.

From this response, no oscillation is expected for DC bias below 8V. A threshold is expected around 8V and sustained oscillations above 8V. The behavior observed for the different DC bias voltages on a spectrum analyzer is shown in figure 5.3 and shows a good correspondence to the expected behavior. The amplifier gain and the DC bias is such that the gain condition is satisfied only for the fundamental mode at 236MHz. For a 15V DC bias, an output RF power of 6.5dBm is obtained at 236.22MHz. The oscillation waveform characterized using an oscilloscope is shown in figure 5.4 with a time period of 4.23ns. The output observed on the spectrum analyzer in figure 5.5 shows the presence of the higher harmonics of the fundamental oscillation frequency. The cause of this is believed to be the non-linearity in the optical transfer characteristics due to the Lorentzian response of the optomechanical resonator.

5.1.1 Oscillator at higher frequencies

In the previous chapter, the scaling of the acousto optic modulator to higher frequencies was presented. The first approach of scaling the disk led to high insertion losses, which makes completing the oscillation loop harder due to the higher gain required. The second approach for modulators at higher frequencies used the ring resonator geometry and higher order modes. While the insertion loss in these devices at high frequencies is low, the fundamental ring modes have a much stronger response than the higher order modes. The amplifiers used to provide feedback for these modes must therefore provide gain only around the higher frequency. Figure 5.6 shows the schematic for a ring resonator modulator based oscillator operating with the broadband MITEQ 1412 amplifier. It is seen that this setup excites oscillations in the fundamental mode

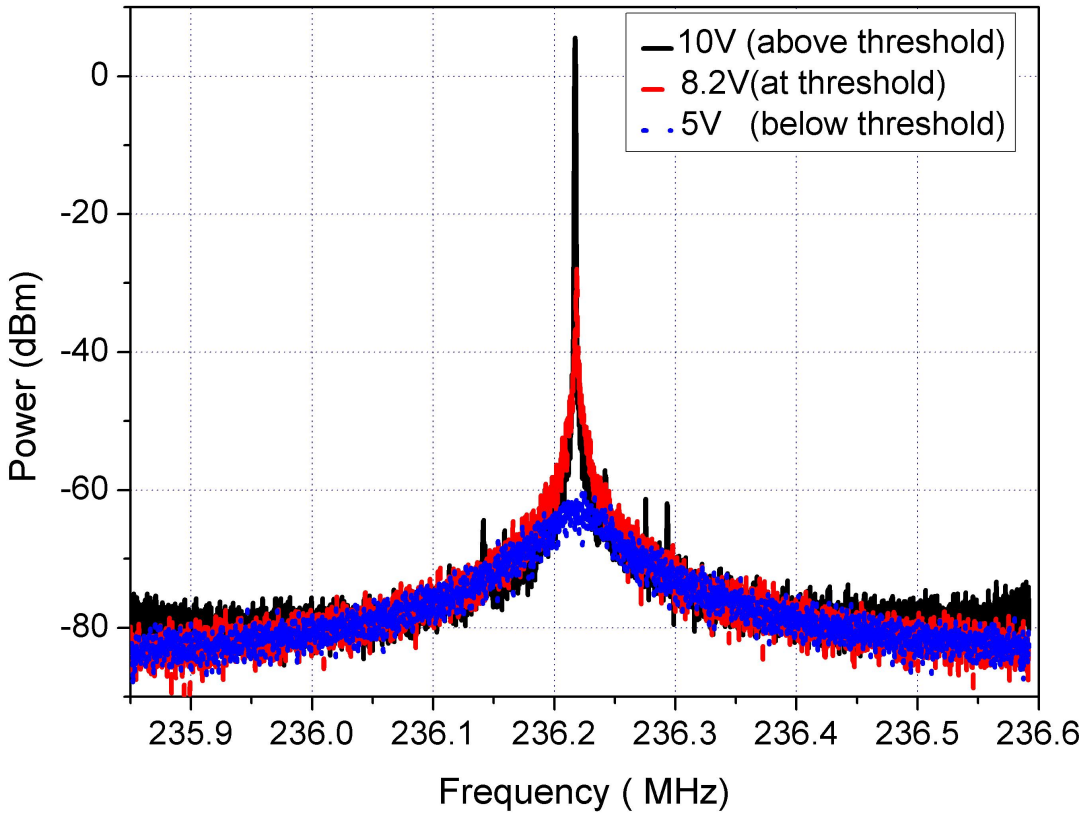

Figure 5.3: Spectrum obtained at the Spectrum analyzer using the setup shown in figure 5.1 for different DC bias voltages applied to the modulator

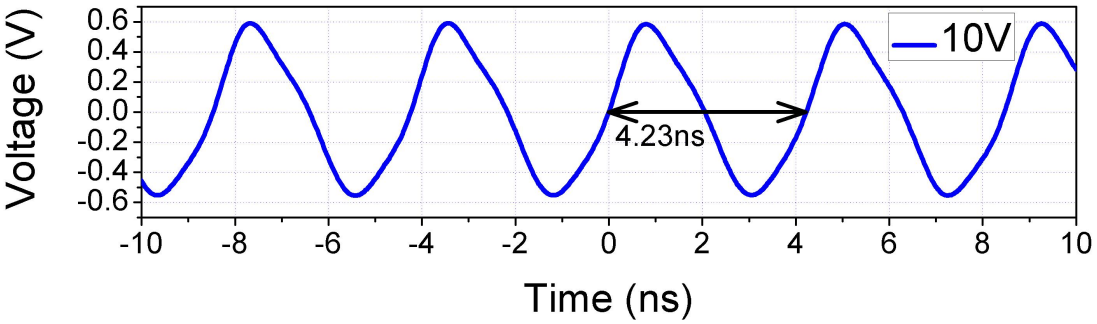

Figure 5.4: Oscillation waveform of the Opto-Acoustic Oscillator with a time period of 4.23ns observed on an oscilloscope

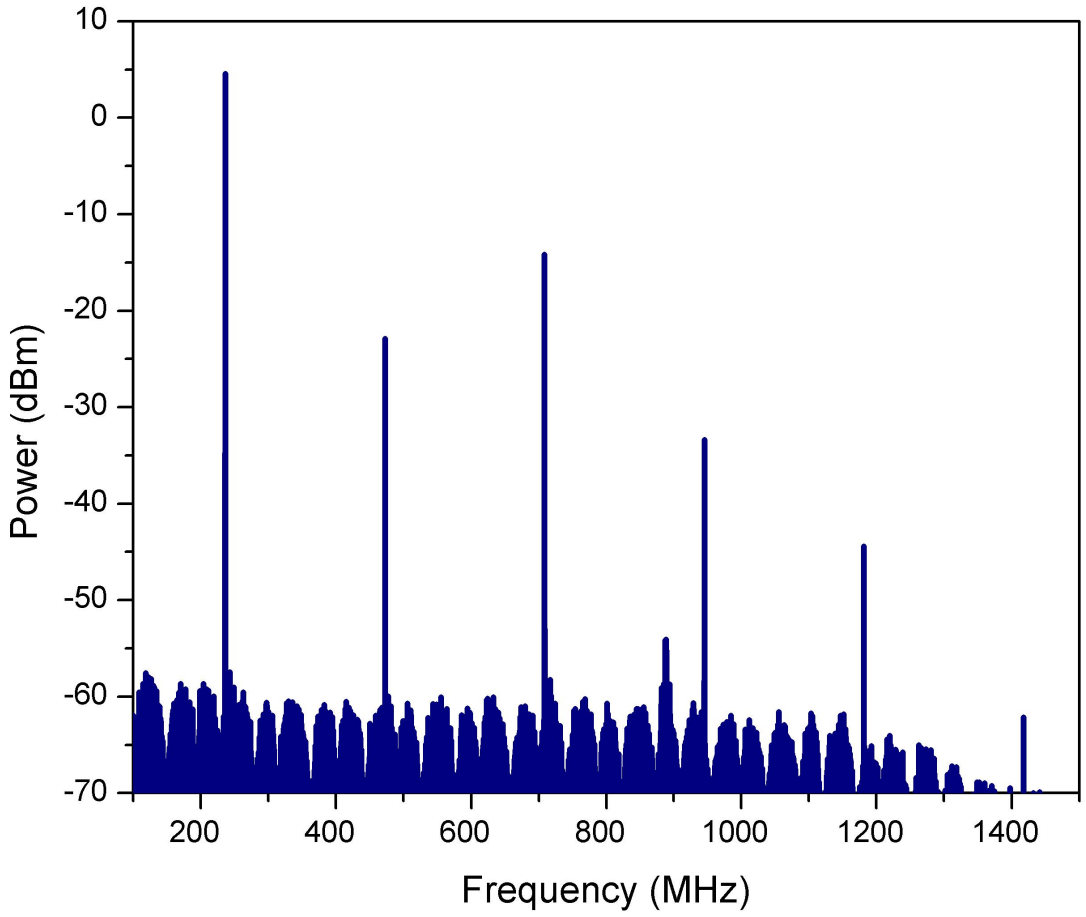

Figure 5.5: Output of the Opto-Acoustic Oscillator on the spectrum analyzer showing the presence of higher harmonics of the fundamental oscillation frequency

of the ring resonator at 176MHz. The response of the oscillator as observed on the spectrum analyzer for an optical input of 6dBm and a DC bias of 8V is shown in figure 5.7 . To excite the higher order mode around 1GHz which has a higher insertion loss, a setup whose schematic is shown in figure 5.8 is used. A combination of available amplifiers and attenuator is used to obtain the required narrowband response with the necessary gain. An attenuator is used to limit the gain as the combination of the amplifiers can provide excess RF power which could damage the modulator. The oscillator output observed at the spec-

trum analyzer for an optical input of 11dBm and 6.5V DC bias is shown in figure 5.9.

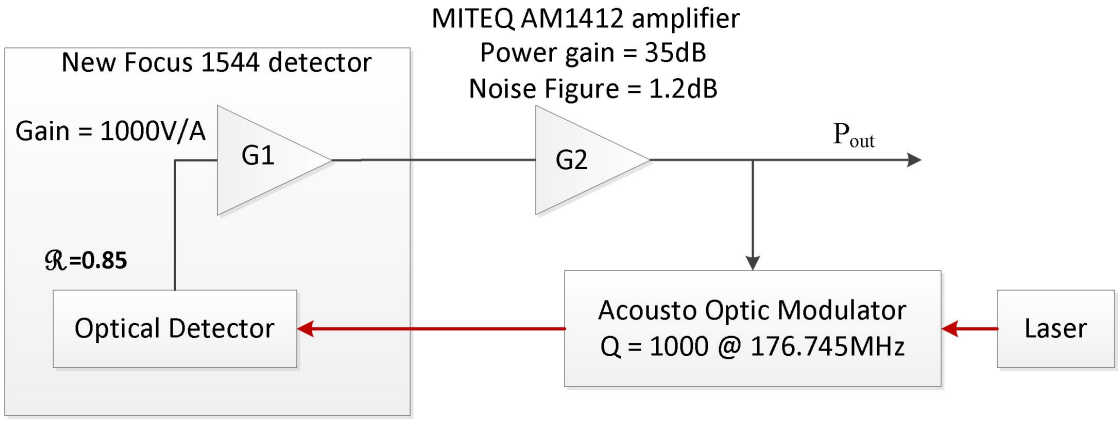

Figure 5.6: Schematic of the OAO setup used for the ring resonator modulator based oscillator showing the component parameters.

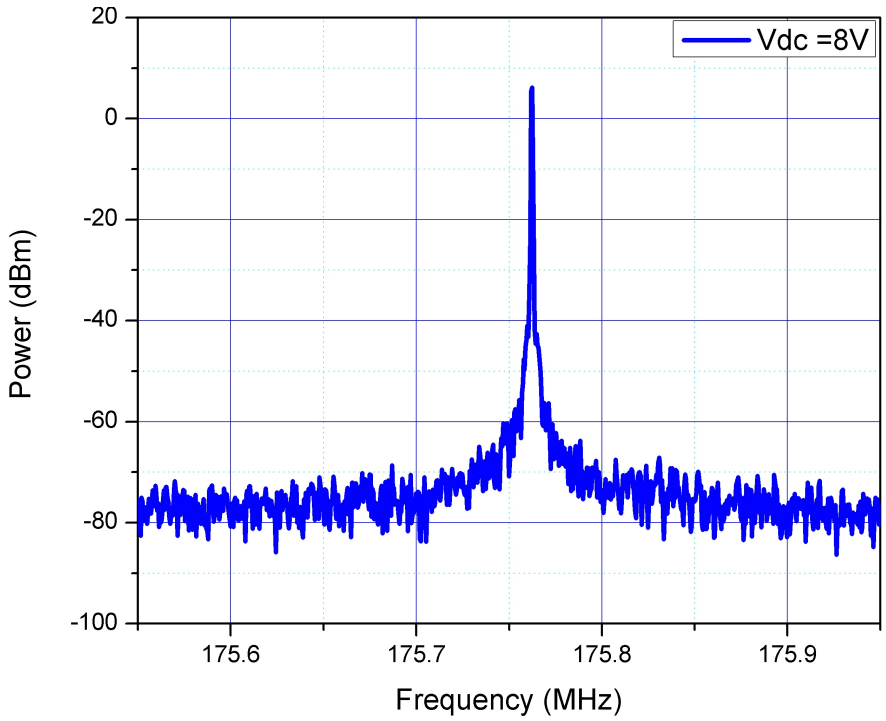

Figure 5.7: Oscillation at the fundamental ring resonator mode at 175.76MHz observed on the oscilloscope

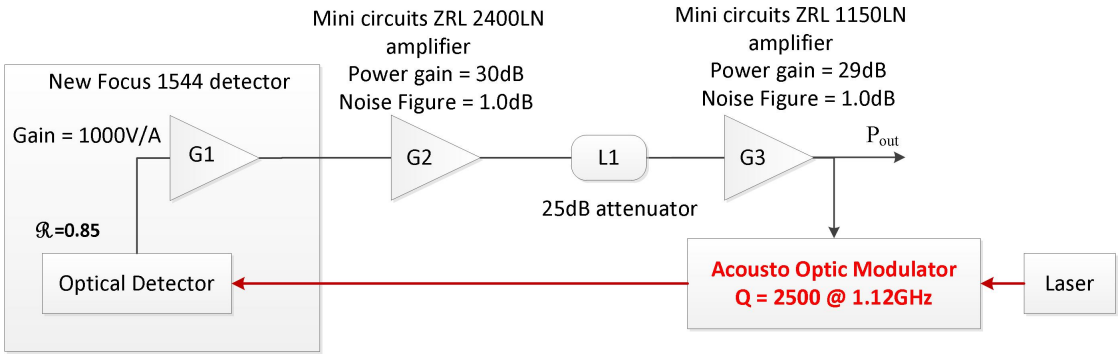

Figure 5.8: Schematic of the OAO setup used for the higher order ring resonator modulator based 1Ghz oscillator with two amplifiers and an attenuator

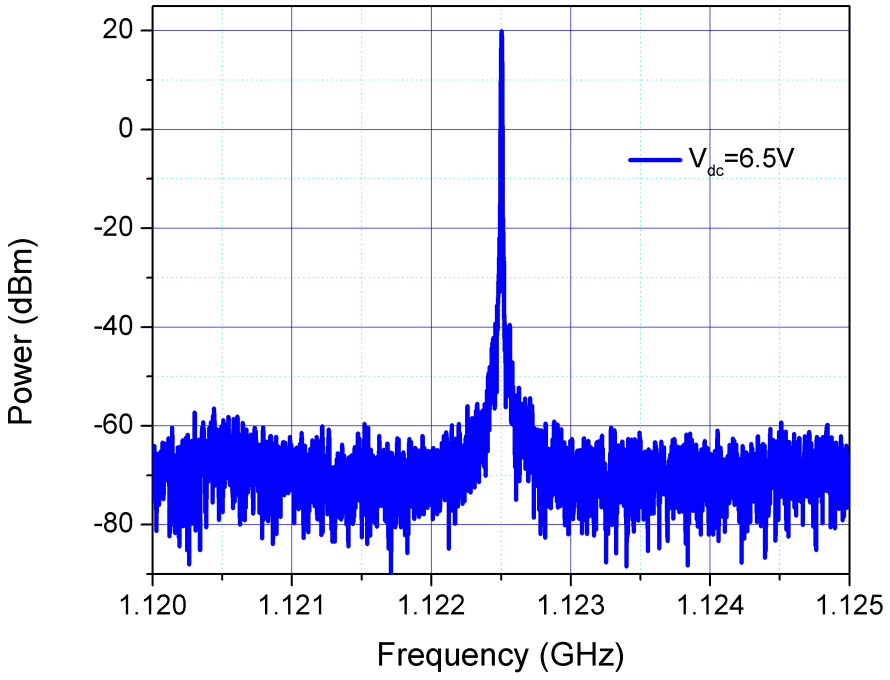

Figure 5.9: Oscillation at the higher order radial mode of ring resonator mode at 1.122GHz observed on the oscilloscope

5.2 Oscillator Phase Noise

In this section, a model for the phase noise of the oscillator is obtained by studying the noise characteristics of the components in the oscillator loop. The effect of phase noise at the oscillator output is understood by starting with an ideal oscillator. The output signal of an ideal electrical oscillator can be represented as voltage signal

$$v(t) = V_0 \cos(\omega_0 t + \phi) \tag{5.1}$$

where V_0 is the peak amplitude, $\omega_0 = 2\pi\nu_0$ is the angular frequency and ϕ is a constant phase. Equivalently, the signal can be represented by a complex phasor $\mathbf{V}$ by factoring out the $\omega_0 t$ oscillation

$$\begin{aligned} \mathbf{V} &= V_0 e^{j\phi} \\ \mathbf{V} &= V_0(cos\phi + jsin\phi) \end{aligned} \tag{5.2}$$

When the amplitude and the phase have slow time variations compared to the $\omega_0 t$ oscillation, these changes can be absorbed into the complex phasor.

$$\tilde{v} = V(t)e^{j\phi(t)} \tag{5.3}$$

In reality, the oscillator signal has noise components in the amplitude and phase which can be represented in the voltage signal as (5.4).

$$v(t) = V_0(t)[1 + \alpha(t)] \cos(\omega_0 t + \phi(t)) \tag{5.4}$$

where $\alpha(t)$ and $\phi(t)$ are the noise in amplitude and phase. The voltage noise added can be represented in the phasor domain by an in-phase component $v_x(t)$ and quadrature component $v_y(t)$ as

$$v(t) = V_0 + v_x(t) + jv_y(t) \tag{5.5}$$

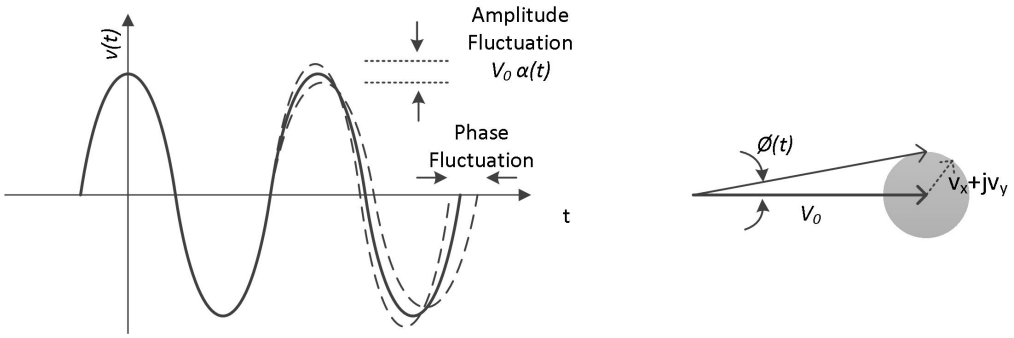

Figure 5.10: Amplitude and phase noise of the oscillator in the time domain and in the phasor representation

From this equation we see that the phase added is given by $\phi(t) = \frac{tan^{-1}v_y(t)}{V_0+v_x(t)}$. For low noise givrn by $|v_x/V_0| << 1$ this reduces to

$$\phi(t) = \frac{v_y(t)}{V_0} \tag{5.6}$$

Converting to represent power spectral density, the phase noise of power spectral density is measured by taking the ratio of the power spectral density of noise in quadrature with the oscillator signal to the oscillation power.The unit of measurement thus is dBc/Hz which stands for "dB below carrier in a 1Hz measurement bandwidth". The phase noise of an oscillator is obtained by first considering the noise added by the constituent elements of the oscillator individually in a open loop configuration. The loop is then closed using the phase transfer function in order to obtain the phase noise power spectral density of the oscillator. The two components which form part of the oscillator loop where noise is added are the optical detector and the electrical amplifiers.

5.2.1 Phase Noise in optical detectors

The optical output from the modulator in a opto acoustic oscillator is converted back into the electrical domain using a photodetector. The photodetector is a diode in which a reverse biased junction collects light and convert them into electron hole pairs. For a given optical power $P(t)$ incident on the detector, the output photocurrent is given by

$$i(t) = \Re P_l(t) = \frac{q\eta}{h\nu} P_l(t) \tag{5.7}$$

where $i(t)$ is the photocurrent corresponding to a responsivity $\Re$ given in A/W. The responsivity $\Re$ can be expressed as the charge q times the quantum efficiency with which carriers are generated η multiplied by the number of photons incident given by $\frac{P_l(t)}{h\nu}$. The discrete nature of photons and charge carriers leads to a white noise in the current at the photodetector with spectral density which is represented by the expression

$$S_i(\nu) = 2q\bar{i} = 2q\Re\overline{P}_l \tag{5.8}$$

with units A^2/Hz where $\bar{i}$ and $\overline{P}$ are the average current output and optical power input to the detector.When the detector is terminated by a resistance R, the power spectrum of the shot noise is

$$S_i(\nu) = 2q\bar{i}R = 2q\Re\overline{P}_l R \tag{5.9}$$

given in W/Hz.When the input optical signal is modulated sinusoidally with modulation index m , the output current from the photodetector is

$$i(t) = \Re\overline{P}_l(1 + mcos\omega_0 t) \tag{5.10}$$

The time averaged electrical power fed into a load resistance R_0 at the ac frequency ω_0 is then

$$P_0 = \frac{1}{2} m^2 \Re^2 \overline{P}_l{}^2 R_0 \tag{5.11}$$

The phase noise power spectral density due to shot noise is a ratio of the shot noise to the output power and is given by by $S_\phi(f) = b_0 = S_i/P_0$. Using (5.9) and (5.11) this comes out to

$$b_0 = \frac{4q}{m^2 \Re P_l} \tag{5.12}$$

5.2.2 Phase Noise in amplifiers

There are two kinds of noise associated with the amplifier, the thermal noise and flicker noise.

Thermal Noise

The thermal noise is white noise and is specified by the noise figure F for an amplifier. Consider a resistor at the input of an amplifier with voltage gain A. The noise due to the thermal noise in this resistor is given by

$$N_r = kT_0 \tag{5.13}$$

When this resistor is input matched to the input impedance of the amplifier, the equivalent input referred noise power spectral density N of the amplifier can be written as

$$\begin{aligned} N_a &= (F-1)kT_0 \\ N &= N_a + N_r = FkT_0 \end{aligned} \tag{5.14}$$

The total noise in bandwidth B given by NB consists of a half ($\frac{1}{2}NB$) of power in amplitude noise and phase noise respectively. Considering the two sidebands that exist around the carrier, the power spectral density in the phase component is NB. This gives the phase noise power spectral density for an input power P_0

into the amplifier to be

$$\begin{aligned} S_\phi(f) = b_0 &= \frac{N}{P_0} \\ &= \frac{FkT_0}{P_0} \end{aligned} \tag{5.15}$$

Thermal Noise of cascaded amplifiers

The total noise power spectral density of all cascaded amplifiers with power gain $A_1^2, A_2^2, ...A_n^2$ can be referred the input of the first amplifier as

$$N = kT_0 + (F_1 - 1)kT_0 + \frac{(F_2 - 1)kT_0}{A_1^2} + \frac{(F_3 - 1)kT_0}{A_1^2 A_2^2} + ... \tag{5.16}$$

Flicker Noise

Flicker Noise is a low frequency noise caused in amplifiers due to fluctuations of the gain of the transistor due to random processes affecting the carrier density [53]. The flicker noise power spectral density has a $1/f$ dependence and is equal to the white noise at the corner frequency f_c. The flicker phase noise power spectral density can be described by

$$s_\phi(f) = \frac{b_{-1}}{f} \tag{5.17}$$

where the coffecient b_{-1} is an experimentally determined parameter. By the definition of corner frequency

$$\begin{aligned} f_c &= \frac{b_{-1}}{b_0} \\ b_{-1} &= \frac{f_c FkT_0}{P_0} \end{aligned} \tag{5.18}$$

Therefore, the coeffecient b_{-1} can be obtained by experimentally measuring the corner frequency of the flicker noise of the amplifier.

The total noise spectral density in the amplifier can be expressed as a sum of the white noise and flicker components using (5.16) and (5.18)

$$S_{amp}(f) = N + \frac{b_{-1}P_0}{f} \tag{5.19}$$

5.2.3 Oscillator Phase Noise using phase transfer function

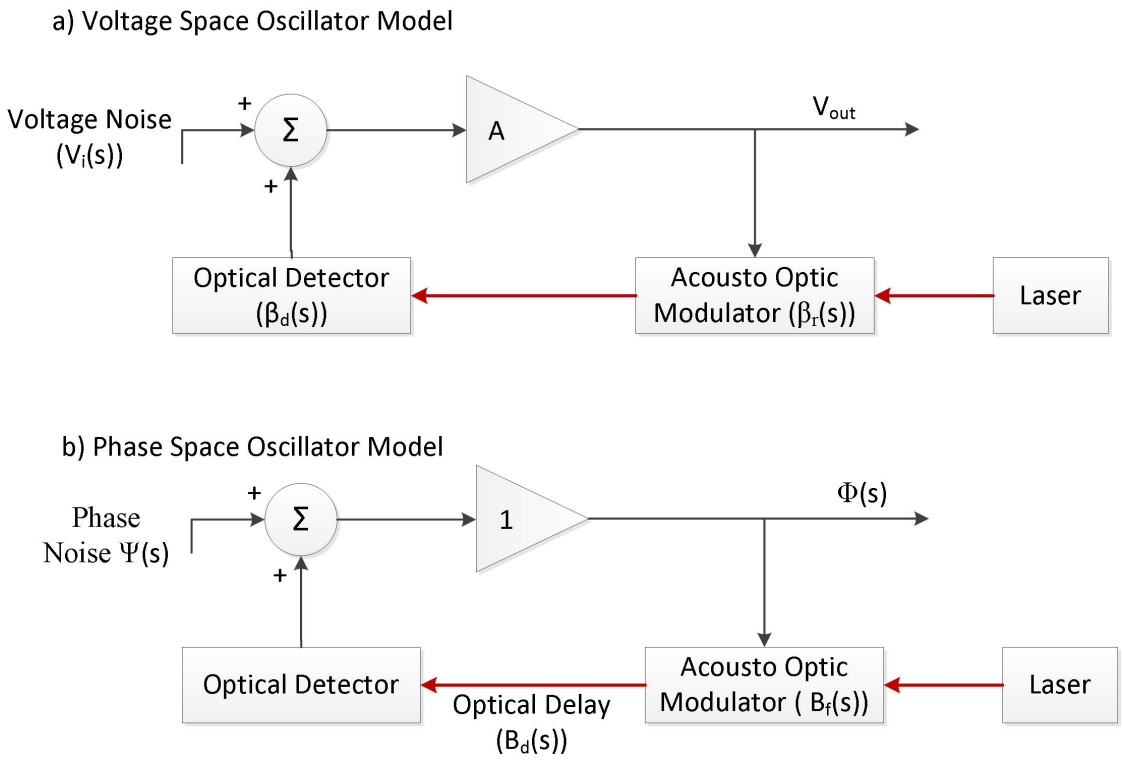

Figure 5.11: The voltage space oscillator model is shown in (a). Around oscillation, the loop gain is 1 and the loop phase response is obtained by considering the phase transfer function of the resonator $B_f(s)$ and the delay line $B_d(s)$ as shown in (b)

The oscillator is an inherently nonlinear system. However around the oscillation , the phase noise is always a small perturbation. Thus, to describe the phase noise, we can describe an oscillator phase transfer function for the system

shown in figure 5.11. This model describes phase perturbations around a stationary oscillation, for which $A\beta(j\omega) = 1$ at the oscillation frequency. The phase transfer function $B_f(s)$ and $B_d(s)$ are the Laplace transforms of the phase impulse response around the oscillation frequency as outlined in [54]. The input signal $\Psi(s)$ models the noise from the amplifier's phase noise and other sources connected to the amplifier input as described in the previous section. The oscillator phase-noise transfer function is defined as

$$H(s) = \frac{\Phi(s)}{\Psi(s)} \tag{5.20}$$

and the phase noise power spectral density of the oscillator is obtained using the phase-noise transfer function defined above by

$$S_\phi(\omega) = |H(j\omega)|^2 S_\psi(\omega) \tag{5.21}$$

where $S_\phi(\omega)$ is the phase noise power spectral density at the output of the oscillator $S_\psi(\omega)$ is the phase noise power spectral density of the components in the loop. Using the basic relations of the loop components, the phase-noise transfer function can be written in terms of the phase transfer functions of the loop components as

$$H(s) = \frac{1}{1 - B(s)} = \frac{1}{1 - B_d(s)B_f(s)} \tag{5.22}$$

The phase transfer function of the resonator and the delay line are [54]

$$\begin{aligned} B_d(s) &= e^{-s\tau_d} \\ B_f(s) &= \frac{1}{1 + s\tau_f} \end{aligned} \tag{5.23}$$

where τ_d is the time delay of the delay line and $\tau_f = \frac{2Q}{\omega_0}$ is the lifetime of the resonator filter with quality factor Q. The phase-noise transfer function is then

$$H(s) = \frac{1 + s\tau_f}{1 + s\tau_f - e^{-s\tau_d}} \tag{5.24}$$

This simplifies to

$$|H(j\omega)|^2 = \frac{1 + \omega^2\tau_f^2}{2 - 2\cos\omega\tau_d + \omega^2\tau_f^2 + 2\omega\tau_f \sin\omega\tau_d} \tag{5.25}$$

To obtain the phase noise power spectral density of the oscillator from this expression, we make use of (5.21), (5.25) to get

$$S_\phi(\omega) = \frac{1 + \omega^2\tau_f^2}{2 - 2\cos\omega\tau_d + \omega^2\tau_f^2 + 2\omega\tau_f \sin\omega\tau_d} S_\psi(\omega) \tag{5.26}$$

When there is no time delay in the optical feedback loop i.e. $\tau_d << \tau_f$, the phase transfer function reduces to

$$\begin{aligned} H(j\omega) &= \left(1 + \frac{1}{\omega^2\tau_f^2}\right) \\ &= \left(1 + \frac{\omega_L^2}{\omega^2}\right) \\ S_\phi(\omega) &= \left(1 + \frac{\omega_L^2}{\omega^2}\right) S_\psi(\omega) \end{aligned} \tag{5.27}$$

which is the well known Leeson's model for the phase noise of an oscillator with Leeson frequency $\omega_L = 2Q/\omega_0$. This further simplifies to

$$S_\phi(f) = \left(1 + \frac{1}{f^2}\left(\frac{\nu_0}{2Q}\right)^2\right) S_\psi(f) \tag{5.28}$$

In addition, it is equivalent to look at the phase noise power spectral density at the output of the amplifier stages rather than at the output of the photodiode. The phase noise at the output of the photodiode is

$$S_\psi(f) = \frac{S_{shotnoise} + S_{amp}(f)}{P_d} \tag{5.29}$$

where $S_{shotnoise}$ is the shot noise at the photodiode output (5.9) and S_{amp} is the input referred noise of the cascaded amplifiers (5.19). On passing through the amplifiers, the phase noise power spectral density added from the different com-

ponents at the output point is

$$\begin{aligned} S_{\psi}(f) &= \frac{G_1 G_2 \left(S_{shotnoise} + S_{amp}(\omega) \right)}{G_1 G_2 P_d} \\ &= \frac{G_1 G_2 \left(S_{shotnoise} + S_{amp}(f) \right)}{P_{out}} \end{aligned} \tag{5.30}$$

As described in the earlier section, the noise power spectral densities of the amplifier has a dependence on frequency. On combining (5.30) with (5.28), the frequency dependence of the oscillator phase noise is a function of the leeson frequency and amplifier flicker noise corner frequency . Figure 5.12 shows the phase noise plotted against frequency offset from oscillation frequency in a log-log plot for two different cases of the amplifier flicker noise corner frequency. The first plot (bottom left of figure 5.12) represents the case when the flicker noise corner frequency (f_c) is less than the Leeson frequency (f_l).In this case, the phase noise power spectral density has a $1/f^3$ dependence close to the carrier up to the frequency offset corresponding to the flicker noise corner frequency, beyond which there is a $1/f^2$ dependence up to the Leeson frequency. Above the Leeson frequency, the phase noise of the oscillator has no dependence on offset frequency. In the second case, when the amplifier flicker frequency is close to the Leeson frequency of the oscillator, there is a $1/f^3$ dependence up to the corner frequency and a white response beyond that frequency.

5.2.4 Verification of phase noise model

The phase noise model developed above is verified using the optoacoustic oscillator. The phase noise of the oscillator is measured using an Agilent Signal source analyzer. The schematic of the components used in the ring resonator based oscillator is shown in figure 5.6. The parameters that are unknown in

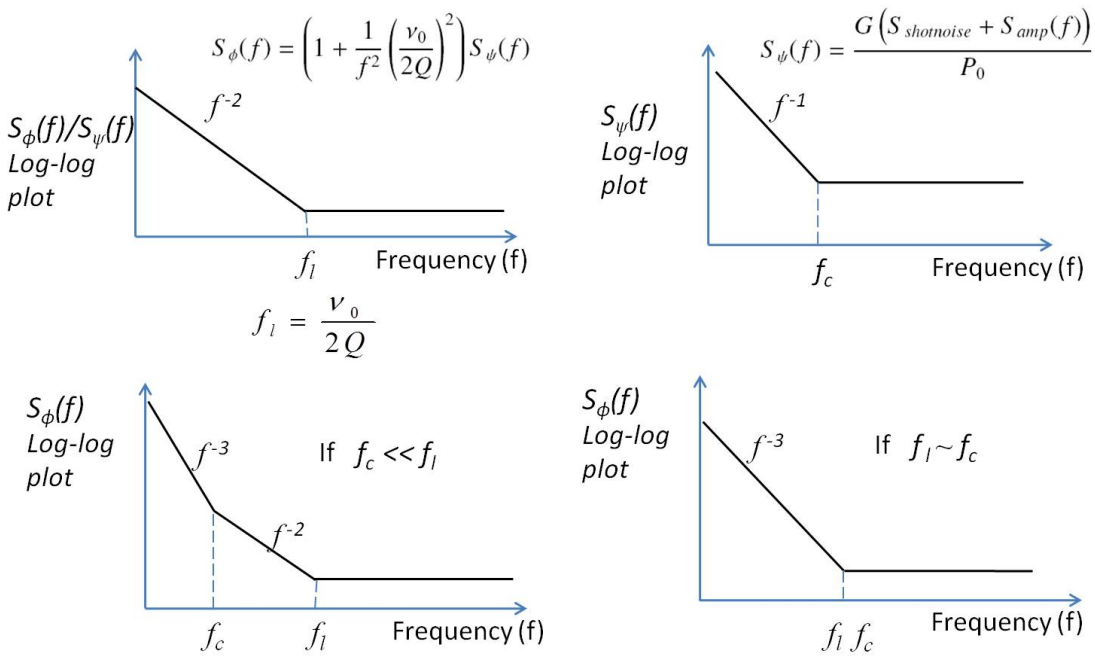

Figure 5.12: (top left) Log-log plot of the loop phase transfer function versus carrier offset frequency showing a $1/f^2$ dependence upto the Leeson frequency and white beyond (top right) Log-log plot of the phase noise spectral density of the components versus carrier offset frequency (bottom left) Log-log plot of the phase noise power spectral density for the case when flicker noise corner frequency is less than the Leeson frequency (bottom right) Log-log plot of the phase noise power spectral density for the case when flicker noise corner frequency is close to the Leeson frequency.

this setup are the noise figure of the inbuilt trans impedance amplifier of the new focus 1544 detector and the slope of the flicker phase noise power spectral density b_{-1}. These unknown components are extracted by performing a fit to a phase noise measurement of the oscillator for a given optical input power. The model is then verified by varying the optical input power, which causes the oscillator output to operate at different RF powers. The changing RF oscillation

power due to a change in optical input power is due to the dependence of the RF insertion loss of the modulator on the optical power input as described in the previous chapter. To evaluate the unknown components,we look at the phase noise of the 176MHz oscillator for an optical input of 6dBm to the acousto optic modulator.At this optical input power level, the average power level at the detector is $23\mu W$ at the half maximum operation point of the modulator. A noise figure of 3.2dB and a slope b_{-1} of $2.785 \times 10^{-8} rad^2$ provide a good fit using equation (5.28) to the measured phase noise as shown in figure 5.13. To verify the

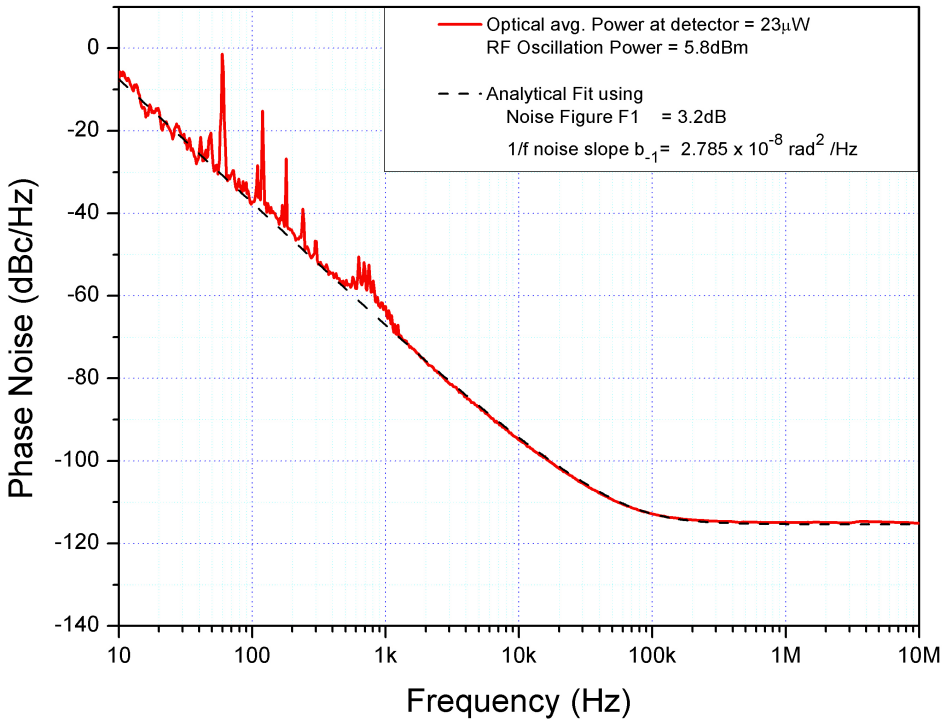

Figure 5.13: Extraction of the amplifier noise figure and flicker noise slope from the measured phase noise of a 176.76MHz opto acoustic oscillator

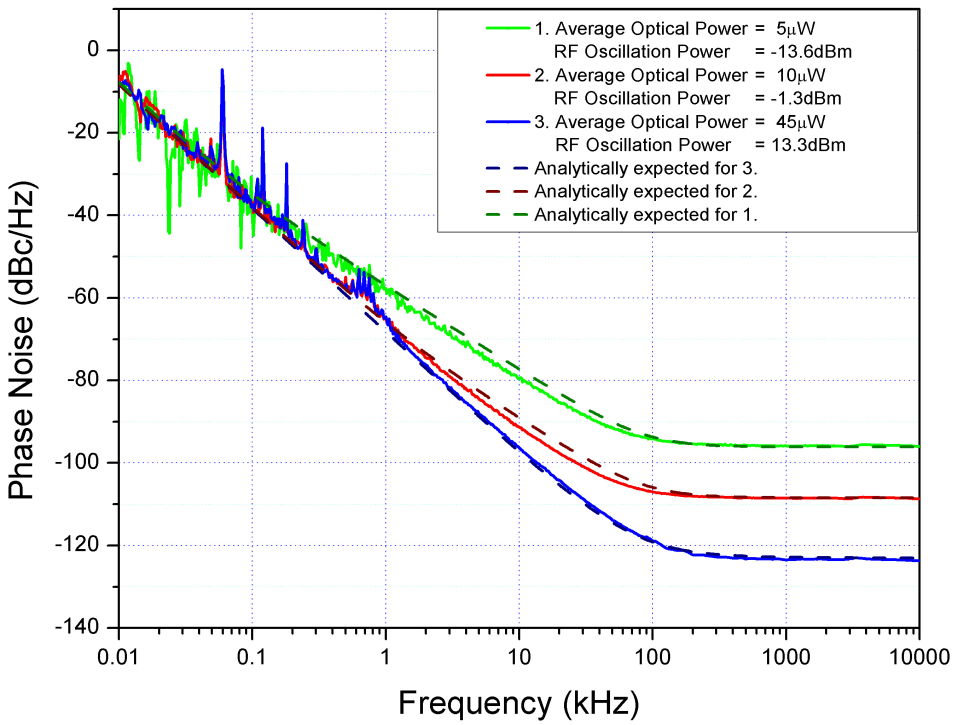

Figure 5.14: Measured phase noise for 176.76MHz oscillator operating with different optical input powers and output RF oscillation powers and an analytical prediction for the phase noise

phase model, the optical power from the laser is varied which changes the optical power at the detector and the RF oscillation power at the output. The theoretical predicted phase noise on changing optical power is obtained by using the extracted numbers from the first measurement. The plots in figure 5.14 show a good agreement between the measured and the analytical model predictions for the 176.76MHz oscillator. The values extracted for the detector noise figure and amplifier flicker noise corner frequency are also verified for a 236MHz modulator using the setup shown in figure 5.15. This setup uses the disk res-

onator based modulator to obtain oscillations at 236MHz with the same detector and amplifier as the 176MHz oscillator. This allows for further verification of the model with a different set of data from another oscillator. The analytically expected phase noise and the corresponding phase noise measurement for the 236MHz oscillator is shown in figure **??**. It is seen that there is a good match between the theoretical and measured phase noise values. The measured phase noise data resembles the case of the flicker noise frequency being lower than the Leeson frequency as shown in the bottom left plot of figure 5.12. The measured phase noise has a $1/f^3$ dependence upto a frequency of 1kHz beyond which the slope changes to $1/f^2$ up to the Leeson frequency.

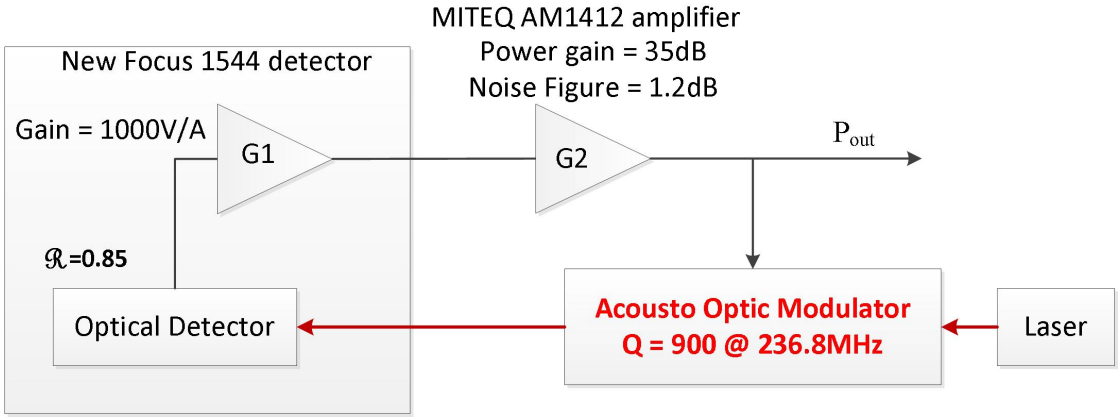

Figure 5.15: Schematic of the OAO setup used for the 236MHz disk resonator modulator based oscillator

Figure 5.17 is the phase noise obtained for the 1.12GHz ring resonator modulator based oscillator whose setup is shown in figure 5.8. The output shows an $1/f^3$ all the way upto the Leeson frequency suggesting that the flicker noise corner is at the same frequency as the Leeson frequency. A study similar to the 236MHz and 176MHz by varying optical power was not possible as the RF insertion losses for the higher order mode are higher and oscillations exist only at

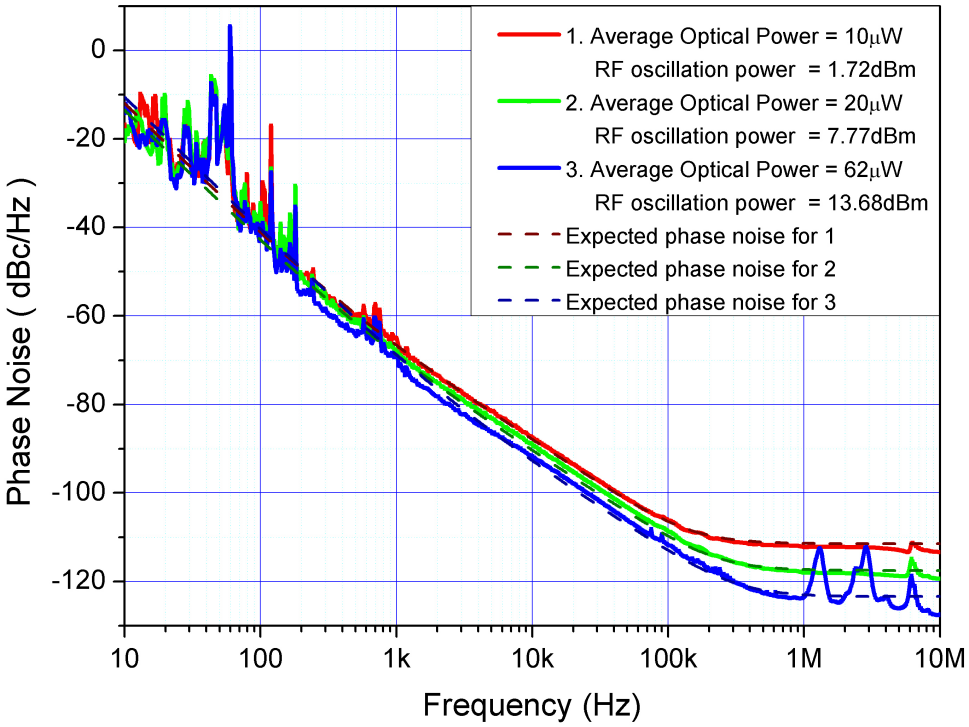

Figure 5.16: Measured phase noise for 236MHz oscillator operating with different optical input powers and output RF oscillation powers along with the analytical prediction for the phase noise

higher input optical powers.

5.3 Improving the Opto-Acoustic Oscillator

The opto-acoustic oscillator presented in the chapter used optical feedback to close the loop around a mechanical resonator to obtain oscillations. The spectral purity of the oscillator which is specified by the phase noise of the oscillator is determined in this case by two factors, the mechanical quality factor and

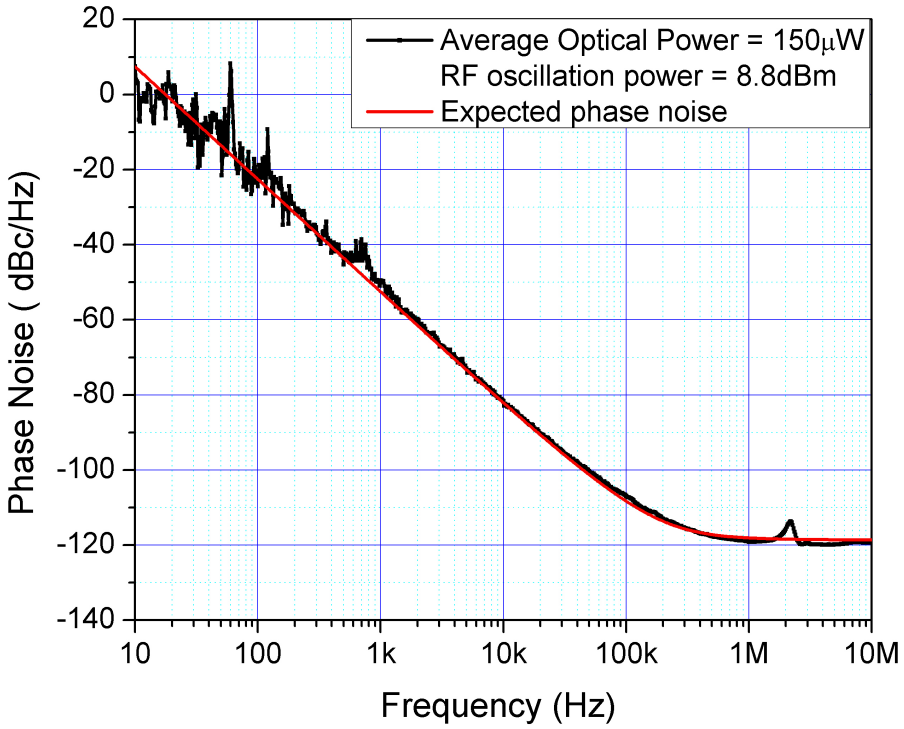

Figure 5.17: Measured phase noise for 1.12GHz oscillator along with the theoretical predicted phase noise

the noise introduced by the amplifiers and photodetector. The scheme of using optical feedback is very similar to the optical delay line based Opto-Electronic Oscillator(OEO) which is the current state-of-art RF oscillator. The schematic of a typical OEO as shown in figure 5.18 consists of an optical modulator whose output is sent through a long fiber delay line before being converted back into the electrical domain using a high speed photodiode [55, 56]. The electrical signal is then amplified and sent through an RF filter before being fed back into the optical modulator. There are multiple radio frequencies that can be sustained in the combined optical-electrical cavity formed by the modulator - optical fiber -

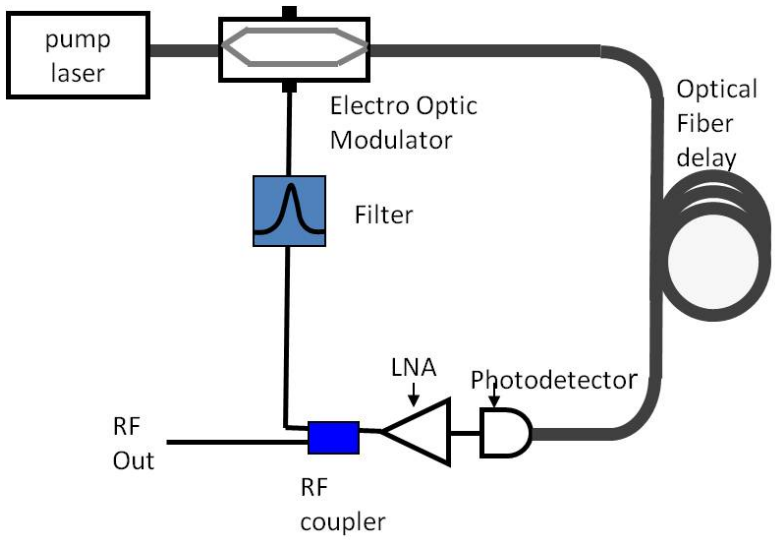

Figure 5.18: Schematic of Opto-Electronic Oscillator(OEO)

electrical amplifier system. The RF filter acts to choose one of these frequencies for oscillation in the loop by allowing the gain condition for oscillation to be satisfied for only one mode of the entire cavity. The very good spectral purity of the oscillator is obtained by the use of a fiber optical delay line which allows a large time delay at high radio frequencies without introducing much loss. The equivalent quality factor of the delay line as outlined in the phase noise section by the phase transfer function of the delay line can be specified by $\omega_{rf}\tau_{delay}/2$. For time delays of 1$\mu$s at 10GHz, the equivalent quality factor is about 30,000 which is not obtainable with any other resonator technology. In addition the low loss of the optical fiber eliminates the need for a very high gain amplifier in the loop which can introduce noise. From a comparison of the schematic of the OEO and the OAO, it is seen that the two approaches are very similar. The OAO combines the optical modulator and RF filter into a single unit eliminating the inefficiencies associated with two separate components. In addition, the demonstration of the OAO used a very small length of optical fiber in the feed-

back loop and thereby no time delay in the loop. By including a longer section of fiber based time delay it would be possible to obtain the performance advantage of the OEO into an OAO. In addition, there have been attempts to scale the OEO to the micro scale by the use of high quality factor micro-resonators in the optical domain to obtain large group delays [57]. The OAO has established a scheme for scaling and combining the optical modulator and RF filter as an integrated solution at the microscale. Thus, by including an optical resonator based delay element to the OAO loop, a micro scale platform for combining the best of the two worlds of optical time delay and high quality factor mechanical resonance can be obtained.

CHAPTER 6

CONCLUSION AND FUTURE WORK

In the previous chapters, a CMOS compatible process for combining electrostatic actuated micromechanical resonators with optomechanical disk resonators in a silicon-on-insulator substrate has been presented. The displacement response of the mechanical resonators is obtained as an optical modulation at the output in these devices. Using this optical sensing technique, the mechanical resonance spectrum of disk resonators of radius 10μm in silicon was observed. Using scaled disk resonators and higher order ring resonators, mechanical modes up to 2GHz for disks and up to 3.5GHz for ring resonator have been shown. These measured resonance frequencies are the highest measured frequencies of electrostatically actuated micromechanical disk resonators to date.The output from this device is used to fabricate an opto-acoustic oscillator by using a combined optical electrical feedback loop. An oscillator working at 236.2MHz with an output RF power of 6.5dBm and a phase noise of -68dBc/Hz at a 1kHz frequency offset from the carrier has been demonstrated. An oscillator working at 1.12GHz with the scaled ring resonator structure has been shown to achieve an output RF power of 8.8dBm and a phase noise of -85dBc/Hz at 10kHz offset. Table 6.1 compares the performance of the 1.12GHz with other micro scale oscillators being developed. While the performance of the 1.12GHz has a phase noise performance lower than the other oscillators in the comparison, there is a large scope for improvement for the opto-acosutic oscillator.

As explained in the previous chapter, the phase noise of the opto-acoustic oscillator can be improved in two ways. The first way is to reduce the losses

Table 6.1: Performance comparison of micro-scale oscillators

Parameter	OAO	Silicon disk [58]	FBAR [59]	CMOS LC VCO [60]
Frequency	1.12GHz	60MHz	1.5GHz	4.7GHz
Quality Factor	2500	48000	1573	Q_{cap} = 62, Q_{ind} = 6
Phase Noise @10kHz offset(dBc/Hz) (scaled to 1.12GHz)	-85	-100	-115	-92.5
Phase Noise @1MHz offset(dBc/Hz) (scaled to 1.12GHz)	-120	-105	-150	-138

in the loop which would allow oscillation with a lower gain amplifier thereby reducing the noise added. Among the most significant losses in the loop are the losses at the electrical to mechanical air gap electrostatic transducer. The second area of loss in the loop is the insertion loss of the laser light from the laser into the waveguides through the grating couplers. The optical loss at the grating can be brought down to a dB per coupler from the current 6 to 8dB pwer coupler through design and process improvements. The second way to improve phase noise is to increase the overall energy stored in the system, which can be done by increasing the quality factor of the mechanical resonator and by adding additional optical delay in the loop. The mechanical quality factor of the system is around 2500 which is much smaller than the material limit for silicon at these frequencies as well as the quality factors of existing demonstration around these frequencies. An increased quality factor would bring the Leeson

frequency closer to the carrier and thereby reduce the phase noise close to the carrier.

6.0.1 Increasing transducer efficiency

The opto-acoustic oscillator uses electrostatically actuated mechanical resonators. The motional impedance, which determines the power transferred to the mechanical mode and thereby the displacement amplitude, is inversely proportional to the thickness of the actuation capacitor thickness. As these mechanical resonators are fabricated in photonics compatible 220nm thick device layer buried oxide SOI, the motional impedance of these resonators are much higher than those previously demonstrated which are use 2μm thick polysilicon layers [5, 4]. This is observed in the reflected power S11 being close to 0dB even at mechanical resonance indicating that there is very little power being transferred into the mechanical resonance. To improve the electrostatic transducer and reduce the motional impedance, the actuation gaps can be reduced by optimizing the lithography process. In addition, an array of disks can be used to reduce the motional impedance[61]. Another idea for improvement is to replace the air gap electrostatic transducer with other transducers which can be more efficient. An idea for a modified transducer is to use a piezoelectric transducer above the mechanical resonator to excite the different vibrational modes. Another idea for actuation is to use the technique of internal transduction using a pn diode within the mechanical resonator [62]. This scheme of actuation can potentially allow the mechanical actuation resonator to be combined with the optomechanical resonator. The single released using such a pn actuator would be similar to the pn disk modulator previously demonstrated [63].

6.0.2 Direct optical to mechanical conversion

The current implementation of the opto-acoustic oscillator works by converting the modulated optical signal back to the electrical domain using a photodetector and then feeding back to the modulator. An alternate idea for an opto-acoustic oscillator is to perform direct conversion from the optical modulated signal to mechanical vibrations using optical forces. The optical power inside an optical resonator exerts radiation pressure forces on the walls of the resonator proportional to the optical power [15]. This has been previously shown to excite self oscillations in ultra high optical quality factor resonators. While these forces exist in high quality factor silicon resonators, the forces are much smaller and are not enough to setup self oscillations. However, when the optical power at the input of the resonator is modulated at the mechanical resonant frequency, the optical force on the edges of the resonator is also modulated at the mechanical resonant frequency. This modulated force can directly excite the mechanical vibration mode of the disk which can be picked up through the electrostatic transducer. Alternately, the mechanical vibrations excited optically can be fed back into the optomechanical resonator of the modulator thereby eliminating the need to pass through the electrical domain in the opto-acoustic oscillator.

APPENDIX A

ESTIMATING ELECTROSTATIC FORCE ON MICROMECHANICAL RESONATORS

To obtain a model for the electrostatic force between the resonator and the actuation electrodes, one requires an understanding of how the actuation capacitor varies with gap distance electrode and the electric potential difference across the capacitor. The parallel plate approximation is not valid for the actuation capacitor as the gap between the electrode and the disk is comparable to the thickness of the disk. A finite element simulation in COMSOL was performed to determine the electric potential distribution and the capacitance. The capacitance for the resonator is evaluated to be 5.52fF. The measured series resistance of the routing beams is 3.2kΩ, obtained with shorted characterization devices. The electric potential difference across the actuation capacitor is calculated using a simple series RC model as shown in figure A.1. The electrostatic force for a unit potential is evaluated by integrating the Maxwell stress tensor by solving the field distribution using the finite element method in COMSOL as shown in fig **??**.The force per unit area for 1V potential is obtained to be 50.89μN/m which corresponds to a force of 2.398nN across the length of electrode around the disk. This force is equivalent to that obtained using the expression

$$\begin{aligned} F &= \left|\frac{\partial U}{\partial x}\right| = \frac{1}{2}\left|\frac{\partial C}{\partial x}\right| V^2 \\ F_{V=1} &= \frac{1}{2}\left|\frac{\partial C}{\partial x}\right| = 2.398nN \end{aligned} \tag{A.1}$$

The nonlinear dependence of the force on the applied electric potential is used to obtain an ac force at the frequency of applied ac voltage, by using a combination of DC and AC potentials.

$$F_\omega = \left|\frac{\partial C}{\partial x}\right| V_{dc} v_{ac} = 4.796 V_{dc} v_{ac} \tag{A.2}$$

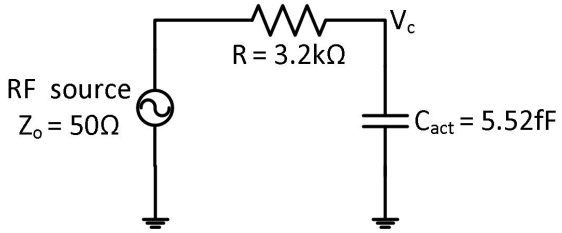

(a) Schematic of the circuit used for evaluating potential across actuation capacitor

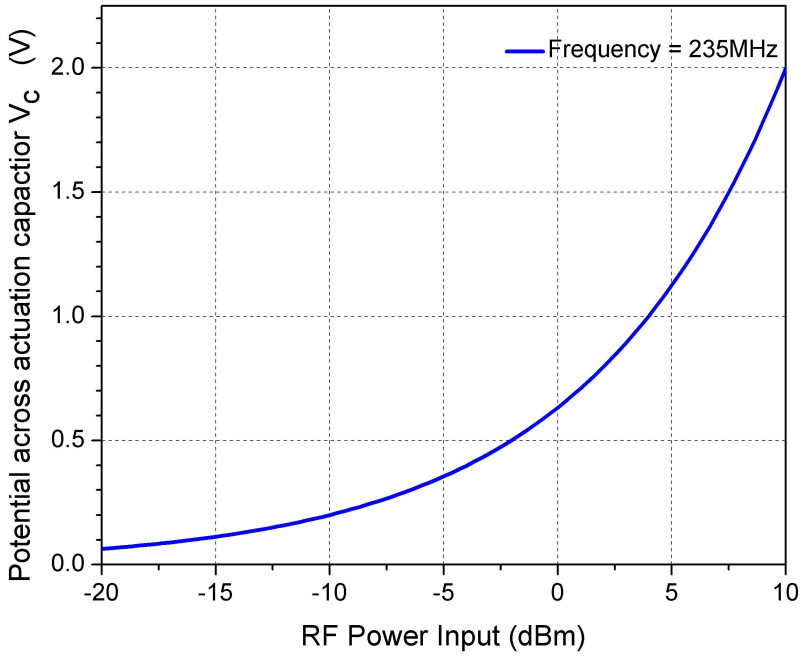

(b) Potential across capacitor (V_c) as a function of the RF power input at 235 MHz

Figure A.1: Model for evaluating potential across actuation capacitor

APPENDIX B

PROCESS FLOW FOR ACOUSTO OPTIC MODULATOR

The starting substrate for the fabrication of the Acousto Optic modulator is a silicon on insulator wafer with 250nm thick high resistivity (10-20 ohm cm) (100) silicon device layer on 3μm buried oxide.

1. Measure SOI stack

Equipment : Filmetrics

Measure stack height to establish device layer Si and buried oxide thickness

2. MOS clean

Equipment : MOS clean wet bench

Recipe: 10minutes dip in 1:1:6 NH_4OH:H_2O_2:H_2O at 70^{o}C

10minutes dip in 1:1:6 HCl:H_2O_2:H_2O at 70^{o}C

Rinse in De-Ionized (DI) H_2O

3. Thermal Oxidation : Hard Mask Creation

Equipment : Wet/Dry Oxide furnace - B2

Recipe: 24 minutes at 900^{o}C using Wet HCl Oxidation

4. Surface clean/preparation

Equipment : Acid Chemical Hood

Recipe: 2 minutes dip in Nanostrip

Rinse in DI H_2O

2 minutes dehydrate bake at 170^{o}C

5. Resist spin

Equipment : E-beam resist spinners

Recipe: Spin ma-N 2403 e-beam resist with parameters:

Time = 30s,speed=5000rpm,ramp= 2000rpm/s

Hard bake at 90^{o}C for 1 minute

6. Expose

Equipment : JEOL 9300 e-beam lithography system

Recipe: Expose at 5nA with dose of $1000\mu C/cm^2$ for waveguides, $800\mu C/cm^2$ for gratings, $600\mu C/cm^2$ for the resonators and $500\mu C/cm^2$ for the electrical routing and probe pads

7. Develop

Equipment : Electron beam resist hood

Recipe : 75s in 300MIF developer

8. Resist height measurement

Equipment: P10 profilometer

Recipe: Measure step height of the resist across alignment marks

9. Descum

Equipment: Oxford 81 etcher

Recipe:Oxygen plasma clean on empty chamber, time = 10minutes

Oxygen plasma clean recipe, time = 11s

10. Oxide Hard mask etch

Equipment: Oxford 100 etcher

Recipe: Oxygen plasma clean, time = 10minutes

CHF3 O2 Oxide Etch season on dummy wafer for 2 minutes

CHF3 O2 Oxide Etch , time = 52 seconds.

11. Metrology

Equipment : P10 profilometer and Filmetrics

Recipe: Measure step height on P-10 profilometer and Oxide hard mask - Silicon - buried oxide stack on filmetrics. Use measurements to determine if oxide hard mask is completely etched.

12. Resist Strip

Equipment : Oxford 81

Recipe: Oxygen plasma clean, time = 120s

11. Step height measurement

Equipment : P10 profilometer

Recipe: Measure step height on P-10 profilometer after resist removal to obtain depth of over etch into silicon .

13. Silicon device layer etch

Equipment : Plasmatherm PT 770

Recipe: Season on dummy silicon wafer using ssridar.prc for 10minutes

Etch sample using ssridar.prc for 50s

14. Metrology

Equipment : P10 profilometer and Filmetrics

Recipe: Measure step height on P-10 profilometer and Oxide hard mask - Silicon - buried oxide stack on filmetrics. Use measurements to verify complete etch of silicon device layer.

15. Oxide Hard mask removal

Equipment: Oxford 82 etcher

Recipe: Oxygen plasma clean, time = 10minutes

CHF3 O2 Oxide Etch season on dummy wafer for 3 minutes

CHF3 O2 Oxide Etch , time = 36 seconds.

16. Resist spin

Equipment : Photo resist spinners

Recipe: Spin SPR 220 photoresist with parameters:

Time = 30s,speed=3000rpm,ramp= 1000rpm/s

Hard bake at 115^{o}C for 90s

17. Expose - Ion Implant mask

Equipment : ABM contact aligner

Recipe: Exposure time of 13s

Post exposure bake at 115^{o}C for 90s

18. Develop

Equipment : General chemistry hoods

Recipe : 90s in 300MIF developer

19. Ion Implantation

Equipment : Eaton Ion Implanter

Recipe : Boron ion implantation at 30keV, Dose = 2e15. Keep current low to prevent photoresist burning.

20. Reist strip

Equipment : General Chemistry hood

Recipe:10 mins Acetone dip with ultrasonic agitation

10 mins Isopropyl alcohol dip

Rinse with DI H_2O

21. MOS clean

Equipment : MOS clean wet bench

Recipe: 10minutes dip in 1:1:6 NH_4OH:H_2O_2:H_2O at 70^{o}C

10minutes dip in 1:1:6 HCl:H_2O_2:H_2O at 70^{o}C

Rinse in De-Ionized (DI) H_2O

22. Furnace Anneal

Equipment : MOS clean anneal furnace - B1

Recipe: Load sample at 800^{o}C

10minutes 900^{o}C nitrogen anneal

Unload at 7% unload rate at 700^{o}C

23. Surface preparation

Equipment : Acid Hood

Recipe: 30s dip in Buffered Oxide Etchant 30:1

Rinse in DI H_2O

24. Vapor Prime Equipment : HMDS Vapor Prime oven

Recipe: Standard HMDS vapor prime recipe

25. Resist spin

Equipment : Photo resist spinners

Recipe: Spin SPR 220 photoresist with parameters:

Time = 30s,speed=3000rpm,ramp= 1000rpm/s

Hard bake at 115^{o}C for 90s

26. Expose - Release mask

Equipment : ABM contact aligner

Recipe: Exposure time of 13s

Post exposure bake at 115^{o}C for 90s

27. Develop

Equipment : General chemistry hoods

Recipe: 90s in 300MIF developer

28. Hard Bake

Equipment : Photoresist/E-beam resist hotplates

Recipe: 20 mins at 140^{o}C

29. Timed Release Etch

Equipment : Acid Hood

Recipe: 36min 30s in BOE 6:1

30. Resist strip and CPD prep

Equipment : Base/Solvent Hood

Recipe:10mins dip in Acetone for resist removal

5mins rinse in 1:1 Isopropyl alcohol: DI H_2O

5mins rinse in Isopropyl Alcohol

24. Critical Point Drying Equipment : Critical point dryer

Recipe: Transfer samples to critical point dryer without exposing to air and run standard recipe

BIBLIOGRAPHY

[1] S. Gigan, H. R. Boehm, M. Paternostro, F. Blaser, G. Langer, J. B. Hertzberg, K. C. Schwab, D. Baeuerle, M. Aspelmeyer, and A. Zeilinger, "Self-cooling of a micromirror by radiation pressure," *NATURE*, vol. 444, no. 7115, pp. 67–70, NOV 2 2006.

[2] O. Arcizet, P. F. Cohadon, T. Briant, M. Pinard, and A. Heidmann, "Radiation-pressure cooling and optomechanical instability of a micromirror," *NATURE*, vol. 444, no. 7115, pp. 71–74, NOV 2 2006.

[3] D. Kleckner and D. Bouwmeester, "Sub-kelvin optical cooling of a micromechanical resonator," *NATURE*, vol. 444, no. 7115, pp. 75–78, NOV 2 2006.

[4] J. Wang, Z. Ren, and C.-C. Nguyen, "1.156-ghz self-aligned vibrating micromechanical disk resonator," *Ultrasonics, Ferroelectrics and Frequency Control, IEEE Transactions on*, vol. 51, no. 12, pp. 1607 –1628, dec. 2004.

[5] J. Clark, W.-T. Hsu, M. Abdelmoneum, and C.-C. Nguyen, "High-q uhf micromechanical radial-contour mode disk resonators," *Microelectromechanical Systems, Journal of*, vol. 14, no. 6, pp. 1298 – 1310, dec. 2005.

[6] J. Geen, S. Sherman, J. Chang, and S. Lewis, "Single-chip surface micromachined integrated gyroscope with 50 deg;/h allan deviation," *Solid-State Circuits, IEEE Journal of*, vol. 37, no. 12, pp. 1860 – 1866, dec 2002.

[7] B. Ilic, H. G. Craighead, S. Krylov, W. Senaratne, C. Ober, and P. Neuzil, "Attogram detection using nanoelectromechanical oscillators," *Journal of Applied Physics*, vol. 95, no. 7, pp. 3694–3703, 2004. [Online]. Available: http://link.aip.org/link/?JAP/95/3694/1

[8] H. Nathanson, W. Newell, R. Wickstrom, and J. Davis, J.R., "The resonant gate transistor," *Electron Devices, IEEE Transactions on*, vol. 14, no. 3, pp. 117 – 133, mar 1967.

[9] K. Lakin, G. Kline, and K. McCarron, "High-q microwave acoustic resonators and filters," *Microwave Theory and Techniques, IEEE Transactions on*, vol. 41, no. 12, pp. 2139 –2146, dec 1993.

[10] A. Husain, J. Hone, H. W. C. Postma, X. M. H. Huang, T. Drake, M. Barbic, A. Scherer, and M. L. Roukes, "Nanowire-based very-high-frequency elec-

tromechanical resonator," *Applied Physics Letters*, vol. 83, no. 6, pp. 1240–1242, 2003. [Online]. Available: http://link.aip.org/link/?APL/83/1240/1

[11] H. Rokhsari, T. Kippenberg, T. Carmon, and K. Vahala, "Radiation-pressure-driven micro-mechanical oscillator," *Opt. Express*, vol. 13, no. 14, pp. 5293–5301, Jul 2005. [Online]. Available: http://www.opticsexpress.org/abstract.cfm?URI=oe-13-14-5293

[12] T. Carmon, H. Rokhsari, L. Yang, T. J. Kippenberg, and K. J. Vahala, "Temporal behavior of radiation-pressure-induced vibrations of an optical microcavity phonon mode," *Phys. Rev. Lett.*, vol. 94, p. 223902, Jun 2005. [Online]. Available: http://link.aps.org/doi/10.1103/PhysRevLett.94.223902

[13] M. Eichenfield, R. Camacho, J. Chan, K. J. Vahala, and O. Painter, "A picogram- and nanometre-scale photonic-crystal optomechanical cavity," *Nature*, vol. 459, no. 7246, pp. 550–555, May 2009. [Online]. Available: http://dx.doi.org/10.1038/nature08061

[14] G. Anetsberger, O. Arcizet, Q. P. Unterreithmeier, R. Riviere, A. Schliesser, E. M. Weig, J. P. Kotthaus, and T. J. Kippenberg, "Near-field cavity optomechanics with nanomechanical oscillators," *NATURE PHYSICS*, vol. 5, no. 12, pp. 909–914, DEC 2009.

[15] T. J. Kippenberg and K. J. Vahala, "Cavity optomechanics: Back-action at the mesoscale," *Science*, vol. 321, no. 5893, pp. 1172–1176, 2008. [Online]. Available: http://www.sciencemag.org/content/321/5893/1172.abstract

[16] W. Bogaerts, R. Baets, P. Dumon, V. Wiaux, S. Beckx, D. Taillaert, B. Luyssaert, J. Van Campenhout, P. Bienstman, and D. Van Thourhout, "Nanophotonic waveguides in silicon-on-insulator fabricated with cmos technology," *Lightwave Technology, Journal of*, vol. 23, no. 1, pp. 401 – 412, jan. 2005.

[17] J. Niehusmann, A. Vörckel, P. H. Bolivar, T. Wahlbrink, W. Henschel, and H. Kurz, "Ultrahigh-quality-factor silicon-on-insulator microringresonator," *Opt. Lett.*, vol. 29, no. 24, pp. 2861–2863, Dec 2004. [Online]. Available: http://ol.osa.org/abstract.cfm?URI=ol-29-24-2861

[18] Q. Xu, B. Schmidt, S. Pradhan, and M. Lipson, "Micrometre-scale silicon electro-optic modulator," *NATURE*, vol. 435, no. 7040, pp. 325–327, MAY 19 2005.

[19] M. Lipson, "Guiding, modulating, and emitting light on silicon-challenges and opportunities," *J. Lightwave Technol.*, vol. 23, no. 12, p. 4222, Dec 2005. [Online]. Available: http://jlt.osa.org/abstract.cfm?URI=jlt-23-12-4222

[20] M. Li, W. H. P. Pernice, C. Xiong, T. Baehr-Jones, M. Hochberg, and H. X. Tang, "Harnessing optical forces in integrated photonic circuits," *NATURE*, vol. 456, no. 7221, pp. 480–U28, NOV 27 2008.

[21] V. Kaajakari, T. Mattila, A. Oja, J. Kiihamaki, and H. Seppa, "Square-extensional mode single-crystal silicon micromechanical resonator for low-phase-noise oscillator applications," *Electron Device Letters, IEEE*, vol. 25, no. 4, pp. 173 – 175, april 2004.

[22] S. Pourkamali, A. Hashimura, R. Abdolvand, G. Ho, A. Erbil, and F. Ayazi, "High-q single crystal silicon harpss capacitive beam resonators with self-aligned sub-100-nm transduction gaps," *Microelectromechanical Systems, Journal of*, vol. 12, no. 4, pp. 487 – 496, aug. 2003.

[23] Z. Hao, S. Pourkamali, and F. Ayazi, "Vhf single-crystal silicon elliptic bulk-mode capacitive disk resonators-part i: design and modeling," *Microelectromechanical Systems, Journal of*, vol. 13, no. 6, pp. 1043 – 1053, dec. 2004.

[24] M. Onoe, "Contour vibrations of isotropic circular plates," *Journal of the Acoustical Society of America*, vol. 28, no. 6, pp. 1158–1162, 1956. [Online]. Available: http://dx.doi.org/doi/10.1121/1.1908579

[25] H. A. C. Tilmans, "Equivalent circuit representation of electromechanical transducers: I. lumped-parameter systems," *Journal of Micromechanics and Microengineering*, vol. 6, no. 1, p. 157, 1996. [Online]. Available: http://stacks.iop.org/0960-1317/6/i=1/a=036

[26] V. Kajaakari, "Electrical equivalent circuits for microresonators," http://www.kaajakari.net/ ville/research/tutorials/eq_circ_tutorial.pdf.

[27] M. Lipson, "Guiding, modulating, and emitting light on silicon-challenges and opportunities," *Lightwave Technology, Journal of*, vol. 23, no. 12, pp. 4222 – 4238, dec. 2005.

[28] D. Miller, "Rationale and challenges for optical interconnects to electronic chips," *Proceedings of the IEEE*, vol. 88, no. 6, pp. 728 –749, jun 2000.

[29] M. Soltani, "Novel integrated silicon nanophotonic structures using ultra-high q resonators," Ph.D. dissertation, Georgia Institute of Technology, 2009.

[30] B. E. Little, S. T. Chu, H. A. Haus, J. Foresi, and J.-P. Laine, "Microring resonator channel dropping filters," *Journal of Lightwave Technology*, vol. 15, pp. 998–1005, Jun. 1997.

[31] M. Gnan, S. Thorns, D. Macintyre, R. De La Rue, and M. Sorel, "Fabrication of low-loss photonic wires in silicon-on-insulator using hydrogen silsesquioxane electron-beam resist," *Electronics Letters*, vol. 44, no. 2, pp. 115 –116, 17 2008.

[32] Y. Vlasov and S. McNab, "Losses in single-mode silicon-on-insulator strip waveguides and bends," *Opt. Express*, vol. 12, no. 8, pp. 1622–1631, Apr 2004. [Online]. Available: http://www.opticsexpress.org/abstract.cfm?URI=oe-12-8-1622

[33] K. K. Lee, D. R. Lim, L. C. Kimerling, J. Shin, and F. Cerrina, "Fabrication of ultralow-loss si/sio2 waveguides by roughness reduction," *Opt. Lett.*, vol. 26, no. 23, pp. 1888–1890, Dec 2001. [Online]. Available: http://ol.osa.org/abstract.cfm?URI=ol-26-23-1888

[34] T. Baehr-Jones, M. Hochberg, C. Walker, and A. Scherer, "High-q optical resonators in silicon-on-insulator-based slot waveguides," *Applied Physics Letters*, vol. 86, no. 8, p. 081101, 2005. [Online]. Available: http://dx.doi.org/doi/10.1063/1.1871360

[35] P. Dumon, W. Bogaerts, V. Wiaux, J. Wouters, S. Beckx, J. V. Campenhout, D. Taillaert, B. Luyssaert, P. Bienstman, D. V. Thourhout, and R. Baets, "Low-loss soi photonic wires and ring resonators fabricated with deep uv lithography," *Photonics Technology Letters, IEEE*, vol. 16, no. 5, pp. 1328 – 1330, may 2004.

[36] R. Koh, "Buried layer engineering to reduce the drain-induced barrier lowering of sub-0.05μm soi-mosfet," *Japanese Journal of Applied Physics*, vol. 38, no. Part 1, No. 4B, pp. 2294–2299, 1999. [Online]. Available: http://jjap.jsap.jp/link?JJAP/38/2294/

[37] L. Su, J. Chung, D. Antoniadis, K. Goodson, and M. Flik, "Measurement and modeling of self-heating in soi nmosfet's," *Electron Devices, IEEE Transactions on*, vol. 41, no. 1, pp. 69 –75, jan 1994.

[38] J.-T. Park and J.-P. Colinge, "Multiple-gate soi mosfets: device design guidelines," *Electron Devices, IEEE Transactions on*, vol. 49, no. 12, pp. 2222 – 2229, dec 2002.

[39] D. Hisamoto, W.-C. Lee, J. Kedzierski, H. Takeuchi, K. Asano, C. Kuo, E. Anderson, T.-J. King, J. Bokor, and C. Hu, "Finfet-a self-aligned double-gate mosfet scalable to 20 nm," *Electron Devices, IEEE Transactions on*, vol. 47, no. 12, pp. 2320 – 2325, dec 2000.

[40] P. Chu, J. Chen, R. Yeh, G. Lin, J. Huang, B. Warneke, and S. Pister, "Controlled pulse-etching with xenon difluoride," in *Solid State Sensors and Actuators, 1997. TRANSDUCERS '97 Chicago., 1997 International Conference on*, vol. 1, jun 1997, pp. 665 –668 vol.1.

[41] C. Batten, A. Joshi, J. Orcutt, A. Khilo, B. Moss, C. Holzwarth, M. Popovic, H. Li, H. Smith, J. Hoyt, F. Kartner, R. Ram, V. Stojanovic, and K. Asanovic, "Building many-core processor-to-dram networks with monolithic cmos silicon photonics," *Micro, IEEE*, vol. 29, no. 4, pp. 8 –21, july-aug. 2009.

[42] V. R. Almeida, R. R. Panepucci, and M. Lipson, "Nanotaper for compact mode conversion," *Opt. Lett.*, vol. 28, no. 15, pp. 1302–1304, Aug 2003. [Online]. Available: http://ol.osa.org/abstract.cfm?URI=ol-28-15-1302

[43] K. Preston, B. Schmidt, and M. Lipson, "Polysilicon photonic resonators for large-scale 3d integration of optical networks," *Opt. Express*, vol. 15, no. 25, pp. 17 283–17 290, Dec 2007. [Online]. Available: http://www.opticsexpress.org/abstract.cfm?URI=oe-15-25-17283

[44] Z. Zhang, M. Dainese, L. Wosinski, and M. Qiu, "Resonance-splitting and enhanced notch depth in soi ring resonators with mutual mode coupling," *Opt. Express*, vol. 16, no. 7, pp. 4621–4630, Mar 2008. [Online]. Available: http://www.opticsexpress.org/abstract.cfm?URI=oe-16-7-4621

[45] Q. Li, Z. Zhang, F. Liu, M. Qiu, and Y. Su, "Dense wavelength conversion and multicasting in a resonance-split silicon microring," *Applied Physics Letters*, vol. 93, no. 8, p. 081113, 2008. [Online]. Available: http://dx.doi.org/doi/10.1063/1.2976123

[46] L. Martinez and M. Lipson, "High confinement suspended micro-ring resonators in silicon-on-insulator," *Opt. Express*, vol. 14, no. 13, pp. 6259–6263, Jun 2006. [Online]. Available: http://www.opticsexpress.org/abstract.cfm?URI=oe-14-13-6259

[47] M. Oxborrow, "Traceable 2-d finite-element simulation of the whispering-gallery modes of axisymmetric electromagnetic resonators," *Microwave Theory and Techniques, IEEE Transactions on*, vol. 55, no. 6, pp. 1209 –1218, june 2007.

[48] R. Tabrizian, M. Rais-Zadeh, and F. Ayazi, "Effect of phonon interactions on limiting the f.q product of micromechanical resonators," in *Solid-State Sensors, Actuators and Microsystems Conference, 2009. TRANSDUCERS 2009. International*, june 2009, pp. 2131 –2134.

[49] E. Hwang and S. Bhave, "Pn-diode transduced 3.7-ghz silicon resonator," in *Micro Electro Mechanical Systems (MEMS), 2010 IEEE 23rd International Conference on*, jan. 2010, pp. 208 –211.

[50] P. Steeneken, J. Ruigrok, S. Kang, J. van Beek, J. Bontemps, and J. Koning, "Parameter extraction and support-loss in mems resonators," in *Proceeding of Comsol conference 2007, Grenoble*, 2007, p. 725.

[51] S. Wang, S. Chandorkar, A. Graham, M. Messana, J. Salvia, and T. Kenny, "Encapsulated mechanically coupled fully-differential breathe-mode ring filters with ultra-narrow bandwidth," in *Solid-State Sensors, Actuators and Microsystems Conference (TRANSDUCERS), 2011 16th International*, june 2011, pp. 942 –945.

[52] E. Dieulesaint and D. Royer, "Optoacoustic oscillator using a quartz resonator," in *1982 Ultrasonics Symposium*, 1982, pp. 793 – 795.

[53] K. Hung, P. Ko, C. Hu, and Y. Cheng, "A unified model for the flicker noise in metal-oxide-semiconductor field-effect transistors," *Electron Devices, IEEE Transactions on*, vol. 37, no. 3, pp. 654 –665, mar 1990.

[54] E. Rubiola, *Phase Noise and Frequency Stability in Oscillators*, 1st ed. CNRS FEMTO-ST Institute: CAmbridge University Press, 2009, vol. 1.

[55] X. S. Yao and L. Maleki, "Optoelectronic microwave oscillator," *J. Opt. Soc. Am. B*, vol. 13, no. 8, pp. 1725–1735, Aug 1996. [Online]. Available: http://josab.osa.org/abstract.cfm?URI=josab-13-8-1725

[56] X. Yao and L. Maleki, "Optoelectronic oscillator for photonic systems," *Quantum Electronics, IEEE Journal of*, vol. 32, no. 7, pp. 1141 –1149, jul 1996.

[57] L. Maleki, V. Iltchenko, S. Huang, and A. Savchenkov, "Micro-optical res-

onators and applications in optoelectronic oscillator," in *Microwave Photonics, 2001. MWP '01. 2001 International Topical Meeting on*, jan. 2002, pp. 37 – 40.

[58] Y.-W. Lin, S. Lee, S.-S. Li, Y. Xie, Z. Ren, and C.-C. Nguyen, "Series-resonant vhf micromechanical resonator reference oscillators," *Solid-State Circuits, IEEE Journal of*, vol. 39, no. 12, pp. 2477 – 2491, dec. 2004.

[59] S. Rai, Y. Su, W. Pang, R. Ruby, and B. Otis, "A digitally compensated 1.5 ghz cmos/fbar frequency reference," *Ultrasonics, Ferroelectrics and Frequency Control, IEEE Transactions on*, vol. 57, no. 3, pp. 552 –561, march 2010.

[60] Z. Li and K. O, "A low-phase-noise and low-power multiband cmos voltage-controlled oscillator," *Solid-State Circuits, IEEE Journal of*, vol. 40, no. 6, pp. 1296 – 1302, june 2005.

[61] M. Demirci and C.-C. Nguyen, "Mechanically corner-coupled square microresonator array for reduced series motional resistance," *Microelectromechanical Systems, Journal of*, vol. 15, no. 6, pp. 1419 –1436, dec. 2006.

[62] E. Hwang and S. Bhave, "Pn-diode transduced 3.7-ghz silicon resonator," in *Micro Electro Mechanical Systems (MEMS), 2010 IEEE 23rd International Conference on*, jan. 2010, pp. 208 –211.

[63] M. R. Watts, W. A. Zortman, D. C. Trotter, R. W. Young, and A. L. Lentine, "Vertical junction silicon microdisk modulators and switches," *Opt. Express*, vol. 19, no. 22, pp. 21 989–22 003, Oct 2011. [Online]. Available: http://www.opticsexpress.org/abstract.cfm?URI=oe-19-22-21989